

**A Thesis Submitted for the Degree of PhD at the University of Warwick**

**Permanent WRAP URL:**

<http://wrap.warwick.ac.uk/81947>

**Copyright and reuse:**

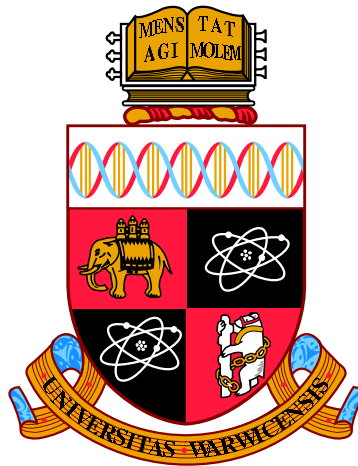
This thesis is made available online and is protected by original copyright.

Please scroll down to view the document itself.

Please refer to the repository record for this item for information to help you to cite it.

Our policy information is available from the repository home page.

For more information, please contact the WRAP Team at: [wrap@warwick.ac.uk](mailto:wrap@warwick.ac.uk)



# Computer Simulations of Liquid Crystals

by

**Anja Humpert**

**Thesis**

Submitted to the University of Warwick

for the degree of

**Doctor of Philosophy**

**Department of Physics**

August 2016



# Contents

<b>List of Tables</b>	<b>iv</b>
<b>List of Figures</b>	<b>v</b>
<b>Acknowledgments</b>	<b>viii</b>
<b>Declarations</b>	<b>ix</b>
<b>Abstract</b>	<b>x</b>
<b>Chapter 1 Introduction to liquid crystals</b>	<b>1</b>
1.1 Liquid crystal molecules and different liquid crystalline phases . . . .	2
1.2 Order parameters . . . . .	3
1.3 Phenomenological free energy . . . . .	4
1.4 Elastic properties of nematic liquid crystals . . . . .	6
1.5 Dynamical properties of nematic liquid crystals . . . . .	8
1.6 Topological defects . . . . .	10
1.7 Scope of this thesis . . . . .	17
<b>Chapter 2 Computer simulations</b>	<b>19</b>
2.1 Computer Simulations of Liquid Crystals . . . . .	20
2.2 Molecular Dynamics (MD) . . . . .	21
2.2.1 Integration of the equations of motion for linear molecules . .	22
2.2.2 Linking simulations and experiments . . . . .	23
2.2.3 Improving efficiency . . . . .	24
2.2.4 Reduced units . . . . .	28
2.3 Equilibration of the Gay-Berne nematic LC phase . . . . .	28
2.4 Visualisation . . . . .	32
2.5 Conclusions . . . . .	36

<b>Chapter 3</b>	<b>Elastic constants in nematic liquid crystals</b>	<b>37</b>
3.1	Introduction . . . . .	37
3.2	Theoretical background . . . . .	39
3.3	Model and simulation details . . . . .	40
3.4	Data analysis and results . . . . .	42
3.5	Conclusions . . . . .	47
<b>Chapter 4</b>	<b>Dynamics in nematic liquid crystals</b>	<b>49</b>
4.1	Introduction . . . . .	49
4.2	Theoretical background . . . . .	50
4.3	Simulation details . . . . .	54
4.4	Data analysis and results . . . . .	55
4.5	Discussion . . . . .	59
4.6	Conclusions . . . . .	60
<b>Chapter 5</b>	<b>Topological defects around a nanoparticle inserted into a nematic</b>	<b>62</b>
5.1	Introduction . . . . .	62
5.2	Model and simulation details . . . . .	65
5.3	Data analysis and results . . . . .	69
5.3.1	Saturn ring defect . . . . .	69
5.3.2	Boojum defect . . . . .	72
5.3.3	Satellite defect . . . . .	72
5.3.4	Nanoparticle pair interactions . . . . .	77
5.4	Conclusions . . . . .	78
<b>Chapter 6</b>	<b>Entangled defect structures around nanoparticles in nematics</b>	<b>80</b>
6.1	Introduction . . . . .	80
6.2	Model and simulation details . . . . .	83
6.3	Data analysis and results . . . . .	85
6.4	Conclusions . . . . .	93
<b>Chapter 7</b>	<b>Dynamics of a single disclination line</b>	<b>94</b>
7.1	Introduction . . . . .	94
7.2	Theoretical background . . . . .	95
7.3	Model and simulation details . . . . .	97
7.4	Data analysis and results . . . . .	99

7.5	Conclusions . . . . .	105
<b>Chapter 8 Interaction of nanoparticles with a single disclination line</b>		<b>106</b>
8.1	Introduction . . . . .	106
8.2	Model and simulation details . . . . .	108
8.3	Data analysis and results . . . . .	110
8.4	Conclusions . . . . .	122
<b>Chapter 9 Conclusions</b>		<b>124</b>

# List of Tables

3.1	Elastic constants for eight different state points . . . . .	41
3.2	Elastic constants for simulation with 8000 Gay-Berne molecules . . .	46
4.1	Basic relations for velocity coefficients . . . . .	52
4.2	Proportionality factors relating the relaxation rates of the director and velocity correlations to $k^2$ . . . . .	58
4.3	Proportionality factors relating the relaxation rates of the director correlations to $k^2$ . . . . .	59
5.1	Simulation parameters of simulations of nanoparticle inclusions in a nematic host . . . . .	65
6.1	Frequency of observations of different entangled defect structures for a different particle radii and separations . . . . .	92

# List of Figures

1.1	Area of all flat-panel displays produced worldwide . . . . .	2
1.2	Mesogenic compounds . . . . .	3
1.3	Schematic sketches of the three basic deformation modes in a liquid crystal: Splay, twist and bend. . . . .	5
1.4	Schematic of the three basic deformation modes in a nematic liquid crystal . . . . .	7
1.5	Schlieren texture in a liquid crystal . . . . .	10
1.6	Sketch of nematic fields near disclination lines . . . . .	11
1.7	Sketch of director field around a particle inclusion . . . . .	13
1.8	Mircographs of silica microspheres with homeotropic anchoring embedded in a nematic host . . . . .	15
2.1	Lennard-Jones potential . . . . .	25
2.2	Periodic boundary conditions and minimum image convention . . . .	26
2.3	Neighbour lists and cell lists . . . . .	27
2.4	Standard Gay-Berne potential . . . . .	30
2.5	Purely repulsive Gay-Berne potential . . . . .	31
2.6	QMGA snapshots of slices through the Gay-Berne system . . . . .	33
2.7	Cubic b-spline weighting function . . . . .	35
3.1	Surface fitting results for $W_{13}$ and $W_{23}$ . . . . .	43
3.2	Slices through $W_{13}$ and $W_{23}$ . . . . .	44
3.3	Gay-Berne potential for the end-to-end configuration . . . . .	47
4.1	Time correlation functions of the director fluctuations . . . . .	56
4.2	Time correlation functions of the velocity fluctuations . . . . .	57
4.3	Relaxation rates $\nu$ as a function of $k^2$ . . . . .	57
4.4	Relaxation rates $\nu_{\text{bend}}$ for bend fluctuations . . . . .	58

5.1	Sketch of director field around a particle inclusion . . . . .	63
5.2	Schematic to illustrate notation $x$ , $y$ and $\theta$ used in the derivation of the closest approach distance $\sigma_c$ for planar surface anchoring. . . . .	67
5.3	Cross-section of the simulation box showing local order parameter maps and defect regions . . . . .	70
5.4	Distance of the defect region from the surface of the nanoparticle . .	71
5.5	Local order parameter maps and defect regions of boojum defect . .	72
5.6	Defect regions for different time steps with fixed nanoparticle at the centre . . . . .	73
5.7	Average defect line position for Saturn ring to satellite transition . .	74
5.8	Transition from the satellite to the Saturn ring defect . . . . .	75
5.9	First and last time step for two nanoparticles inserted in a nematic .	77
5.10	Separation and the angle with respect to the far field director . . . .	78
6.1	Micrographs of particles in a nematic entangled by disclination lines	81
6.2	QMGA snapshot of the setup from two different angles . . . . .	85
6.3	Defect structures observed for two nanoparticles . . . . .	86
6.4	Disclination lines around two nanoparticles . . . . .	88
6.5	Schematic of two nanoparticles and the surrounding disclination lines	88
6.6	Defect structure versus time for $R_{NP} = 10$ and a surface-to-surface separation $\Delta = 2.94\sigma_0$ . . . . .	89
6.7	Defect structure versus time for $R_{NP} = 10$ and a surface-to-surface separation $\Delta = 10.3\sigma_0$ . . . . .	89
6.8	Defect structure versus time for $R_{NP} = 15$ and a surface-to-surface separation $\Delta = 5\sigma_0$ . . . . .	90
6.9	Defect structure versus time for $R_{NP} = 15$ and a surface-to-surface separation $\Delta = 10\sigma_0$ . . . . .	90
6.10	Defect structure versus time for $R_{NP} = 20\sigma_0$ and a surface-to-surface separation $\Delta = 10\sigma_0$ . . . . .	91
6.11	Disclination line (red) corresponding to $S < 0.4$ time-averaged over entire production run for $R_{NP} = 10\sigma_0$ and $\Delta = 2.94\sigma_0$ . . . . .	93
7.1	Sketch of the virtual cylinder wall in a simulation box . . . . .	98
7.2	Strength function $f$ . . . . .	99
7.3	Two dimensional cross-section of the simulation box in the $x$ - $y$ plane	100
7.4	3D visualisation of disclination lines for the system snapshots . . . .	101
7.5	Number of Westin grid points with $c_l < 0.12$ versus time . . . . .	102
7.6	Two-dimensional cross-section of the disclination line . . . . .	102



7.7	Visualisation of the defect line at intervals of $1 \times 10^6$ . . . . .	103
7.8	Inverse of decay times $\tau$ and inverse of square amplitudes of the fluctuations versus $k^2$ . . . . .	104
8.1	Sketch of the director field corresponding to a -1/2 defect . . . . .	109
8.2	Maps of the local order, biaxiality, director field and density . . . . .	110
8.3	3D visualisation of defect lines for setup0 . . . . .	111
8.4	Defect visualisation for setupC . . . . .	112
8.5	Isosurface with $S < 0.5$ for time-averaged results for setupC . . . . .	113
8.6	2D time-averaged local order parameter and director field maps for setup30 $\rightarrow$ setup180 . . . . .	114
8.7	3D visualisation of a typical defect structure observed for setup30 $\rightarrow$ setup180 . . . . .	115
8.8	Six examples of entangled and intermediate defect structures . . . . .	116
8.9	Trajectories of nanoparticles for all setups . . . . .	117
8.10	Time-averaged forces acting on the nanoparticles . . . . .	118
8.11	The $x$ , $y$ and $z$ components of the vector connecting the positions of the two nanoparticles over time . . . . .	119
8.12	Two nanoparticles initially placed at centre of disclination line separated along $z$ by $30\sigma_0$ . . . . .	119
8.13	The $x$ , $y$ and $z$ components of the vector connecting the positions . . . . .	120
8.14	Two nanoparticles initially placed at centre of the simulation box separated along $x$ by $30\sigma_0$ . . . . .	121
8.15	The $x$ , $y$ and $z$ components of the vector connecting the positions of the two nanoparticles . . . . .	121

# Acknowledgments

I would like to thank my supervisor, Prof. Mike Allen, for his patience, support and encouragement and Gareth Alexander for continuing my supervision for the last two years.

I am grateful for the computer facilities provided by Warwick University Centre for Scientific Computing and the support from the Engineering and Physical Sciences Research Council. The C.R. Barber Trust travel bursary from the Institute of Physics and the generous invite by the Soft Matter Group, University of Ljubljana are gratefully acknowledged.

I thank the theory group, especially former and current PS131 and PS001 office friends for all the conversations, walks, coffee-breaks, pub debates, tennis matches and their general support and friendship.

I would like to thank Duncan and Woody for looking after my many packages and the great chats we have had on my daily to weekly excursions to Physics stores.

I thank the members of the Warwick University Canoe Polo club for great distractions from work in the evenings and weekends and for making my time at Warwick fantastic.

Finally, and most importantly, I would like to thank my family and Matt for their support and encouragement.

# Declarations

I declare that no part of this thesis has been submitted to a higher degree in this, or any other, university. The research reported herein has been published [1, 2] and is the result of my own research except where reference is made to the work of others. All research was carried out under the supervision of Professor M.P. Allen and Gareth Alexander at the University of Warwick, between October 2012 and April 2016. The work presented (including data generated and data analysis) was carried out by the author except in the cases outlined here: Figure 1.1 was reproduced from [3]. Figure 1.5 was reproduced from [4]. Figure 1.8 and 6.1 were reproduced from [5].

Anja Humpert

June 2016

# Abstract

In this thesis we studied nematic liquid crystals using molecular dynamics simulations based on the coarse grained Gay-Berne potential. The elastic and dynamical properties of the nematic bulk were calculated and the impact of the system size and simulation run time were investigated showing that both have to be considered carefully. For the bend fluctuations we observed propagating modes for the director and velocity components. This contradicts statements found in the literature that assume these modes are overdamped. We derive from nematodynamics that this assumption may not be valid for all systems and hence we argue that propagating modes may be observed in experiments.

Furthermore we studied defect structures forming due to nanoparticle inclusions in nematics. Depending on the particle size and the surface anchoring three different defect types were observed: Saturn ring, surface-ring and boojum defects. The satellite defect was found to be unstable for the particle sizes studied here, which is in agreement with theoretical predictions. For two nanoparticles in close proximity entangled defects formed, similar to experimental observations for micron sized particles. We explain the three-ring structure, which was observed in other molecular simulations, as a superposition of the different entangled states.

Finally we calculated the line tension and viscous drag of a single disclination line of strength  $-1/2$ . Nanoparticles placed in close proximity of the single disclination experienced highly non-linear attractive forces. Once the particle ‘touches’ the disclination it remained connected for the entire simulation. In addition we have shown that the presence of a single disclination has a significant impact on inter-nanoparticle interactions.

# Chapter 1

## Introduction to liquid crystals

The liquid crystal (LC), or mesomorphic, state is a phase that can occur between the liquid and the crystalline phases [6]. On the one hand liquid crystals have some liquid-like properties, for example fluidity and the inability to support shear; on the other hand they show a crystal-like anisotropy in optical, electrical and magnetic properties. Liquid crystals exhibit birefringence and easy switching in response to an applied field, which has driven their main application in the display technology.

We distinguish between thermotropic and lyotropic liquid crystals. For thermotropic LCs the phase transitions are temperature driven. Here the molecules are usually elongated or disk-shaped, which, due to their shape, tend to align with each other. They are also referred to as calamitic and discotic mesogens respectively. The phase transitions in lyotropic liquid crystals are driven by concentration, rather than temperature. Lyotropic LCs can be formed by amphiphilic molecules, which self-assemble due to the hydrophobic effect. Another group of lyotropic LCs are colloidal suspensions. In lyotropic LCs the orientational order is mostly caused by the geometry of the LC molecules.

Due to their unique properties liquid crystals are of major technological importance. Their main application is in liquid crystal displays [7, 8]. Since LCs are very sensitive to external fields, the orientation of the molecules can be controlled by applying an electric field across the LC. Most commercial LC displays are based on twisted-nematic LCs. An external light source is polarised before it enters the twisted-nematic film, which guides the light through the film. Here the optical axis is along the averaged orientation of the molecules. The axis of polarisation rotates, following the twist of the LC. If the orientation of the molecules of the final layer matches the angle of the second polariser, the light passes through. The LC can be untwisted gradually by applying an external field. By controlling the strength

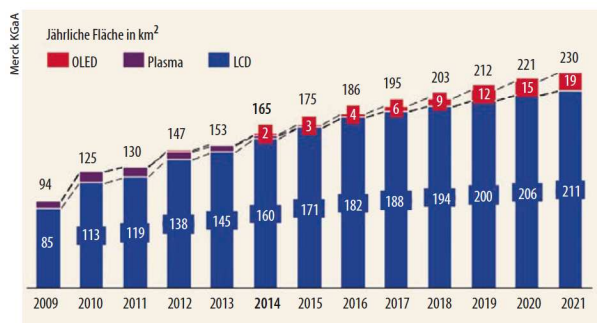


Figure 1.1: The area of all flat-panel displays produced worldwide. Reproduced with permission from [3]. Original from Merck KGaA.

of the external field, light can be allowed to pass through in varying amounts. LC displays have the advantage of being inexpensive and being able to operate under low voltage. They are commonly used in devices such as television and phones. The liquid crystal display market is constantly growing. In Fig. 1.1 the area of annually produced displays worldwide is shown. One can see that the area is increasing by roughly 5% each year. In 2013 only, more than one billion smart phones with LC displays were produced [3]. The main advantages of liquid crystal displays compared to other displays are fast response times, high contrast and resolution and energy efficiency.

## 1.1 Liquid crystal molecules and different liquid crystalline phases

Throughout the years many different molecules were found that can form a liquid crystalline phase. Especially interesting are the ones that can be mesomorphic at room temperature, which makes them particularly interesting for everyday applications. A few typical examples of mesogenic compounds are shown in Fig. 1.2. Note that the mesomorphic behaviour is mainly determined by the molecular shape.

LC molecules can show a variety of different LC phases. The most common one for rod-like molecules is the nematic phase, which is defined by long-range orientational order, but the absence of long-range positional order. A LC with positional order, but in one or two directions only is called smectic phase. The smectic A phase can be thought of as piled layers of nematics with molecules perpendicular to the smectic plane. The smectic B phase is very similar to the A phase; the molecules however are arranged into a network of hexagons within the smectic layer. In the smectic C phase the molecules are arranged as in a smectic A phase, but the

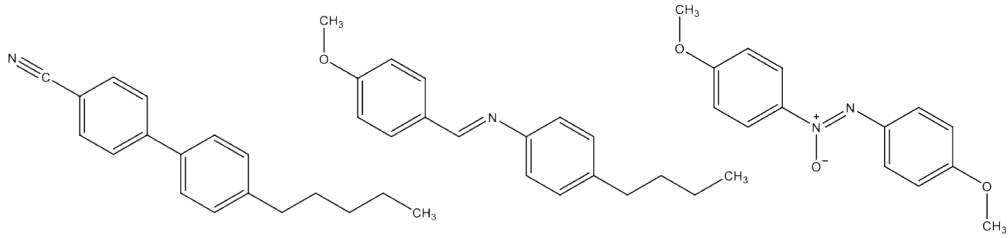


Figure 1.2: Mesogenic compounds from left to right: (i) 5CB (4-cyano-4'-pentylbiphenyl), nematic at room temperature ( $22.5 - 35^\circ\text{C}$ ), (ii) MBBA (N-p-methoxybenzylidene-p-butylaniline), (iii) PAA (p-azoxyanisole) [6, 9].

molecules are tilted within the smectic plane. Disk-shaped LC molecules can exhibit the columnar phase, where molecules are stacked on top of each other in column-like structures, hence demonstrating two-dimensional positional order. A nematic phase formed by disk-like particles is referred to as discotic phase. Another phase is the cholesteric LC phase. Here the average orientation of the molecules varies throughout the medium following a helical structure. The distance over which the orientation rotates through a full cycle is called the pitch length, which is similar to the optical wave length of several hundred nanometers. The pitch length is very sensitive to temperature and external fields. Hereafter we will be dealing solely with the nematic phase.

## 1.2 Order parameters

For all LC phases we can identify an average direction of the particles' major axes called the director  $\hat{n}$ , which is in general time and position dependent. The director is not a vector, because no net polarisation has been observed in liquid crystals, i.e. the number of molecules pointing into opposite directions is the same. In other words,  $\hat{n}$  and  $-\hat{n}$  are indistinguishable. In general, the direction of the director is arbitrary, but in practice it is enforced by the environment, such as the walls of the container.

To describe the ordering within a liquid crystal, an order parameter  $S$  is introduced, which quantifies the orientation fluctuation of the molecules around the director. The choice is non-trivial since it has to vanish in isotropic liquids due to symmetry. Taking into account the  $-\hat{n} \leftrightarrow \hat{n}$  equivalence, the order parameter can be calculated via [6]

$$S = \frac{1}{2} \langle (3 \cos^2 \theta - 1) \rangle, \quad (1.1)$$

where  $\theta$  is the angle between the orientation vector of a molecule and the director

$\hat{\mathbf{n}}$ . The angle brackets denote a statistical average. The order parameter  $S$  varies between  $-\frac{1}{2}$  and 1. If all molecules are perfectly aligned with the director, the angle between each molecule and the director is zero, hence  $\langle \cos^2 \theta \rangle = 1$  and therefore  $S=1$ . The order parameter is zero if the orientation of the molecules is entirely random, i.e. isotropic, since  $\langle \cos^2 \theta \rangle = \frac{1}{3}$ . Note that in simulations with  $N$  particles finite-size effects will lead to a small positive value of order  $\mathcal{O}(N^{-1/2})$  [10]. For the nematic phase  $S$  takes an intermediate value with  $0.5 \leq S \leq 0.85$  [7, 11]. For  $S=-\frac{1}{2}$  all molecules lie within the surface normal to the director. The order parameter can also be calculated from the more general order tensor  $\mathbf{Q}$  which is given by

$$Q_{mm'} = \frac{1}{N} \sum_{i=1}^N \frac{3}{2} \hat{u}_{im} \hat{u}_{im'} - \frac{1}{2} \delta_{mm'} \quad (1.2)$$

for uniaxial molecules. Here  $\hat{\mathbf{u}}_i$  is the orientation vector of the molecule  $i$  and  $m, m' = x, y, z$ .  $\delta_{mm'}$  is the Kronecker delta and  $N$  the total number of molecules within the volume for which  $Q_{mm'}$  is calculated.  $Q_{mm'}$  is a symmetric and traceless tensor. A full description of the nematic phase requires an order tensor to account for all five degrees of freedom: orientation of the director, orientation of the possible biaxial ordering and the nematic order  $S$  and biaxiality  $P$ . Here we solely focus on uniaxial nematics, for which  $P = 0$ . As for  $S$ , finite size effects will lead to a value of biaxiality  $P$  that is not identically zero. Both the order parameter and the director can be calculated directly from the order tensor. The order parameter  $S$  is equal to the highest eigenvalue of the order tensor and its corresponding normalised eigenvector represents the director  $\hat{\mathbf{n}}$ . In diagonal form  $\mathbf{Q}$  is given by

$$\mathbf{Q}^{\text{diag}} = \begin{pmatrix} \frac{2}{3}S & 0 & 0 \\ 0 & -\frac{1}{3}S + P & 0 \\ 0 & 0 & -\frac{1}{3}S - P \end{pmatrix}. \quad (1.3)$$

### 1.3 Phenomenological free energy

In this section we give a brief summary of the phenomenological free energy, which can be minimised to study nematic phases. The majority of numerical work discussed in later chapters is based on this mean-field approach. A more detailed description can be found elsewhere [6, 12, 13].

The basic idea of Landau-de Gennes calculations is to express the phenomenological free energy and minimise it with respect to  $\mathbf{Q}$  in order to find the equilibrium structure of the nematic field. Depending on the chosen initial condi-



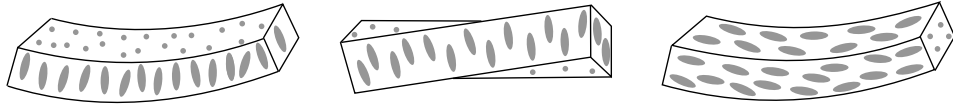


Figure 1.3: Schematic sketches of the three basic deformation modes in a liquid crystal: Splay, twist and bend.

tions, stable as well as unstable configurations can be explored. The Landau-de Gennes free energy functional can be divided into three main parts: the bulk, the elastic and the surface free energy density. In addition to the bulk and elastic free energy, terms can be added to account for dielectric coupling [13] or surface anchoring at particles' and containers' surfaces [14]. The free energy volume density  $f_{\text{phase}}$  can be written as

$$f_{\text{phase}} = \frac{1}{2}a(T - T_{\text{NI}})Q_{ij}Q_{ji} + \frac{1}{3}BQ_{ij}Q_{jk}Q_{ki} + \frac{1}{4}C(Q_{ij}Q_{ji})^2, \quad (1.4)$$

where  $a, B, C$  are phenomenological material coefficients,  $T$  is the temperature and  $T_{\text{NI}}$  is the supercooling temperature. Summation over repeated indices is assumed. Equation (1.4) is a Landau expansion correct up to fourth order taking into account the invariants of the nematic order tensor.

Each deformation of a liquid crystal increases its total energy. Assuming these deformations vary slowly in space, i.e. for large wavelength distortions, they can be described using continuum elastic theory. Any elastic deformation can be decomposed into three basic deformation modes: splay, twist and bend, shown in Fig. 1.3. The elastic free energy  $f_{\text{grad}}$  can be expressed in terms of second order derivatives of  $\mathbf{Q}$

$$f_{\text{grad}} = \frac{1}{2}L_1 \frac{\partial Q_{ij}}{\partial x_k} \frac{\partial Q_{ij}}{\partial x_k} + \frac{1}{2}L_2 \frac{\partial Q_{ij}}{\partial x_j} \frac{\partial Q_{ik}}{\partial x_k} + \frac{1}{2}L_3 Q_{ij} \frac{\partial Q_{kl}}{\partial x_i} \frac{\partial Q_{kl}}{\partial x_j}, \quad (1.5)$$

where  $L_1, L_2$  and  $L_3$  are elastic constants.  $f_{\text{grad}}$  can be rewritten in terms of the director field  $\hat{\mathbf{n}}(\mathbf{r})$  for uniaxial nematics in the Frank-Oseen form as

$$f_{\text{grad}}^{\text{FO}} = \frac{1}{2}K_1(\nabla \cdot \hat{\mathbf{n}})^2 + \frac{1}{2}K_2(\hat{\mathbf{n}} \cdot \nabla \wedge \hat{\mathbf{n}})^2 + \frac{1}{2}K_3 \left| \hat{\mathbf{n}} \wedge (\nabla \wedge \hat{\mathbf{n}}) \right|^2. \quad (1.6)$$

where  $K_1, K_2$  and  $K_3$  are the splay, twist and bend Frank elastic constants respectively. Note that higher order terms are neglected. The elastic constants in Equation (1.5) are directly related to the Frank elastic constants with  $L_1 = (K_3 + 2K_2 - K_1)/9S^2$ ,  $L_2 = 4(K_1 - K_2)/9S^2$  and  $L_3 = 2(K_3 - K_1)/9S^2$ . In the mean-field approach the one-elastic-constant approximation is commonly used, which assumes

that the splay, twist and bend elastic constants are equivalent  $K = K_1 = K_2 = K_3$ . However this is a rather crude assumption. We show in Chapter 3 that for some systems and state points the bend Frank elastic constant is eight times higher than the corresponding twist elastic constant.

This phenomenological approach complements molecular simulations. Compared to molecular simulations it has the advantage to allow access to large length scales (micrometre regime), similar to the length scales accessible in experiments. Furthermore it does not require details about the molecular interactions. However it also has several disadvantages. The free energy minimisation only finds one state at a time and therefore it is possible to miss other (meta)stable configurations of a system. Since continuum theory can only describe distortions with wavelength large compared to the size of the LC molecules, systems below this limit, for example nanoparticle inclusions in nematics, can only be studied using molecular simulations.

## 1.4 Elastic properties of nematic liquid crystals

Using continuum elastic theory each elastic deformation varying slowly in space can be described by the three basic deformation modes described in Section 1.3. To quantify these thermal equilibrium fluctuations it is convenient to define a new orthogonal Cartesian axis system with  $(\hat{e}_1, \hat{e}_2, \hat{e}_3)$ , where  $\hat{e}_3$  is along the director  $\hat{\mathbf{n}}$ . In this system  $\hat{\mathbf{n}} = (0, 0, 1)$  and  $(n_1, n_2, 0)$  describe small fluctuations of the director. When studying these fluctuations in reciprocal space, the wave vector  $\mathbf{k}$  can be restricted to lie in the  $\hat{e}_1$ - $\hat{e}_2$  plane, i.e.  $\mathbf{k} = (k_1, 0, k_3)$ . In the following we derive the second derivatives of the director field  $\hat{\mathbf{n}}(\mathbf{r})$  used in the Frank free energy expression in Equation (1.6). A schematic of the director fluctuations for the different deformation modes is shown in Fig. 1.4. The fluctuations of the director field may be expanded in Fourier components

$$n_m(\mathbf{r}) = \frac{1}{V} \sum_{\mathbf{k}} \tilde{n}_m(\mathbf{k}) \exp(i\mathbf{k} \cdot \mathbf{r}) , \quad m = 1, 2 , \quad (1.7a)$$

$$\tilde{n}_m(\mathbf{k}) = \int_V d\mathbf{r} n_m(\mathbf{r}) \exp(-i\mathbf{k} \cdot \mathbf{r}) , \quad (1.7b)$$

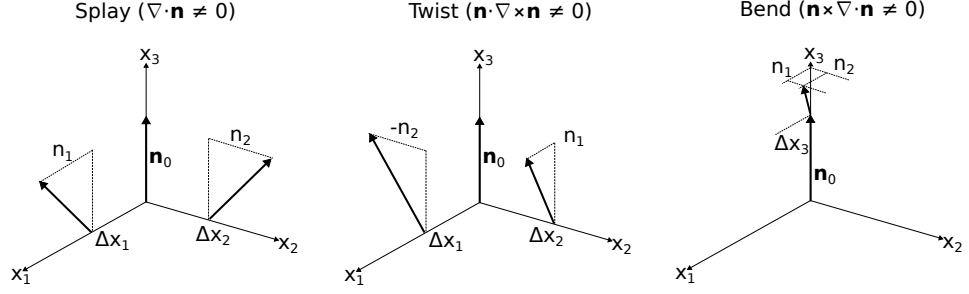


Figure 1.4: Schematic of the three basic deformation modes in a nematic liquid crystal [12].  $n_1$  and  $n_2$  are small deviations from the director assuming that the initial director  $n_0$  is along  $\hat{x}_3$ .

where  $V$  is the volume. The spatial derivatives of  $\hat{n}(\mathbf{r})$  used in Equation (1.6) can be derived as

$$\begin{aligned}\nabla \cdot \hat{n}(\mathbf{r}) &= \frac{1}{V} \sum_{\mathbf{k}} i k_1 \tilde{n}_1(\mathbf{k}) \exp(i\mathbf{k} \cdot \mathbf{r}), \\ \nabla \times \hat{n}(\mathbf{r}) &= \frac{1}{V} \sum_{\mathbf{k}} (-i k_3 \tilde{n}_2(\mathbf{k}), i k_3 \tilde{n}_1(\mathbf{k}), i k_1 \tilde{n}_2(\mathbf{k})) \exp(i\mathbf{k} \cdot \mathbf{r}), \\ \hat{n}(\mathbf{r}) \cdot \nabla \times \hat{n}(\mathbf{r}) &= \frac{1}{V} \sum_{\mathbf{k}} i k_1 \tilde{n}_2(\mathbf{k}) \exp(i\mathbf{k} \cdot \mathbf{r}), \\ \hat{n}(\mathbf{r}) \times (\nabla \times \hat{n}(\mathbf{r})) &= \frac{1}{V} \sum_{\mathbf{k}} -i k_3 (\tilde{n}_1(\mathbf{k}), \tilde{n}_2(\mathbf{k}), 0) \exp(i\mathbf{k} \cdot \mathbf{r}).\end{aligned}$$

These expressions are particularly simple in this coordinate system, because  $n_3 = 0$  and  $k_2 = 0$ . Applying Parseval's theorem, which is given by

$$\int_V d\mathbf{r} |\phi(\mathbf{r})|^2 = \frac{1}{V} \sum_{\mathbf{k}} |\tilde{\phi}(\mathbf{k})|^2,$$

to Equation (1.6) leads to

$$\begin{aligned}\Delta \mathcal{F} &= \frac{1}{V} \sum_{\mathbf{k}} \frac{1}{2} K_1 k_1^2 |\tilde{n}_1(\mathbf{k})|^2 + \frac{1}{2} K_2 k_1^2 |\tilde{n}_2(\mathbf{k})|^2 + \frac{1}{2} K_3 k_3^2 (|\tilde{n}_1(\mathbf{k})|^2 + |\tilde{n}_2(\mathbf{k})|^2) \\ &= \frac{1}{V} \sum_{\mathbf{k}} \frac{1}{2} (K_1 k_1^2 + K_3 k_3^2) |\tilde{n}_1(\mathbf{k})|^2 + \frac{1}{2} (K_2 k_1^2 + K_3 k_3^2) |\tilde{n}_2(\mathbf{k})|^2.\end{aligned}\quad (1.8)$$

One can see that the first term is related to splay and bend ( $K_1$  and  $K_3$ ) and the second term to twist and bend ( $K_2$  and  $K_3$ ) deformations. Equipartition of energy

yields

$$\left\langle |\tilde{n}_1(\mathbf{k})|^2 \right\rangle = \frac{V k_B T}{K_1 k_1^2 + K_3 k_3^2}, \quad \left\langle |\tilde{n}_2(\mathbf{k})|^2 \right\rangle = \frac{V k_B T}{K_2 k_1^2 + K_3 k_3^2}. \quad (1.9)$$

Here  $k_B$  is the Boltzmann constant and  $T$  the temperature. Hence the Frank elastic constants  $K_1$ ,  $K_2$  and  $K_3$  can be extrapolated directly from the equilibrium fluctuations for small wave vectors ( $k \rightarrow 0$ ). The director fluctuations  $(n_1, n_2, 0)$  are directly proportional to the elements  $Q_{13}$  and  $Q_{23}$

$$\tilde{n}_1 = \frac{\tilde{Q}_{13}}{\frac{3}{2}S}, \quad \tilde{n}_2 = \frac{\tilde{Q}_{23}}{\frac{3}{2}S}. \quad (1.10)$$

In Chapter 3 we apply Equations (1.9) and (1.10) to data of order tensor fluctuations obtained from molecular simulations. The fluctuations were fitted to a range of small wave vectors and the elastic constants were extrapolated.

## 1.5 Dynamical properties of nematic liquid crystals

A particularly interesting feature of liquid crystals are their flow properties. A first full description of the dynamics of a nematic liquid crystal was proposed by Ericksen [15], which was later completed by Leslie [16]. A purely hydrodynamic formulation was given by Forster et al. [17]. Detailed descriptions and examples for application of this so-called Ericksen-Leslie theory can be found elsewhere [6, 9, 18, 19]. In the following a brief introduction into the hydrodynamics of nematics, commonly referred to as nematodynamics, is given. To start with we consider an ordinary isotropic fluid, which can be described by

$$\nabla \cdot (\rho \mathbf{v}) = -\dot{\rho}, \quad (1.11)$$

where  $\rho$  is the density and  $\mathbf{v}$  the velocity. For an incompressible fluid  $\rho(\mathbf{r}, t) = \text{const.}$  and hence the above expression leads to  $\nabla \cdot \mathbf{v} = 0$ . Newton's law describes the motion of the fluid elements due to a force  $\mathbf{f}$

$$\rho \frac{d\mathbf{v}}{dt} = \mathbf{f}. \quad (1.12)$$

The total force  $\mathbf{f}$  is a combination of the pressure gradient  $-\nabla \rho$ , viscous forces  $\mathbf{f}_{\text{vis}}$  and external fields  $\mathbf{f}_{\text{ext}}$ .

$$\rho \left[ \frac{\partial \mathbf{v}}{\partial t} + (\nabla \cdot \mathbf{v}) \mathbf{v} \right] = -\nabla \rho + \mathbf{f}_{\text{vis}} + \mathbf{f}_{\text{ext}}. \quad (1.13)$$

We now consider a fluid without any external fields. A stress tensor  $\sigma$  can be defined, such that a force can be expressed as

$$f_i = \frac{\partial}{\partial x_j} \sigma_{ij} . \quad (1.14)$$

Summation over repeated indices is implied. Equation (1.13) can be reformulated in terms of the stress tensor

$$\rho \left[ \frac{\partial v_i}{\partial t} + v_j \frac{\partial v_i}{\partial x_j} \right] = - \frac{\partial p}{\partial x_i} + \frac{\partial \sigma_{ij}}{\partial x_j} , \quad (1.15)$$

where  $p$  is the pressure. The stress tensor is proportional to the linear gradients of the velocity

$$\sigma_{ij} = \eta \left( \frac{\partial v_j}{\partial x_i} + \frac{\partial v_i}{\partial x_j} \right) , \quad (1.16)$$

where  $\eta$  is the viscous coefficient. To describe the hydrodynamics of a nematic the stress tensor has to be expanded to account for the orientation and rotation of the director in addition the velocity gradients. Ericksen [15] and Leslie [16] derived

$$\sigma_{ij} = \alpha_1 n_k n_l A_{kl} n_i n_j + \alpha_2 n_i n_j + \alpha_3 n_j n_i + \alpha_4 A_{ij} + \alpha_5 n_k A_{kj} + \alpha_6 n_j n_k A_{ki} , \quad (1.17)$$

where  $A_{ij}$  is defined as  $\frac{1}{2}(v_{j,i} + v_{i,j})$ . The fourth term  $\alpha_4 A_{ij}$  corresponds to the isotropic contribution (see Equation (1.16)). The six  $\alpha$  coefficients are referred to as Leslie coefficients. Parodi [20] showed that  $\alpha_2 + \alpha_3 = \alpha_6 - \alpha_5$  leaving five independent coefficients. Similarly to Equation (1.12) conservation laws lead to the balance equation

$$\rho_1 \ddot{n}_i = g_i + \pi_{ji,j} , \quad (1.18)$$

where  $\rho_1$  is a material constant with the dimensions of moment of inertia density,  $g_i$  is the intrinsic director body force,  $\pi_{ji}$  the couple stress and  $n_i$  the director. Similarly to  $A_{ij}$  it is useful to define the vorticity  $B_{ij} = \frac{1}{2}(v_{i,j} - v_{j,i})$  and the co-rotational time flux of the director

$$N_i = \dot{n}_i - B_{ij} n_j \quad (1.19)$$

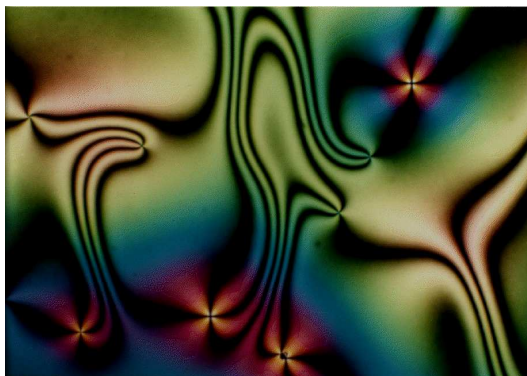


Figure 1.5: Schlieren texture in a liquid crystal. Courtesy: National Science Foundation [4].

We can separate  $\sigma$  and  $g$  into reactive and dissipative parts:  $\sigma_{ji} = \sigma_{ji}^R + \sigma_{ji}^D$  and  $g_j = g_j^R + g_j^D$ , while  $\pi$  is purely reactive. Some derivation yields

$$\begin{aligned}\sigma_{ji}^R &= -p\delta_{ji} - \frac{\partial f}{\partial n_{k,j}}n_{k,i} \\ g_i^R &= \gamma n_i - \beta_j n_{i,j} - \frac{\partial f}{\partial n_i} \\ \pi_{ji} &= \beta_j n_i + \frac{\partial f}{\partial n_{i,j}} \\ g_i^D &= \lambda_1 N_i + \lambda_2 n_j A_{ji}\end{aligned}$$

where  $\lambda_1 = \alpha_2 - \alpha_3$  and  $\lambda_2 = \alpha_5 - \alpha_6$  and  $\gamma$  and  $\beta_j$  are arbitrary constants. By choosing the same coordinate system as in Section 1.4 these can be derived further and simplified leading to the equations used in Chapter 4.

## 1.6 Topological defects

Topological defects can be points, lines or walls where the order parameter of interest in a system is undefined. Topological defects can be observed in numerous areas of physics; they are especially important in liquid crystals, because it is almost impossible to have an entirely defect-free liquid crystal. Defects in liquid crystals can significantly change the properties of the entire system and hence it is crucial to understand the behaviour of these defects. In Fig. 1.5 the so-called Schlieren texture of a LC sample between crossed polarisers is shown. The colour variation observed is due to the variation of the birefringence throughout the sample. Additionally one can see dark brushes across the sample. These brushes are black, because

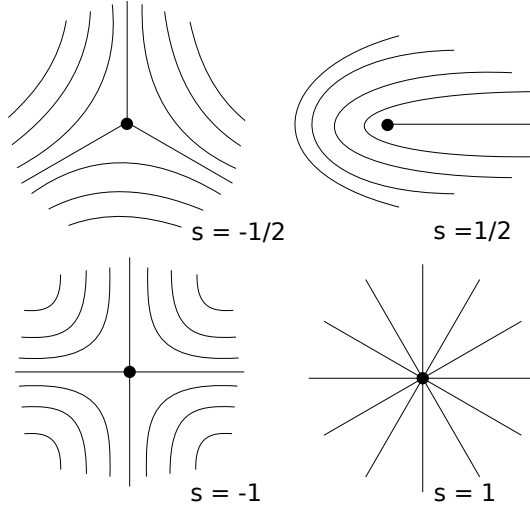


Figure 1.6: Sketch of nematic fields near disclination lines in 2D and their corresponding winding number  $s$ .

the director in those regions is either parallel or perpendicular to the polariser or analyser. In the region where the dark brushes intersect, the defect core, the director is discontinuous. Within the defect core the LC is melted into the isotropic phase and the molecules have no preferred orientation. At a molecular level this corresponds to high fluctuations of the molecular orientation. This is commonly referred to as ‘frustrated’ molecules. Within the defect region the order parameter  $S$  drops significantly and biaxiality is observed [21]. This local perturbation of the long-range orientational order is called a topological defect. Defects can arise due to fast cooling, external perturbations or, at very low concentrations, thermal fluctuations as well as the presence of particle inclusions.

In nematics two types of defects are found, namely point defects, also called hedgehogs, and line defects, commonly referred to as disclinations. A point defect can be characterised by a topological charge, which specifies the integer number of times the unit sphere is wrapped by the director on any surface enclosing the defect core [22]. Due to the  $-\hat{n} \leftrightarrow \hat{n}$  symmetry, we cannot distinguish between a source and a sink. By convention the topological charge is chosen to be positive. A disclination line can be characterised by a winding number  $s$ , which describes the symmetry of the surrounding director field. It can be described as the ratio  $s = \alpha/(2\pi)$ , where  $\alpha$  is the angle, by which the director rotates along a closed loop surrounding the disclination line [22]. All disclinations, where  $s$  is a half-integer, are topologically equivalent and likewise all those, where  $s$  is a full integer. The corresponding director fields are sketched in Fig. 1.6 for a variety of different defects

in 2D. Note that lines in form of closed loops can shrink and convert into point defects, and vice versa, so that there is a subtle topological interplay between them.

In Schlieren textures we commonly observe two or four dark brushes arising from each defect core (see Fig. 1.5). Higher numbers, as long as they are multiples of two, are possible. The number of brushes is directly related to the winding number  $s$ . Because the analyser and polarisers directions are rotated by  $\pi/2$  relative to each other, each brush must correspond to a director rotation of  $\pi/2$ . We can identify the strength  $s$  by multiplying the number of brushes arising from a defect core by  $\pm 1/4$ . To identify the sign one can rotate the polariser and observe the rotation of the brushes. The sign is negative if the brushes counter-rotate and positive otherwise. Low order defects are energetically favourable, because the energy associated with a disclination line is proportional to  $s^2$ . The energy is also proportional to the length of the disclination line, i.e. stretching the line will result in an increase in energy.

A spherical particle inserted into a nematic liquid crystal induces the creation of defects [13, 23–25]. The defects are caused by the competition of the LC molecules trying to ‘pack’ around the particle and trying to align along the director. Particle inclusions effectively act as point defects. Their corresponding topological charge is determined by the orientation of the director field along their surface. Since the total topological charge in a closed system has to be zero, each particle inclusion is accompanied by a defect in the liquid crystal. In experiments the particle inclusions are often materials such as silica, glass, polystyrene microspheres or liquid droplets. The surface of the inserted particle is chemically treated to control the anchoring of the LC molecules around it. The major axes of the LC molecules often arrange either perpendicular or parallel to the surface of the particle. These anchoring conditions are referred to as homeotropic and planar anchoring respectively. Similarly, the surfaces of the LC container can be treated to enforce different types of anchoring. Consequently, in most real systems the direction of the director will be imposed by the walls, even if its direction is generally arbitrary.

An interesting question is how exactly the director field deforms around the inclusion. This depends on many different factors, for example the size of the particle, its surface anchoring strength, boundary conditions as well as external fields [13, 24, 26]. Four different defect structures have been observed in experiments. A sketch of their corresponding director fields in 2D is shown in Fig. 1.7. For particles with homeotropic surface anchoring, the deformation is either of dipolar or quadrupolar structure. The dipolar structure, often referred to as hyperbolic hedgehog or satellite defect, is characterised by a hyperbolic point defect. The quadrupolar defect, also called Saturn ring defect, consists of a  $-1/2$  disclination



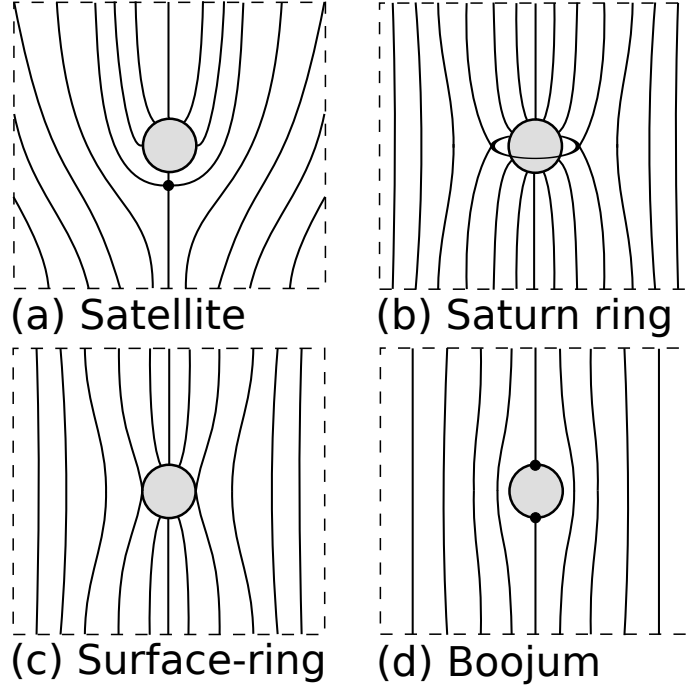


Figure 1.7: Sketch of director field around a particle inclusion: (a) satellite defect, (b) Saturn ring defect, (c) Surface-ring defect and (d) boojum defect.

line looping around the equator of the particle with respect to the director. The satellite and Saturn ring defect are topologically equivalent. One can think of the Saturn ring being transformed to the satellite defect by moving the disclination line away from the equator, until it collapses in one point. Theoretical and experimental work as well as Monte Carlo simulations, suggest that satellite defects tend to be stable for large particles and that the Saturn ring is stable for small particles [23, 27–29]. Attempts were made to estimate the threshold for which the dipolar structure becomes unstable as a function of particle size. However the description did not account sufficiently for very strong surface anchoring and strong confinement. For example Škarabot and Mušević [30] and Ryzhkova and Mušević [31] observed Satellite defects for particles as small as 125 nm and 35 nm respectively due to very strong surface anchoring. We address the question of satellite versus Saturn ring in Chapter 5 by employing molecular dynamics to study a range of particle sizes.

For particles with very weak homeotropic anchoring a Surface-ring defect is predicted, which is very similar to the Saturn ring; however the core of the disclination line sits directly on the surface of the particle. Particles with planar anchoring only have one known defect structure, which is quadrupolar and generates two  $-1/2$  antipodal surface defects called ‘boojums’. Boojum defects have been studied using

Landau-de Gennes free energy minimisation [32], which predicts that in 3D systems one can distinguish three different types: the single, split and double boojum. The single boojum, which is a  $-1$  point defect, arises around small particles with weak anchoring and is stable at high temperatures. For large particles with strong anchoring the boojum defect splits into two  $+1/2$  point defects, which are connected by a disclination line. They usually arise at low temperatures. The double boojum is an intermediate state where the defect core splits, but the disclination line is not fully developed. The three types can be smoothly transformed from one to another by varying the anchoring strength, temperature or particle radius.

So far we solely focused on topological defects due to single particles inserted into a nematic host. In the following, we focus on pair interactions of particle inclusions [33] as well as whole clusters of particles. Due to the anchoring of the liquid crystal molecules at the surface of the inserted particle, the director field is distorted, which induces long-range structural forces between particles. These structural forces can be regarded as effective elastic forces, which try to minimise the perturbation of the director field caused by the inclusion. When two dipoles are brought into close vicinity, they can attract each other and it was observed experimentally as well as in numerical calculations that they can form chains within the nematic. This attraction is due to the particles trying to share defect regions to minimise the total free energy. Fig. 1.8 (a-f) shows the corresponding micrographs and sketches of the director fields for two dipoles. Two collinear dipoles attract each other and form linear chains along the director [34, 35], if their dipoles are pointing in the same direction. Otherwise they repel each other. It was shown that the binding energies for two dipoles can be as strong as  $1000k_B T$  for micron-sized particles [28, 36, 37]. Two antiparallel dipoles attract each other sideways with respect to the director. The total free energy is minimised when the dipoles are tilted at an angle with respect to the director. In contrast, parallel dipoles repel each other along this direction. Poulin et al. [38] studied the inter-particle interactions for small water droplets, which exhibit a dipolar structure, as a function of particle separation. These droplets form chain-like structures inside nematics, with attractive interactions at long distance and repulsive ones at short distances. This interaction behaviour was successfully reproduced using Monte Carlo simulations [39]. The simulation results suggest that the overall interaction strength increases with increasing particle size. Attempts have been made to study the influence of the anchoring effects on the aggregation of nanoparticles in nematics using simulations [40].

Two quadrupoles only have one stable configuration, shown in Fig. 1.8 (g-i), in which the two quadrupoles prefer to sit at a fixed angle with respect to the

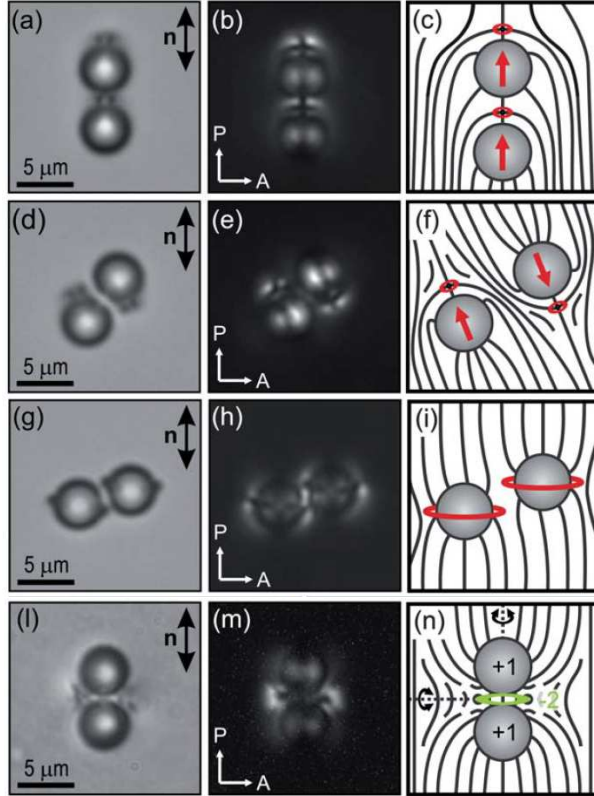


Figure 1.8: Silica microspheres with homeotropic anchoring embedded in a nematic host. Left column shows micrographs; Centre column shows micrographs under crossed crossed polarisers; Right column shows sketches of the director field: (a-c) Two parallel dipoles, (d-f) two antiparallel dipoles, (g-i) two quadrupoles and (l-n) bubble gum defect. Reproduced from [5] with permission from the Royal Society of Chemistry.

director. Particles further than the equilibrium distance apart attract each other [41]. These observations were successfully reproduced using continuum theory [27] as well as molecular dynamics simulations [33]. The binding energies of elastic quadrupoles are significantly weaker ( $\approx 100k_{\text{B}}T$ ) [42, 43] than the ones of elastic dipoles. In two-dimensional systems quadrupoles can assemble in form of zig-zag chains. If two quadrupoles are forced together along a straight line perpendicular to the director, both Saturn rings bend to minimise the total free energy.

Fig. 1.8 (l-n) shows the bubble gum structure, which can arise if two anti-dipoles are forced into close vicinity [35]. This escaped -1 loop was found to be highly metastable and has only been observed naturally arising in chiral nematic cells [44]. Embedded in nematics the bubble-gum shows almost no interactions.

For two particles with planar anchoring only attractive structural forces are observed; hence two boojums slowly approach each other. At very close distances they are strongly bound due to the particles sharing their inner point defect. This was observed in experiments and reproduced by simulations [32]. The forces between two boojums as a function of angle show large discrepancies between theoretical and experimental results and are not fully understood. Eskandari et al. [45] showed that two particles, one with homeotropic and one with planar anchoring, attract each other. Their interactions only become repulsive for very small particle separation.

In Chapter 5 we will present molecular simulation results of single particle inclusions in nematics, as well as results of particle pair-interactions due to the long-range structural forces inside the nematic.

The attractive long-range interactions between different inclusions can be utilised for the self-assembly of three-dimensional colloidal liquid crystals [30, 37, 46–49]. These clusters can be formed by dipoles or quadrupoles and they were also observed for binary mixtures of quadrupoles and dipoles. The clusters formed by dipoles seem to be somewhat more robust, whereas quadrupolar ones slowly decay over time. Dipolar clusters are formed by one-dimensional chains of parallel dipoles along the director, which are surrounded by neighbouring chains with their dipoles pointing in the opposite direction. Apart from cluster formation, the structural forces can also lead to particle trapping at LC boundaries [50] as well as colloidal lattice formations inside nematic LC droplets [51]. The interactions and self-assembly of nanoparticles in nematic LC is still rather unexplored. The main difficulty is the visualisation and tracking of such small particles.

For two quadrupoles in close vicinity entangled defect structures were observed to arise spontaneously. Here a single defect line winds around both particles leading to an effective binding energy. In Chapter 6 we show that such structures

can be observed in molecular simulations and compare them to experimental observations and mean-field calculations.

Recent studies [52–55] have focused on anisotropic particle inclusion. Using novel microfabrication methods, experimental work was carried out focusing on anisotropic particles like micro-rods [56] and toroids [57] in nematic liquid crystals. Experimental results suggest a strong dependence of the inter-particle interaction on the shape [58–62] opening up a new route to design novel materials.

## 1.7 Scope of this thesis

In Chapter 2 we introduce the simulation methods used. The remaining chapters are structured as follows.

**Chapter 3:** In this chapter we present molecular dynamics calculations of the Frank elastic constants in nematic liquid crystals. We study two variants of the Gay-Berne potential, and use system sizes of half a million molecules, significantly larger than in previous studies of elastic behaviour. Equilibrium orientational fluctuations in reciprocal ( $\mathbf{k}$ -) space were calculated, to determine the elastic constants by fitting at low  $|\mathbf{k}|$ . The importance of the system size was investigated.

**Chapter 4:** In this chapter the dynamics of the Gay-Berne nematic were studied by calculating time correlation functions of components of the order tensor, together with associated components of the velocity field, for a set of wave vectors  $\mathbf{k}$ . We found exponential decay for splay and twist correlations, and oscillatory exponential decay for the bend correlation. A comparison with the predictions of nematodynamics reveals that propagating bend fluctuations may be observable in some experimental systems.

**Chapter 5:** We studied the formation of topological defects caused by nanoparticle inclusions in nematics and observed Saturn ring, boojums and satellite defects arise. The effects of particle size and surface anchoring on the defect structure were analysed. Furthermore nanoparticle interactions caused by the structural elastic forces in the nematic were investigated.

**Chapter 6:** We present molecular dynamics simulations of nanoparticles in close vicinity. Depending on the particles' radii and their separation entangled defects were observed, where two (or more) particles are surrounded by single disclination line. The different entanglements were categorised and the dynamics of the rearrangement from one configuration to another were investigated.

**Chapter 7:** A single disclination line was stabilised in a molecular simulation by applying an external field near the boundaries of the simulation box. The ratio of the line tension of the disclination line and the viscous drag of the liquid crystal host were calculated from the relaxation times of the fluctuations of the line in reciprocal space.

**Chapter 8:** In this chapter we studied the interactions of a single disclination line with a nearby nanoparticle. When the position of the nanoparticle is fixed, we observed the disclination line to bend towards it to minimise total free energy. In addition, some nanoparticles became entangled by the defect line. Once the particle was released it was strongly attracted towards the centre of the simulation box allowing the defect line to be straight. This interaction was found to be strongly depending on the nanoparticles position with respect to the  $-1/2$  director field of the defect. For two nanoparticles in close vicinity of the disclination line attractive as well as repulsive interactions were discovered depending on their initial positions.

## Chapter 2

# Computer simulations

Most problems in statistical mechanics are not soluble; sometimes it is not even possible to find an approximate analytical solution. This is where computers come in useful to provide us with numerical approximations. A major advantage of simulations compared to experiments is that, at all times, we have full information about the system. Therefore simulations can give insight into experiments and can help us understand the underlying dynamics; they also provide a powerful tool to test theories.

One of the simplest computer simulations is based on lattice models. Introducing a lattice reduces the number of degrees of freedom, which leads to large savings in computer time. The well known Ising model consists of a lattice of spins, that can be in two states ‘up’ or ‘down’. Only nearest neighbours interact with each other. The Ising model can be extended to the classical Heisenberg model, by replacing the spin dipoles with freely rotating unit vectors. Both models have been widely used to study phase transitions. The well known Lebwohl-Lasher lattice model [63] is a modification of the classical Heisenberg model. The nearest-neighbour interaction energy is given by  $U_{ij} \propto -(\frac{3}{2} \cos^2(\theta_{ij}) - \frac{1}{2})$ , where  $\theta_{ij}$  is the angle between the major axes of particle  $i$  and  $j$ . The Lebwohl-Lasher model has been successfully used to study liquid crystal (LC) systems [64–67]. However, lattice models are often too simplistic for more complex systems.

In hard particle models the particles are free to translate. To keep the interactions simple, the particles have an infinitely repulsive core. Onsager [68] predicted a nematic phase for extremely long hard rods. This was successfully reproduced in simulations [69], which indicates that the molecular shape plays the main role in the formation of liquid crystalline phases. Frenkel et al. [69] found the nematic phase to be stable for hard prolate ellipsoids with a more realistic length to width ratio

as small as three. For oblate particles the discotic phase forms, which is a nematic phase formed by disk-like particles. Later studies [70] revealed that hard particle models can also show biaxial phases. For hard spherocylinders with a length to width ratio of five, Frenkel [71] observed the smectic phase in addition to the nematic phase. The smectic phase appears because of the spherocylinders' shape, as well as its length.

Soft particle models tend to be more sophisticated by avoiding the infinitely repulsive hard core and by adding attractive forces. The most commonly used soft potential to simulate liquid crystals is the Gay-Berne potential [72], which will be introduced later in this chapter. At a much higher computational cost (usually compensated by reducing the number of molecules simulated to a few thousand) even atomistic simulations of liquid crystals can be realised with today's computer power. This approach aims to predict mesophase behaviour for real systems based on the knowledge of the molecular structure [73–77].

When modelling particle inclusions in nematic LC, molecular modelling has several advantages compared to mean-field approaches (see Section 1.3). It gives insight into the defect structure on a molecular level and shows the exact dynamics of the formation and rearrangement of such defects. Furthermore, the impact of thermal fluctuations can be observed in molecular simulations. Mostly, it was used in this thesis to allow particle inclusions of the size of a few nanometer. At this scale the phenomenological model becomes less reliable due to its mean-field character.

In the following Section 2.1 a brief account of computer simulations of liquid crystalline systems is given. In Section 2.3, the Gay-Berne soft interaction is introduced. All research presented in this thesis was simulated using Molecular Dynamics, which is introduced in Section 2.2. In Section 2.4 different visualisation methods of defects in liquid crystals are described, which are used throughout this thesis.

## 2.1 Computer Simulations of Liquid Crystals

Computer simulations have been widely used to study liquid crystalline systems. They have been employed, amongst others, to investigate bulk elastic constants [78–80], viscosities [81–83], phase transitions [84, 85], surface effects [86–90] and nanodroplets in solution [91–94]. Furthermore simulations showed that chiral nanostructures can impose chiral ordering in the bulk [95]. Molecular simulations successfully modelled the properties of twisted nematic cells [96]. Recently atomistic simulations [74] successfully reproduced liquid crystalline phase transitions and the



formation of several smectic phases. All-atom simulations were used to reproduce the aggregation of non-ionic chromonic liquid crystals in solution [76] and the formation of biaxial liquid crystals [77]. In more recent years topological defects in liquid crystals were studied using computer simulations. Several studies analysed the structure of the defect core on a molecular level [21, 97]. Another research interest is the effect of particle inclusions in nematics [98–100] as well as chiral LCs [101] for various surface anchoring conditions. Recent simulations analysed the torque on anisotropic particle inclusions [52] and the effect of flow on the defect created by spherical inclusions [102, 103]. Many studies were devoted to investigate the structural forces between particle inclusions in a nematic as a function of particle size and shapes, separation, angular distance and surface anchoring [33, 39–41, 104–107]. Molecular simulations were also used to investigate the trapping of nanoparticles in disclination lines [67].

## 2.2 Molecular Dynamics (MD)

Molecular dynamics simulations are commonly used to study the equilibrium and transport properties of classical many-body systems [108]. The main idea of MD is that for any system with a fixed number of particles, with given initial positions  $\mathbf{r}_i(0)$  and momenta  $\mathbf{p}_i(0)$  as well as a known force field, we can compute the particles' trajectories  $[\mathbf{r}_i(t), \mathbf{p}_i(t)]$  over time  $t$  by solving Newton's equation of motion

$$m_i \ddot{\mathbf{r}}_i = \mathbf{f}_i, \quad (2.1)$$

where  $m_i$  is the mass of the particle  $i$ ,  $\mathbf{r}_i$  its position and  $\mathbf{f}_i$  the force acting on the particle in Cartesian coordinates. So how does the system evolve over time? Firstly, we have to calculate the force and torque acting on each particle for the given force field [109]. Note that for this section only we deviate from our usual notation for the orientation vector  $\mathbf{u}$  and use  $\mathbf{e}$  instead. In the following  $\dot{\mathbf{e}}$  denotes the time derivative of  $\mathbf{e}$ , i.e.  $\mathbf{u}_i = \dot{\mathbf{e}}_i$ . The force on particle  $i$  due to  $j$  is

$$\mathbf{f}_{ij} = -\frac{\partial U_{ij}}{\partial \mathbf{r}_{ij}} \quad (2.2)$$

and the torque on  $i$  due to  $j$  is

$$\boldsymbol{\tau}_{ij} = -\mathbf{e}_i \times \frac{\partial U_{ij}}{\partial \mathbf{e}_i} \equiv -\mathbf{e}_i \times \mathbf{g}_i, \quad (2.3)$$

where  $\mathbf{g}_i$  is referred to as ‘gorque’. Note that  $\mathbf{f}_{ij} = \mathbf{f}_{ji}$ , but that  $\boldsymbol{\tau}_{ij} \neq \boldsymbol{\tau}_{ji}$ . Secondly, we have to numerically integrate Newton’s equation of motion (Eq. 2.1).

### 2.2.1 Integration of the equations of motion for linear molecules

In the following we describe the Velocity Verlet algorithm to integrate the translational and rotational equations of motion [110]. There are several other methods for integrating the rotational equation of motion based on the rotation matrix [111] or Quaternions [112]. In this description we restrict ourselves to linear molecules with two rotational degrees of freedom. Here the rotation occurs about the two axes perpendicular to  $\mathbf{e}$  with the same moment of inertia  $I$  and there is no rotation about  $\mathbf{e}$  itself. The derivative of  $\mathbf{u}_i$  is given by

$$\dot{\mathbf{u}}_i = \mathbf{g}_i^\perp + \lambda \mathbf{e}_i, \quad (2.4)$$

where  $\mathbf{g}_i^\perp$  is the component of the gorque perpendicular to the molecular axis  $\mathbf{e}_i$  and is given by

$$\mathbf{g}_i^\perp = \frac{\mathbf{g}_i - (\mathbf{g}_i \cdot \mathbf{e}_i) \mathbf{e}_i}{I_i}, \quad (2.5)$$

where  $I_i$  is the moment of inertia. For every position and momentum update, the following few steps have to be repeated. The velocity  $\mathbf{v}_i$  and time derivative of the orientation  $\mathbf{u}_i$  have to be advanced by a half-step  $\Delta t/2$

$$\mathbf{v}_i \left( t + \frac{\Delta t}{2} \right) = \mathbf{v}_i(t) + \mathbf{a}_i(t) \frac{\Delta t}{2}, \quad (2.6a)$$

$$\mathbf{u}_i \left( t + \frac{\Delta t}{2} \right) = \mathbf{u}_i(t) + \left( \mathbf{g}_i^\perp + \lambda_i \mathbf{e}_i \right) \frac{\Delta t}{2}. \quad (2.6b)$$

The Lagrange multiplier  $\lambda_i$  can be derived from the constraint  $\mathbf{e}_i \cdot \mathbf{e}_i = 1$ . In the next step, the velocity and orientation vector are advanced by a full time step

$$\mathbf{e}_i(t + \Delta t) = \mathbf{e}_i(t) + \mathbf{u}_i \left( t + \frac{\Delta t}{2} \right) \Delta t, \quad (2.7a)$$

$$\mathbf{r}_i(t + \Delta t) = \mathbf{r}_i(t) + \mathbf{v}_i \left( t + \frac{\Delta t}{2} \right) \Delta t. \quad (2.7b)$$

The forces and gorques (or alternatively the acceleration  $\mathbf{a}$  and component perpendicular to the gorque  $\mathbf{g}^\perp$ ) can now be evaluated for the full time step. To complete

the time step  $\mathbf{v}$  and  $\mathbf{u}$  are calculated for the second half-step

$$\mathbf{v}_i(t + \Delta t) = \mathbf{v}_i\left(t + \frac{\Delta t}{2}\right) + \mathbf{a}_i(t + \Delta t) \frac{\Delta t}{2}, \quad (2.8a)$$

$$\mathbf{u}_i(t + \Delta t) = \mathbf{u}_i\left(t + \frac{\Delta t}{2}\right) + \left(\mathbf{g}_i^\perp(t + \Delta t) - \lambda'_i \mathbf{e}_i(t + \Delta t)\right) \frac{\Delta t}{2}. \quad (2.8b)$$

The Lagrange multiplier  $\lambda'_i$  can be derived from the constraints  $\mathbf{e}_i \cdot \mathbf{e}_i = 1$  and  $\mathbf{e}_i \cdot \mathbf{u}_i = 0$ .

The accuracy of the integration of Newton's equation is important. The more accurate the integration, the larger the time step that can be used and hence the force has to be evaluated less often for a fixed simulation time. Several other integration algorithms for Newton's equation exist as well as some higher order schemes, which include more terms of the Taylor expansion, if a higher accuracy is desired [108].

### 2.2.2 Linking simulations and experiments

Due to small integration errors, the particles' trajectories will diverge exponentially from the real trajectories in every MD simulation. However macroscopic properties are not affected by this divergence since they are ensemble averages. To assure correct averaging, the particles' trajectories have to stay on a constant-energy hypersurface. Indeed, it can be shown that the trajectories conserve a 'pseudo'-Hamiltonian, which, for sufficiently small time steps, differs by only a small amount from the real Hamiltonian.

In order to link experiments and simulations we have to be able to express the macroscopic properties, e.g. viscosities (Leslie coefficients), orientational elasticity (Frank elastic constants) or substrate-LC orientational coupling (anchoring coefficients) in terms of the microscopic simulation details. By averaging over a very long time we can obtain these macroscopic properties from simulation using statistical mechanics. Because simulations are of finite length, the results are always subject to a statistical error, which can be estimated [108, 113].

If we evolve the system over time, we simulate a so-called microcanonical ensemble, where the total number of molecules  $N$ , the volume  $V$  and the total energy  $E$  are conserved. This is also referred to as  $NVE$  simulation. Especially when equilibrating a system, it might be desirable to control the temperature  $T$ . This can be achieved by either periodically reselecting velocities at random from the Maxwell-Boltzmann distribution [114], or alternatively the system can be coupled to a thermal reservoir that heats or cools the system to reach the desired temperature

[115, 116]. This ensemble is called the canonical, or *NVT*, ensemble. The extension of the equations of motion for the *NVT* ensemble can be found elsewhere [110].

### 2.2.3 Improving efficiency

In the following, we will introduce several methods that are usually applied to reduce the computational cost of simulations without significantly affecting the results. Most MD simulations will only consider pairwise interactions and neglect any higher-body interactions, because they are computationally very expensive. The average three-body effect can be included in the pair potential as an ‘effective’ pair potential. At this point it is important to note that the force calculations is the most computationally expensive part of MD simulations. Since many potentials are short-range, they can be truncated at a cutoff distance  $r_c$ . The interaction potential between two particles further apart than  $r_c$  is set equal to zero and hence does not have to be evaluated, i.e. the smaller the cutoff, the smaller the number of force calculations. The appropriate size of the cutoff depends on how long-range the potential is. To avoid fluctuations caused by the forces and pressure being discontinuous at the cutoff, potentials are often shifted vertically at the cutoff. The potential  $U_{\text{cut}}$  for a truncated and shifted potential is described by

$$U_{\text{cut}}(r) = \begin{cases} U(r) - U(r_c) & \text{if } r \leq r_c \\ 0 & \text{if } r > r_c. \end{cases} \quad (2.9)$$

The results will differ slightly with the cutoff and shift included, especially if the shift is large. These differences can be minimised by calculating the tail contribution to account for the long-range contributions [108]. The shifted potential is closer to the real potential the larger the chosen cutoff. Hence the choice of the cutoff distance is crucial. If it is too small, the system’s thermodynamic properties will change significantly; if it is too large the force calculations will become very expensive. The effect of different cutoff ranges as well as the shift are demonstrated in Fig. 2.1 for a Lennard-Jones pair potential  $U_{\text{LJ}}$

$$U_{\text{LJ}}(r) = 4\epsilon_0 \left[ \left( \frac{\sigma_0}{r} \right)^{12} - \left( \frac{\sigma_0}{r} \right)^6 \right]. \quad (2.10)$$

Here  $\epsilon_0$  and  $\sigma_0$  can be used as units of energy and length respectively and hence can be set to unity (see Section 2.2.4). Some systems are almost exclusively governed by excluded volume effects, in which case the potential can be truncated at its minimum and shifted upwards to obtain a purely repulsive potential, see Fig. 2.1. In some

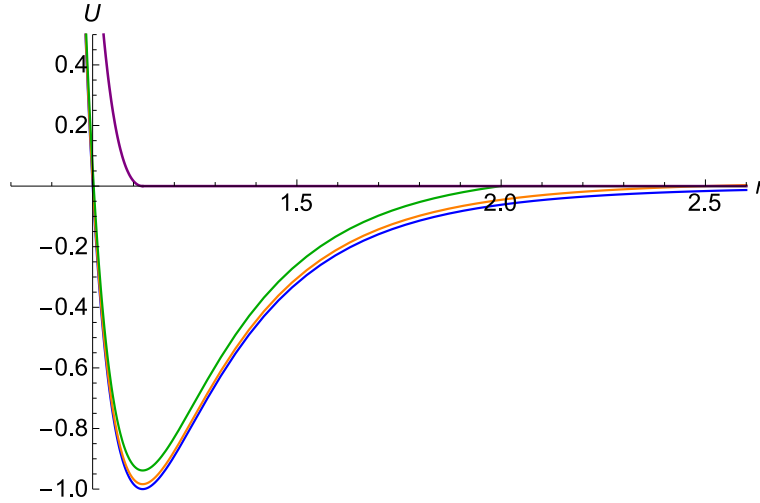


Figure 2.1: Lennard-Jones potential  $U_{\text{LJ}}(r)$  with  $\epsilon_0 = \sigma_0 = 1$ : unshifted (blue), shifted with cutoff  $r_c = 2.5$  (orange), shifted with cutoff  $r_c = 2.0$  (green) and purely repulsive (purple).

systems long-range interactions (e.g. Coulomb charge-charge or dipolar interactions) are important; these have to be treated separately [108, p.291].

In simulations only a very small number of particles can be used compared to the molecular number in real experiments, since pairwise interactions will lead to a  $N^2$  scaling of the force calculations. The problem arises that the smaller the simulation box size, the larger the fraction of molecules lying at the surface, where they are experiencing different forces from the molecules inside the bulk. In order to avoid these edge effects, the presence of an infinite bulk with the same properties as the simulation box is mimicked around the box. This is realised by treating the simulation box as the primitive cell of an infinite lattice; this method is called periodic boundary conditions. The periodic images move in exactly the same way as the molecules in the original box. Thus a molecule that leaves the box will re-enter from the opposite side with the same velocity. Consequently the total number of molecules in the primitive cell is conserved. Only the coordinates and velocities of the molecules in the original box have to be stored, while all images can be reconstructed geometrically. Each particle interacts with all other particles in the simulation box as well as all particle images. A schematic sketch of periodic boundary conditions is shown in Fig. 2.2. Care has to be taken since this approach introduces artificial periodicity into the system. For example, first order transitions often appear of higher order in small simulation boxes due to the suppression of fluctuations. However, periodic boundaries usually have little effect on equilibrium

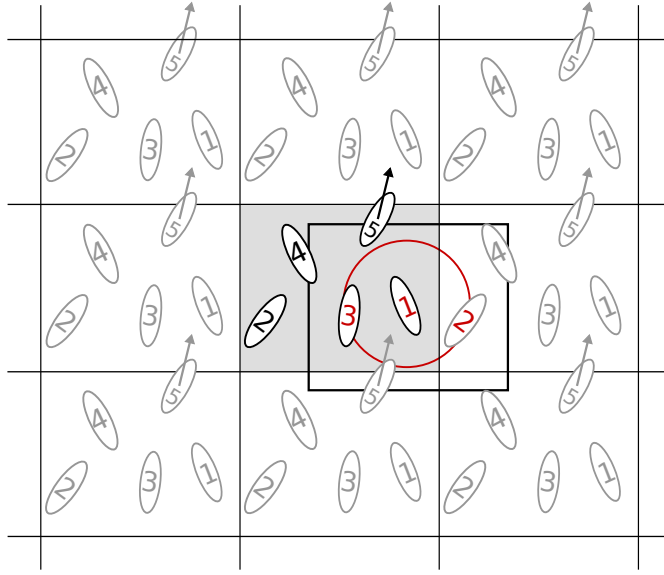


Figure 2.2: Schematic sketch of periodic boundary conditions and minimum image convention: Black particles are inside the original box coloured grey. All grey particles are mirror images of the original particles. Only particles within the red interaction radius of particle 1 interact with it, i.e. particle 3 and the mirror image of particle 2.

thermodynamic properties as long as interactions are short-range.

Using periodic boundaries, particles near the surface interact across the boundary. Here we introduce the minimum image convention, which states that only the nearest image of a particle will contribute, when we calculate the forces. This can be thought of as drawing a box of the same size as the original simulation box size with the molecule of interest at its centre. Only particles that lie within this box contribute to the interaction potential for the considered molecule. It can be seen in Fig. 2.2 that particle 1 interacts with an image of particle 2 rather than the particle itself, because the image is closer to particle 1. Within this limiting box, a spherical cutoff can be used. As before, only molecules that lie within the cutoff radius contribute to the potential. As a consequence of the minimum image convention, the cutoff radius should never be bigger than half the box size  $L/2$ . The impact of the periodicity of the artificially produced lattice on simulations has to be considered carefully[113], see Section 5.3.3. As before, long-range interactions have to be treated more carefully [108].

To calculate the forces, we have to loop over all particles to calculate the minimum image separation, which will leave us with  $N^2$  calculations. However we know that particles very far apart will not interact over the next few time steps.

To increase efficiency we can keep a list for each particle of all nearby particles that could enter their interaction radius over the next few time steps. To build the list, we choose a cutoff radius  $r_{\text{list}}$ , which is larger than  $r_c$ . Molecules that are closer than  $r_{\text{list}}$  to a particle are added to their neighbour list. To calculate forces, we can loop over the listed particles only. This avoids unnecessary calculations of the particles' separation, which leads to significant savings of CPU time. The lists only have to be updated every few time steps. In Fig. 2.3(a) we illustrate neighbour lists in two dimensions. All white and grey particles are listed. White particles are already inside the interaction radius and grey particles could enter the cutoff region over the next few time steps. It is important to ensure that  $r_{\text{list}}$  is sufficiently large and that the list is updated frequently enough. No particle should be able to move across the annulus between two adjacent updates of the neighbouring list. For very large systems, neighbour lists become memory heavy. Instead cell structures can be used to exclude particles that are far apart from the force calculation. By dividing the simulation box into small cells that are bigger than the cutoff radius, we can store an index for each particle depending on the cell they are in. For force calculation we only have to check particles within the surrounding cells. Checking an index is faster than calculating the distance between two particles. A schematic sketch of cell lists is shown in Fig. 2.3(b). Additional methods, e.g. linked lists or multiple time step, can be used and are described elsewhere [113].

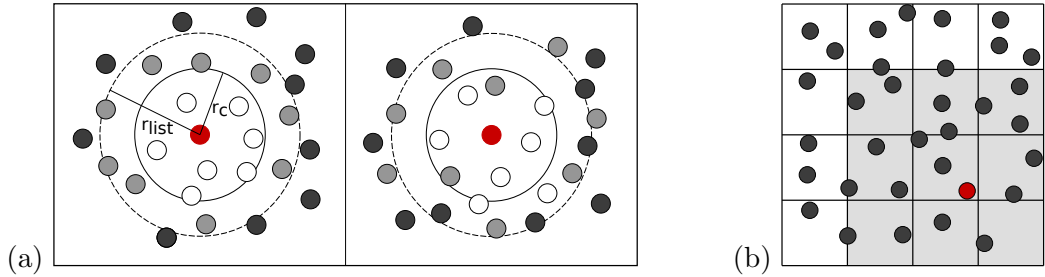


Figure 2.3: (a) Schematic sketch of neighbour lists. All white particles are within the cutoff radius  $r_c$  of the particle of interest (red). All grey particles are listed on the neighbour list, because they are likely to enter the cutoff radius over the next few time steps. Black particles are not listed and should not enter the cutoff radius. If they do, the list is not updated frequently enough. (b) Schematic sketch of cell list in 2D. Box is divided into 16 cells. For each particle we store the cell index. For the particle of interest (red), only particles within the surrounding (grey) cells are checked for force contributions.

Simulations can take a very long time, or even too long, if very large system sizes are needed. To speed up simulations many computing nodes can be used rather

than a single one. A very effective way to divide the work amongst the processors is to use domain decomposition. The simulation box is subdivided into regions and each processor only updates positions and momenta for particles inside its assigned region. Nodes have to share information about particles near the boundaries. Commonly the information is shared using MPI. In theory, there is no limit to how many processors are used. However in simulations the computer time spent on the inter-node communication increases significantly for very large numbers of processors. The optimum number of processors depends on the precise system studied.

#### 2.2.4 Reduced units

In molecular simulations reduced units are commonly used instead of SI units. For example for the Lennard-Jones like potential, we can scale the energy by the factor  $\epsilon_0$  and the distance units by  $\sigma_0$ . Without loss of generality we can choose these units and the mass  $m$  to be unity. All quantities can be expressed in terms of these basic units [113], e.g. the basic unit of time is  $\tau_0 = \sigma_0 \sqrt{m/\epsilon_0}$ . The results of a simulation can always be converted back into SI units. This implies that many systems can be described by just one simulation. The main advantage of reduced units is that most numbers will vary in the range of  $10^{-3}$  to  $10^3$  and therefore the error introduced by floating point calculations is minimised and sometimes mistakes can be discovered when the results of the simulation are far outside this range. All units in this thesis are given in reduced units.

### 2.3 Equilibration of the Gay-Berne nematic LC phase

The potential originally suggested by Gay and Berne [72] is widely used to simulate liquid crystals. It is a coarse-grained single-site potential that represents the interaction energies between two elongated or disk-shaped molecules. It can be regarded as a shifted, anisotropic Lennard-Jones potential, i.e. it depends on the relative orientation of the particles as well as their separation. For identical uniaxial particles it can be written as [117, 118]

$$U(\hat{\mathbf{u}}_i, \hat{\mathbf{u}}_j, \mathbf{r}_{ij}) = 4\epsilon(\hat{\mathbf{u}}_i, \hat{\mathbf{u}}_j, \hat{\mathbf{r}}_{ij}) [\varrho(\hat{\mathbf{u}}_i, \hat{\mathbf{u}}_j, \mathbf{r}_{ij})^{-12} - \varrho(\hat{\mathbf{u}}_i, \hat{\mathbf{u}}_j, \mathbf{r}_{ij})^{-6}] , \quad (2.11)$$

where

$$\varrho(\hat{\mathbf{u}}_i, \hat{\mathbf{u}}_j, \mathbf{r}_{ij}) = \frac{r_{ij} - \sigma(\hat{\mathbf{u}}_i, \hat{\mathbf{u}}_j, \hat{\mathbf{r}}_{ij}) + \sigma_0}{\sigma_0} . \quad (2.12)$$

$\hat{\mathbf{u}}_i$  and  $\hat{\mathbf{u}}_j$  are unit vectors along the principal axes of the two particles  $i$  and  $j$ , while  $\mathbf{r}_{ij} = \mathbf{r}_i - \mathbf{r}_j$  is the vector connecting their centres of mass,  $r_{ij} = |\mathbf{r}_{ij}|$ , and



$\hat{\mathbf{r}}_{ij} = \mathbf{r}_{ij}/r_{ij}$ .  $\sigma_0$  is a parameter representing the width of the particle.  $\sigma(\hat{\mathbf{u}}_i, \hat{\mathbf{u}}_j, \hat{\mathbf{r}}_{ij})$  is the orientation-dependent range parameter

$$\sigma(\hat{\mathbf{u}}_i, \hat{\mathbf{u}}_j, \hat{\mathbf{r}}_{ij}) = \sigma_0 \left[ 1 - \frac{\chi}{2} \left( \frac{(\hat{\mathbf{r}}_{ij} \cdot \hat{\mathbf{u}}_i + \hat{\mathbf{r}}_{ij} \cdot \hat{\mathbf{u}}_j)^2}{1 + \chi \hat{\mathbf{u}}_i \cdot \hat{\mathbf{u}}_j} + \frac{(\hat{\mathbf{r}}_{ij} \cdot \hat{\mathbf{u}}_i - \hat{\mathbf{r}}_{ij} \cdot \hat{\mathbf{u}}_j)^2}{1 - \chi \hat{\mathbf{u}}_i \cdot \hat{\mathbf{u}}_j} \right) \right]^{-1/2}. \quad (2.13)$$

Here  $\chi$  is given by

$$\chi = \frac{\kappa^2 - 1}{\kappa^2 + 1}, \quad (2.14)$$

where  $\kappa$  is the length-to-width ratio of the particle. The strength anisotropy function  $\epsilon(\hat{\mathbf{u}}_i, \hat{\mathbf{u}}_j, \hat{\mathbf{r}}_{ij})$  used in Equation (2.11) is given by

$$\epsilon(\hat{\mathbf{u}}_i, \hat{\mathbf{u}}_j, \hat{\mathbf{r}}_{ij}) = \epsilon_0 \epsilon_1^\nu(\hat{\mathbf{u}}_i, \hat{\mathbf{u}}_j) \epsilon_2^\mu(\hat{\mathbf{u}}_i, \hat{\mathbf{u}}_j, \hat{\mathbf{r}}_{ij}). \quad (2.15)$$

$\epsilon_0$  is the well depth parameter determining the overall strength of the potential, while  $\nu$  and  $\mu$  are two adjustable exponents which allow considerable flexibility in defining a family of Gay-Berne potentials.  $\epsilon_1$  and  $\epsilon_2$  are given by

$$\epsilon_1(\hat{\mathbf{u}}_i, \hat{\mathbf{u}}_j) = \left[ 1 - \chi^2 (\hat{\mathbf{u}}_i \cdot \hat{\mathbf{u}}_j)^2 \right]^{-1/2}, \quad (2.16)$$

$$\epsilon_2(\hat{\mathbf{u}}_i, \hat{\mathbf{u}}_j, \hat{\mathbf{r}}_{ij}) = 1 - \frac{\chi'}{2} \left[ \frac{(\hat{\mathbf{r}}_{ij} \cdot \hat{\mathbf{u}}_i + \hat{\mathbf{r}}_{ij} \cdot \hat{\mathbf{u}}_j)^2}{1 + \chi' \hat{\mathbf{u}}_i \cdot \hat{\mathbf{u}}_j} + \frac{(\hat{\mathbf{r}}_{ij} \cdot \hat{\mathbf{u}}_i - \hat{\mathbf{r}}_{ij} \cdot \hat{\mathbf{u}}_j)^2}{1 - \chi' \hat{\mathbf{u}}_i \cdot \hat{\mathbf{u}}_j} \right]. \quad (2.17)$$

Here

$$\chi' = \frac{\kappa'^{1/\mu} - 1}{\kappa'^{1/\mu} + 1}, \quad (2.18)$$

where  $\kappa' = \epsilon_S/\epsilon_E$  is the ratio of well depths for the side-to-side configuration,  $\epsilon_S$ , and the end-to-end configuration,  $\epsilon_E$ , of two molecules. Different versions of the potential are identified by the  $\text{GB}(\kappa, \kappa', \mu, \nu)$  notation of Bates and Luckhurst [119].  $\text{GB}(3, 5, 2, 1)$  was the original suggestion of Gay and Berne [72], for which the phase diagram has been well studied [11, 120, 121], and  $\text{GB}(3, 5, 1, 3)$ , was later proposed by Berardi et al. [117], which has the advantage of a wider nematic range. The Gay-Berne potential has also been used to study discotic systems [122]. In Fig. 2.4 the Gay-Berne potential is plotted over particle separation for different particle orientations, namely side-by-side, side-to-end (in a T-shape), side-cross-side (in an X-arrangement, with the centre-centre vector perpendicular to both molecular axes) and end-to-end. The ratio of the well depths for side-to-side and end-to-end  $\kappa' = \epsilon_S/\epsilon_E$  was chosen to be 5. The length of the molecules was set to  $\ell = 3$  and the

width to  $d = 1$ , i.e.  $\kappa = \ell/d = 3$ .  $\sigma_0$  and  $\epsilon_0$  were set to unity. When comparing the GB(3, 5, 2, 1) and GB(3, 5, 1, 3) in Fig. 2.4 it can be seen that for the latter parameter set the well depth for side-by-side is significantly lower, which enhances the nematic range.

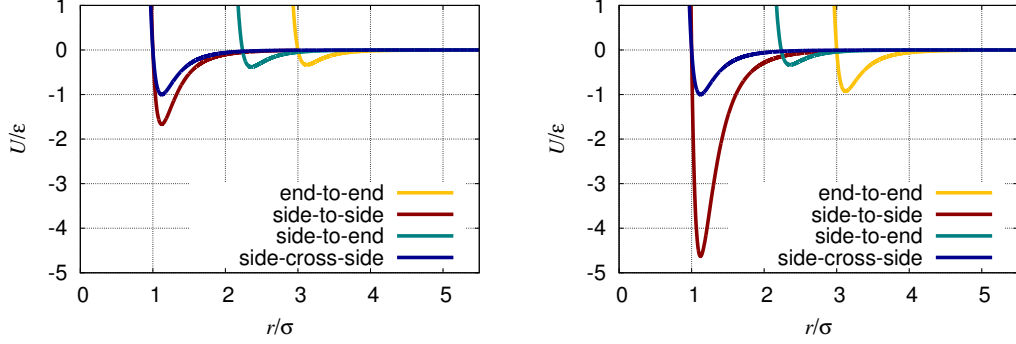


Figure 2.4: Standard Gay-Berne potential scaled by  $\epsilon_0$  plotted over particle separation scaled by  $\sigma_0$  for different orientations: side-to-side, side-cross-side, end-to-side and end-to-end for  $\kappa=3$  and  $\kappa'=5$  (a)  $\mu=2$  and  $\nu=1$  (b)  $\mu=1$  and  $\nu=3$ .

Another variation of the Gay-Berne potential is the purely repulsive GB potential, which corresponds to a truncated and vertically shifted standard GB potential. It can be thought of as the standard GB potential with  $\mu = \nu = 0$ . This potential variation has two main advantages: the force calculation itself is computationally cheaper and it allows the use of a shorter potential cutoff (see Chapter 2.2.3), which leads to a significant speed-up of simulation runs. The purely repulsive Gay-Berne potential can be written as

$$U(\hat{\mathbf{u}}_i, \hat{\mathbf{u}}_j, \mathbf{r}_{ij}) = \begin{cases} 4\epsilon_0 [\varrho(\hat{\mathbf{u}}_i, \hat{\mathbf{u}}_j, \mathbf{r}_{ij})^{-12} - \varrho(\hat{\mathbf{u}}_i, \hat{\mathbf{u}}_j, \mathbf{r}_{ij})^{-6}] + \epsilon_0, & \text{if } \varrho^6 \leq 2 \\ 0, & \text{else.} \end{cases} \quad (2.19)$$

Note that  $\epsilon_0$  is independent of the orientation in contrast to  $\epsilon$  in Equation (2.11).  $\varrho$ ,  $\sigma$  and  $\chi$  are unchanged (see Equations (2.12), (2.13) and (2.14)). In Fig. 2.5 the purely repulsive Gay-Berne potential is plotted over particle separation for different particle orientations for particles with elongation  $\kappa = 3$  and  $\kappa = 5$ . We refer to these systems as GB(3, 0, 0) and GB(5, 0, 0). One can see that the potential behaves very similarly for different orientations; solely  $\sigma$  varies depending on the orientations. Note that the potential for the side-by-side orientation is identical to the one for the side-cross-side orientation. Because there are no attractive forces in this system, the phase behaviour is not sensitively dependent on the temperature  $T$ .

Nematic Gay-Berne liquid crystals are equilibrated using the molecular dy-

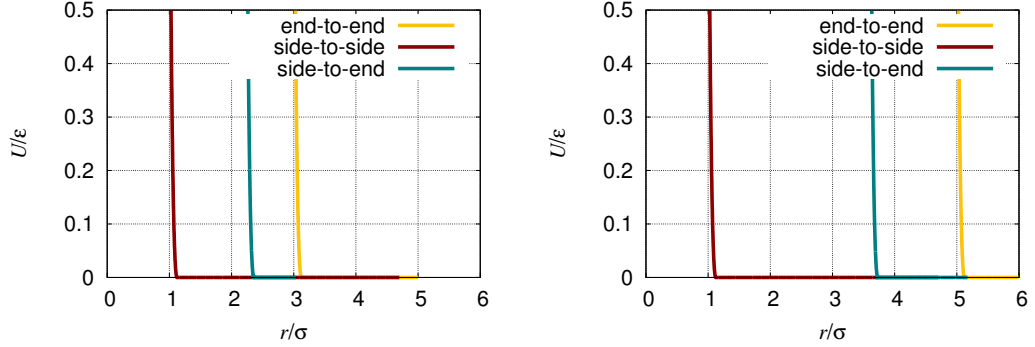


Figure 2.5: Purely repulsive Gay-Berne potential scaled by  $\epsilon_0$  plotted over particle separation scaled by  $\sigma_0$  for different orientations: side-to-side, end-to-side and end-to-end for (a)  $\kappa=3$  and (b)  $\kappa=5$ .

namics packages LAMMPS [123] and GBMOLDD [124]. Both these molecular dynamics packages can be run in parallel using domain decomposition and parallel message passing. To simulate one million Gay-Berne molecules, one can use up to 96 processors to speed up the simulation significantly which allows the study of very large systems within a reasonable time frame. For higher numbers of processors the inter-processor communication increases drastically and hence efficiency is decreasing. GBMOLDD does not scale quite as well as LAMMPS, but it has the advantage to be focused on aspherical particles. Hence, it is straightforward to add orientation dependent external potentials and the corresponding forces and torques. In chapter 3, 4 and 6 LAMMPS was used due to its excellent scaling. In chapter 5, 7 and 8 GBMOLDD was used, which allowed straight-forward implementation of the external potentials required. Some simulations in LAMMPS were repeated in GBMOLDD and no differences were detected. GBMOLDD uses the Gay-Berne potential in its original form [72], whereas LAMMPS uses a generalised form of the Gay-Berne potential, also suitable for biaxial ellipsoids, due to Berardi et al. [125] and reformulated by Everaers and Ejtehadi [126]. Note that GBMOLDD automatically shifts the potential to remove the discontinuity at the (spherical) potential cutoff (See Section 2.2.3 for definition of potential cutoff.); In contrast LAMMPS does not shift the potential. Throughout this work we solely use a potential cutoff of  $5.0\sigma_0$  for the standard Gay-Berne potential, which is slightly larger than the commonly used  $4.0\sigma_0$ . The larger cutoff ( $5.0\sigma_0$ ) keeps truncation errors minimal. At the cutoff distance the potential energy for end-to-end interactions is small with  $0.005\epsilon_0$  and it is even less for all other pairs of orientations. For much smaller cutoffs than  $5.0\sigma_0$ , the choice of cutoff influences the results (e.g. bulk order parameter) significantly and the choice between a shifted or unshifted potential becomes important. For the repulsive Gay-

Berne potential a cutoff of  $(\kappa + 1)\sigma_0$  was found to be a suitable choice.

One method to quickly equilibrate a nematic monodomain is to prepare simulations by filling a cuboidal simulation box with the desired number of particles at the specific density. The initial elongation is set at  $\kappa = 1$  (spherical particles), the positions are chosen to lie on a simple cuboidal lattice, and the initial orientation vectors are all aligned along the axis of choice. Keeping the volume of the box fixed, the MD simulation is initiated, and the particles are progressively elongated along their axis of orientation, until they reached their desired ellipsoidal shape (e.g.  $\kappa = 3$ ). During the growth the particles are free to rotate and translate: positional order is monitored and shown to disappear quite quickly, whereas it proves possible to elongate the particles sufficiently rapidly to reach a nematic monodomain, with the director closely aligned along the initially chosen direction, without the system ever becoming orientationally disordered. This initial growth is followed by an equilibration run, which has to be sufficiently long, because the orientational order takes a long time to equilibrate, especially when the system is large. A detailed study of the relaxation dynamics of the Gay-Berne nematic LC is presented in Chapter 4. In the work presented here, we focus solely on the nematic phase, hence positional order is negligible i.e. very short-range.

## 2.4 Visualisation

In the analysis of nematic textures, especially in regions near the defects, data visualisation of the nematic field plays an important role. In this section we will give a short account of the different methods available, followed by a detailed description of three methods used throughout this thesis.

Traditionally, the director orientation is used to visualise the nematic field. Here the director  $\hat{\mathbf{n}}$  can be represented by, for example, ‘nails’ or cylindrical glyphs to visualise a two-dimensional cross-section. An alternative is to utilise the entire order tensor. Each local order tensor  $\mathbf{Q}$  can be represented by an ellipsoid with its axes along the eigenvectors, and each axis being scaled by the corresponding eigenvalue. However both these methods are somewhat limited to two dimensions. To locate and visualise defects in 3D isosurfaces of lower nematic order  $S$  are commonly used [105, 127, 128]. Since  $S$  does not vary much within the bulk, but decreases significantly around the defect, this approach is sufficient to reliably locate defects. It has the advantages of giving a ‘clean’ picture even in 3D by avoiding unnecessary information. If the biaxiality of the nematic field is of interest, it can be superimposed on the isosurface by the use of colour variations. In addition to these commonly used

methods, more complex ones include the use of streamlines [129], Pontryagin-Thom surfaces, which are based on points which share a common director orientation [130], and splay-bend order parameter visualisation [131].

In molecular dynamics simulations it can be of interest to visualise an instantaneous snapshot of the system. Since each molecular position and orientation is known, we can visualise the molecules as uniaxial ellipsoids. We used the open source software QMGA [132], which has a useful feature of colour coding the molecules depending on their orientation. Molecules, which are parallel to the director are blue; Molecules, which are perpendicular to the director are red and intermediate orientations are coloured green. (Not that we will use a different colour scheme in Chapter 7 and Chapter 8.) Three snapshots of a slice through a smectic, nematic and isotropic Gay-Berne system are shown in Fig. 2.6. Note the absence of positional order in the

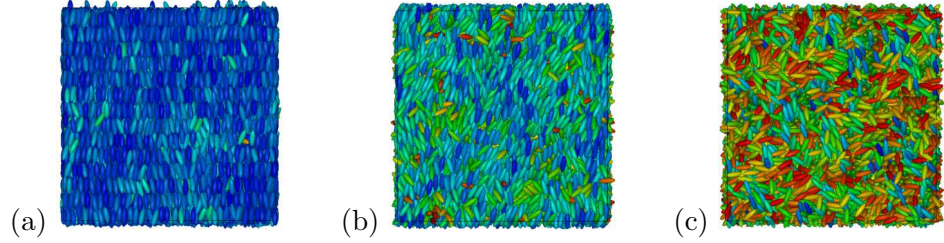


Figure 2.6: QMGA snapshots of slices through the Gay-Berne system  $\mu = 1$ ,  $\nu = 3$  at density  $\rho = 0.3$ : (a) smectic ( $T = 2.0$ ), (b) nematic ( $T = 3.4$ ) and (c) isotropic phase ( $T = 4.0$ ). Molecular orientation is colour coded with respect to the director. Blue molecules are parallel to the director, whereas red molecules are perpendicular to it.

nematic and isotropic phase and the absence of orientational order in the isotropic phase.

A commonly used approach to visualise defects in liquid crystals is to divide the simulation box into small cubic bins. For each bin the local order tensor  $\mathbf{Q}$  is calculated. For a better resolution, i.e. smaller bins, we need to time average over a longer time to ‘fill’ the bins. Ideally the bin size should be comparable to the defect core size. For each bin we have full information of the local order tensor as well as the density. Hence we can plot two-dimensional cross sections of these quantities in the regions of interest. In the binning approach, line defects are tracked by analysing planes parallel to the faces of the bins. Within one of these planes, the director  $\mathbf{n}$  is tracked around a square on the order parameter space sphere. If the final director is on the different hemisphere a disclination line is cutting through the square. The disclination line is perpendicular to the plane of the square [133, 134]. However,

there are many limitations inherent in this approach. Defect loops calculated this way consist of straight lines joined by  $90^\circ$  angles, which is not smooth and does not represent the nature of defects very well. For a high resolution, it is necessary to time-average the data to fill each bin with a sufficient amount of molecules. However this prevents us from seeing any short time-scale dynamics of the system.

Our main research focus here is to study the defects in liquid crystals. Since we are particularly interested in the dynamics of these systems, we require a method to visualise defects for instantaneous system snapshots. Callan-Jones et al. [135] suggested an approach, which enables one to visualise defects for a single snapshot by creating a quasi-continuous tensor field. Their method allows to locate disclination lines and it also gives information about the defect core and the director field around the core region. This visualisation process can be described in the following steps. First, the order tensor  $\mathbf{Q}$  is modified, so that all its eigenvalues are non-negative by adding the identity matrix  $\mathbf{I}$ . As mentioned earlier, this new diagonalised tensor  $\mathbf{D}^{\text{diag}}$

$$\mathbf{D}^{\text{diag}} = \mathbf{Q}^{\text{diag}} + \frac{1}{3}\mathbf{I} = \begin{pmatrix} \lambda_1 & 0 & 0 \\ 0 & \lambda_2 & 0 \\ 0 & 0 & \lambda_3 \end{pmatrix} \quad (2.20)$$

can be represented by a spheroid with the eigenvectors along the principal axes and the corresponding eigenvalues being their respective length [136]. The eigenvalues of  $\mathbf{D}^{\text{diag}}$  are labelled  $\lambda_1 \geq \lambda_2 \geq \lambda_3$  with  $\lambda_1 + \lambda_2 + \lambda_3 = 1$ . The main limitation is that  $\mathbf{D}^{\text{diag}}$  is only defined by averaging over a region of space containing non-vanishing number of molecules. A weighting function  $w$  that interpolates  $\mathbf{D}^{\text{diag}}$  within a certain volume is introduced to create a quasi-continuous tensor field

$$D_{\alpha\beta}(\mathbf{r}) = \frac{1}{N(V_s)} \sum_{i \in V_s} w(|\mathbf{r}_i - \mathbf{r}|) u_m^i u_{m'}^i. \quad (2.21)$$

Here  $N(V_s)$  is the number of molecules in the sampling volume  $V_s$ .  $\mathbf{r}_i$  is the position vector of particle  $i$  and  $u^i$  is the component of the orientation vector with  $mm' = x, y, z$ .  $w(|\mathbf{r}_i - \mathbf{r}|)$  is a weighting function with the constraint

$$\sum_{i \in V_s} w(|\mathbf{r}_i - \mathbf{r}|) = 1. \quad (2.22)$$

For the weighting we choose a cubic b-spline, see Fig. 2.7, which is a piecewise

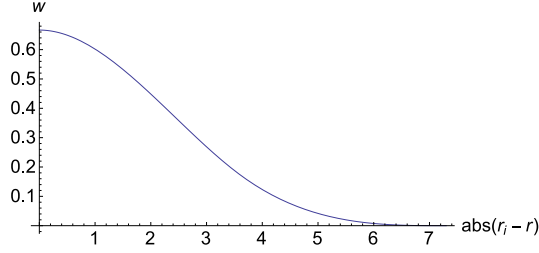


Figure 2.7: Cubic b-spline weighting function  $w$  with kernel radius  $r_k = 7.3$

continuous cubic polynomial approximation to a Gaussian function [137]

$$w(x) = \begin{cases} \frac{1}{6}(3|x|^3 - 6x^2 + 4) & 0 \leq |x| \leq 1 \\ \frac{1}{6}(2 - |x|)^3 & 1 \leq |x| \leq 2 \\ 0 & \text{else,} \end{cases} \quad (2.23)$$

where  $x = 2|\mathbf{r}_i - \mathbf{r}|/r_k$ .  $w$  is zero if  $|\mathbf{r}_i - \mathbf{r}|$  is greater than the kernel radius  $r_k$ .  $r_k$  was chosen to be 7.3, which corresponds to having roughly 30 molecules inside the sampling volume  $V_s$ . From the eigenvalues  $\lambda$ , the Westin metrics can be calculated using

$$c_l = \lambda_1 - \lambda_2, \quad c_p = 2(\lambda_2 - \lambda_3), \quad c_s = 3\lambda_3. \quad (2.24)$$

The Westin metrics have the properties

$$0 \leq c_l, c_p, c_s \leq 1, \quad c_l + c_p + c_s = 1. \quad (2.25)$$

Regions of well ordered uniaxial nematic correspond to  $c_l \sim 1$ , planar ordering corresponds to  $c_p \sim 1$  and isotropic regions correspond to  $c_s \sim 1$  [138]. Within the defect core region  $c_l$  falls below a certain threshold. The choice of this threshold may seem somewhat arbitrary, however by starting at zero and gradually increasing  $c_l$  we reach a point where all defect lines merge, i.e. we have no ‘loose’ ends. The width of the defect core is roughly the same everywhere, which is an indicator that the defect region was determined correctly. The main advantages of this visualisation approach are that time averaging is unnecessary and that there is no limit to the resolution. We simply have to calculate more weighted order tensors if we choose a smaller grid. The software PARAVIEW [139] was used for the visualisation of the isosurface corresponding to low nematic order with  $c_l < \text{threshold}$ .

## 2.5 Conclusions

In the research presented in the following chapters we employed molecular simulations to model nematic liquid crystals to study their elastic and dynamical properties and to investigate topological defects. The positions and orientations of the liquid crystal molecules were updated using molecular dynamics for aspherical particles as introduced in this chapter. Different variations of the soft Gay-Berne interaction potential were employed. The simulations contained up to 1 million particles, which is significantly larger than in previous studies. For such large systems the workload was divided amongst  $\sim 100$  processors. Appropriate potential cutoffs were identified and neighbour lists and periodic boundaries were employed to reduce computational time and costs. We introduced various methods to visualise defects in liquid crystals, which will be used in the following chapters.



## Chapter 3

# Elastic constants in nematic liquid crystals

### 3.1 Introduction

In a liquid crystal, the deviations of the molecular orientations from the director  $\hat{\mathbf{n}}$  are caused by thermal fluctuations. These deformations lead to an energy penalty, and hence elastic forces exist that tend to restore the undistorted state. Assuming these deformations to vary slowly in space relative to the molecular distance scale, the free energy response  $\Delta\mathcal{F}$  of the liquid crystal can be described using continuum elastic theory [12, 140, 141]

$$\Delta\mathcal{F} = \frac{1}{2} \int d\mathbf{r} K_1 (\nabla \cdot \hat{\mathbf{n}}(\mathbf{r}))^2 + K_2 (\hat{\mathbf{n}}(\mathbf{r}) \cdot \nabla \wedge \hat{\mathbf{n}}(\mathbf{r}))^2 + K_3 \left| \hat{\mathbf{n}}(\mathbf{r}) \wedge (\nabla \wedge \hat{\mathbf{n}}(\mathbf{r})) \right|^2, \quad (3.1)$$

where  $K_1$ ,  $K_2$ ,  $K_3$  are the splay, twist and bend Frank elastic constants respectively. Note that the elastic constants have to be positive for the free energy to increase when the nematic is distorted. In addition, a fourth ‘surface-like’ elastic constant term exists, accounting for saddle-splay deformations. However this term can be omitted when studying liquid crystals in the bulk [142].

The elastic properties play a crucial role, for example, in liquid crystal displays [143], colloidal self-assembly [37, 46, 144] and the morphology of nematic droplets [91, 92, 145]. Hence it is important to know the values of the elastic constants, and their relation to molecular structure, since on a mesoscopic length scale they almost exclusively determine the structural properties of the liquid crystal, and together with the transport coefficients of nematodynamics [15–17, 20, 146], govern the dynamical properties as well.

Because in molecular simulations the positions of the molecules and their orientations are known at all times, which allows accurate calculations of properties such as the elastic constants. In contrast to experimental measurements, in simulations it is more straightforward to distinguish between the different deformation modes. On the downside, the elastic constants can only be measured in sufficiently large simulation boxes, since Equation (3.1) is only valid for slowly varying  $\hat{\mathbf{n}}(\mathbf{r})$ , i.e. for fluctuations of long wavelength  $\lambda$ . Moreover, the relaxation times  $\tau$  for these fluctuations are expected to grow rapidly,  $\tau \propto \lambda^2 \propto k^{-2}$ , as the wave number  $k = 2\pi/\lambda$  decreases.

The earliest simulations of this kind, for hard-particle models, used rather small system sizes [147, 148] of a few hundred molecules. Subsequent studies [80] of the Gay-Berne model employed systems of size 1024 – 8000. Recently, hard spherocylinders have been re-examined [149] using system sizes of order 18000, highlighting the care that needs to be taken in the fitting process, and the systematic errors that may result from small system size. Other approaches to calculate the elastic constants have been reported. Cleaver and Allen [150], as well as Gruhn and Hess [151], used the Freédricksz transition to study elastic constants in the Lebwohl-Lasher lattice model; however this approach is approximate, involving a heterogeneous system with boundaries, and the fluctuation approach described here gives more accurate results [150]. Joshi *et al.* [152] used direct calculations of the free energy of perturbations of the uniform director field. As shown by Poniewierski and Stecki [153] (see also [154, 155]), if the orientation-dependent direct correlation function in the nematic can be calculated, the elastic constants may be obtained by appropriate spatial integrations. Early attempts to calculate the elastic constants in this way involved simplifying assumptions of orientational isotropy [79, 156]; the exact calculation, avoiding these assumptions, has been accomplished [78] but is a numerical *tour de force*.

In this chapter we present the elastic constant calculations for a Gay-Berne nematic liquid crystal for two different parameterisations of the interaction potential, and a total of six different state points with a particle length to width ratio of 3:1. The system size chosen is almost two orders of magnitude larger than previous studies, which allows us to pay attention to finite size effects. In addition, we present the elastic constant calculations for a purely repulsive Gay-Berne potential, for two different state points for an intermediate system size with a particle length to width ratio of 5:1.

In Section 1.4 we present the theory of calculating the elastic constants from the orientational fluctuations as a function of wave vector. Details of the simulation

model used, and other simulation details, are given in Section 3.3. Simulation results are presented in Section 3.4 and conclusions are drawn in Section 3.5.

## 3.2 Theoretical background

In the following we briefly recap how the elastic constants are calculated from the equilibrium orientational fluctuations as a function of wave-vector  $\mathbf{k}$  [80, 147, 148]. In a nematic phase we define an order tensor  $\mathbf{Q}$  in reciprocal space (the Fourier transform of the order tensor density) as

$$\tilde{Q}_{mm'}(\mathbf{k}) = \frac{V}{N} \sum_{i=1}^N \left( \frac{3}{2} \hat{u}_{im} \hat{u}_{im'} - \frac{1}{2} \delta_{mm'} \right) \exp(i\mathbf{k} \cdot \mathbf{r}_i). \quad (3.2)$$

Here  $\delta_{mm'}$  is the Kronecker delta, we define Cartesian components  $m, m' = x, y, z$ ,  $N$  is the number of molecules,  $V$  is the volume and  $\hat{\mathbf{u}}_i$  and  $\mathbf{r}_i$  are the orientation vector and the molecular position vector of each molecule  $i$  respectively and  $\mathbf{k}$  is the wave vector. (We restrict our interest to uniaxial molecules). Since the director does not necessarily lie along one of the simulation box axes defining the  $x, y, z$  coordinates, we define a new orthonormal Cartesian axis system  $(\hat{\mathbf{e}}_1, \hat{\mathbf{e}}_2, \hat{\mathbf{e}}_3)$ , where  $\hat{\mathbf{e}}_3$  is along the director. In this system  $\hat{\mathbf{n}} = (0, 0, 1)$ ; small fluctuations of the director may be expressed  $(n_1, n_2, 0)$  and these are proportional to the elements  $Q_{13}$  and  $Q_{23}$ . For simplicity the axes are chosen such that the wave vectors lie in the  $\hat{\mathbf{e}}_1$ - $\hat{\mathbf{e}}_3$  plane, i.e.  $\mathbf{k} = (k_1, 0, k_3)$ . We derived in section 1.4 that the elastic constants can be extrapolated from the Fourier-transformed order tensor fluctuations

$$\langle |\tilde{Q}_{mm'}(\mathbf{k})|^2 \rangle = \langle \tilde{Q}_{mm'}(\mathbf{k}) \tilde{Q}_{mm'}(-\mathbf{k}) \rangle,$$

where the angle brackets represent an ensemble average. These have the long-wavelength behaviour

$$W_{13}(k_1^2, k_3^2) \equiv \frac{\frac{9}{4} \langle S \rangle^2 V k_B T}{\langle |\tilde{Q}_{13}(\mathbf{k})|^2 \rangle} \rightarrow K_1 k_1^2 + K_3 k_3^3 \quad \text{as } k \rightarrow 0, \quad (3.3a)$$

$$W_{23}(k_1^2, k_3^2) \equiv \frac{\frac{9}{4} \langle S \rangle^2 V k_B T}{\langle |\tilde{Q}_{23}(\mathbf{k})|^2 \rangle} \rightarrow K_2 k_1^2 + K_3 k_3^3 \quad \text{as } k \rightarrow 0, \quad (3.3b)$$

where  $k_B$  is the Boltzmann constant and  $T$  the temperature of the system. These quantities can be calculated in the simulation and to extract the elastic constants we have to fit Equation (3.3) for various  $k_1^2$  and  $k_3^2$  and extrapolate to  $k_1 = k_3 = 0$ .

### 3.3 Model and simulation details

For these simulations we used the Gay-Berne interaction potential for uniaxial particles introduced in Section 2.3. We have simulated GB(3,5,2,1) as well as GB(3,5,1,3). and a purely repulsive GB system to which we will refer as GB(5,0,0). The particles with  $\kappa = 3$  were treated as linear rotors, with a moment of inertia chosen to correspond to a uniform distribution of mass within the ellipsoidal shape:  $I = \frac{1}{20}m_0\sigma_0^2(1+\kappa^2)$ . For the longer particles with  $\kappa = 5$ , we chose a higher moment of inertia of  $I = 7.0$ .

For the GB(3,5,2,1) and GB(3,5,1,3) system each simulation was prepared by filling a cubic simulation box with  $N = 512\,000$  particles at the specific density. The system was equilibrated following the procedure described in Section 2.3. Positional order was monitored and found to disappear quite quickly and the rapid particle elongation allows for the equilibration of a nematic monodomain. This initial growth and short equilibration was followed by a longer equilibration run of  $4 \times 10^5$  steps using a timestep of  $\Delta t = 0.004\tau_0$ . We will show in the following chapter (Chapter 4) that this period was sufficient by determining the time correlation functions as a function of wave vector. Simulations were carried out in both the canonical, constant- $NVT$ , ensemble, using the Nosé-Hoover thermostat, and in the microcanonical, constant- $NVE$ , ensemble. The  $NVT$  production runs were of length  $1.9 \times 10^6$  timesteps,  $\Delta t = 0.004\tau_0$ . All molecular positions and orientations were stored every 500 steps for later analysis. The standard deviations of the total energy and the temperature over the entire length of the production run are as small as 1% and 0.3% respectively. Simulation details including the temperature, density, and average order parameter, are given in Table 3.1. We also report the standard deviation  $\sqrt{\langle\delta\theta^2\rangle}$  of the angle  $\delta\theta = \cos^{-1}(|\hat{\mathbf{n}} \cdot \hat{\mathbf{n}}_0|)$  between the initial director  $\hat{\mathbf{n}}_0$  and the instantaneous director  $\hat{\mathbf{n}}$ . This quantity will increase with run length, as the director undergoes rotational diffusion; the results simply indicate that, for these system sizes, this motion is extremely slow on the timescale of our simulations, amounting to no more than a few degrees over the full run in the worst case. For this reason, constraints on the director motion [80] were considered unnecessary. All runs were repeated with a much smaller system size of 8000 GB molecules to investigate finite size effects.

The data obtained from these  $NVT$  runs was used to calculate the elastic constants. For the GB(3,5,1,3) state point  $\rho\sigma_0^3 = 0.3$ ,  $k_B T/\epsilon_0 = 3.4$ , we repeated the runs with a smaller timestep  $\Delta t = 0.002\tau_0$ , simulating in the microcanonical  $NVE$  ensemble to confirm that the thermostating does not affect the results obtained.

The total run length in this case was  $10^6$  timesteps with snapshots stored every 500 time steps. Indeed we find that the elastic constants only deviate by a few percent from the ones calculated using the longer *NVT* runs.

The GB(5,0,0) system was prepared in the same fashion as the standard Gay-Berne ones. The number of Gay-Berne particles was  $N = 125\,000$ . For these runs the constant-*NVE* ensemble was used. The equilibration run length was 400 000, followed by a production run of 1 000 000 timesteps with a timestep  $\Delta t = 0.002$ . A system snapshot was stored every 500 timesteps. Simulation details for this system are given in Table 3.1.

Table 3.1: System details and elastic constants for eight different state points for GB(3,5,2,1), GB(3,5,1,3) and GB(5,0,0) model. We tabulate density  $\rho \equiv \rho\sigma_0^3$ , temperature  $T \equiv k_B T/\epsilon_0$ , average order parameter  $\langle S \rangle$  with estimated error in parentheses, and standard deviation  $\sigma_\theta = \sqrt{\langle \delta\theta^2 \rangle}$  of the angle  $\delta\theta = \cos^{-1}(|\hat{\mathbf{n}} \cdot \hat{\mathbf{n}}_0|)$  (in degrees) between the initial director  $\hat{\mathbf{n}}_0$  and the instantaneous director  $\hat{\mathbf{n}}$ , for the constant-*NVT* runs. Elastic constants  $K_1, K_2, K_3$  are obtained from  $W_{13}$  and  $W_{23}$  surface fitting; the coefficients of determination  $R^2$  for each surface fit are given. Error bars, in parentheses, are discussed in the text.

$\rho$	$T$	$\langle S \rangle$	$\sigma_\theta$ (°)	$W_{13}$ fit			$W_{23}$ fit		
				$K_1$	$K_3$	$R^2$	$K_2$	$K_3$	$R^2$
GB(3,5,2,1)									
0.32	0.9	0.576(2)	0.5	0.61(5)	1.48(7)	0.96	0.69(6)	1.60(4)	0.98
0.33	1.0	0.658(1)	0.4	0.91(7)	2.62(7)	0.97	1.01(8)	2.74(5)	0.99
0.35	2.0	0.580(7)	1.2	1.54(6)	4.00(8)	0.99	1.28(4)	3.96(4)	0.99
0.38	3.0	0.643(5)	0.7	3.9(3)	11.6(2)	0.99	3.1(2)	11.2(2)	0.99
GB(3,5,1,3)									
0.3	3.4	0.614(2)	0.7	3.16(6)	5.88(6)	0.99	2.79(6)	5.85(3)	0.99
0.3	3.45	0.577(3)	1.9	2.79(6)	5.04(3)	0.99	2.45(6)	4.97(3)	0.99
GB(5,0,0)									
0.125	1.0	0.577(4)	0.6	0.63(1)	1.43(1)	0.97	0.36(1)	1.40(2)	0.98
0.15	1.0	0.824(2)	0.4	1.64(1)	7.92(6)	0.99	0.98(1)	7.89(4)	0.99

### 3.4 Data analysis and results

All of our results are calculated as functions of wave vector  $\mathbf{k}$ . In cubic periodic boundary conditions, this is restricted to

$$\mathbf{k} = \frac{2\pi}{L}(\kappa_x, \kappa_y, \kappa_z) . \quad (3.4)$$

Here  $\kappa_x, \kappa_y, \kappa_z$  are integers, and the box length  $L \gtrsim 95\sigma_0$ . In our calculations we restricted interest to  $-5 \leq \kappa_x, \kappa_y \leq 5$  and  $0 \leq \kappa_z \leq 5$ , excluding  $\mathbf{k} = (0, 0, 0)$ .

The data analysis for the elastic constant calculations consists of three parts. Firstly the instantaneous order tensor in reciprocal space is calculated from Equation (3.2) for the allowed set of wave vectors given by Equation (3.4). In the second step, the order tensor is converted from the  $(\hat{\mathbf{x}}, \hat{\mathbf{y}}, \hat{\mathbf{z}})$  frame to the  $(\hat{\mathbf{e}}_1, \hat{\mathbf{e}}_2, \hat{\mathbf{e}}_3)$  frame, and hence  $\tilde{Q}_{13}$  and  $\tilde{Q}_{23}$  can be calculated as functions of  $k_1^2$  and  $k_3^2$  for each stored configuration. Thirdly, the quantities  $|\tilde{Q}_{13}|^2$  and  $|\tilde{Q}_{23}|^2$  are averaged over the entire run, and statistical errors on these quantities estimated by a blocking procedure. To ensure that this did not underestimate errors at low  $k$  (when the fluctuation timescales become very long) these error estimates were corrected by fitting them to a simple function of  $k^2$  and extrapolating higher- $k$  results to low  $k$  (see also Ref. [80]). These results are used to compute  $W_{13}(k_1^2, k_3^2)$  and  $W_{23}(k_1^2, k_3^2)$  using Equation (3.3), with associated statistical errors obtained by the standard error propagation formula. The fact that director motion is very small simplifies the analysis since  $W_{mm'}$  can be measured on a fixed grid in  $\mathbf{k}$ -space.

To calculate the elastic constants from Equation (3.3), each  $W_{mm'}$  is fitted to a low-order polynomial passing through the origin

$$p(k_1^2, k_3^2) = p_{10}k_1^2 + p_{01}k_3^2 + p_{11}k_1^2k_3^2 . \quad (3.5)$$

The estimated errors on each data point were used to calculate weights for the fit. The results for the fitted surfaces  $W_{13}$  and  $W_{23}$  are plotted for one of the state points in Figure 3.1.

It can be seen that in this regime of very small wave vectors the data has very little curvature. This was observed for all state points for all GB potential variations, which confirms that our chosen wave vectors were sufficiently small for Equation (3.3) to hold. The clustering of data points around specific values of  $k_3^2$ , apparent in Figure 3.1, is due to the minimal deviation of the director from its initial orientation in the  $z$ -direction. The goodness of fit is very high, with the coefficient of determination  $R^2 \geq 0.99$  for almost all cases. To highlight the quality of the fit,

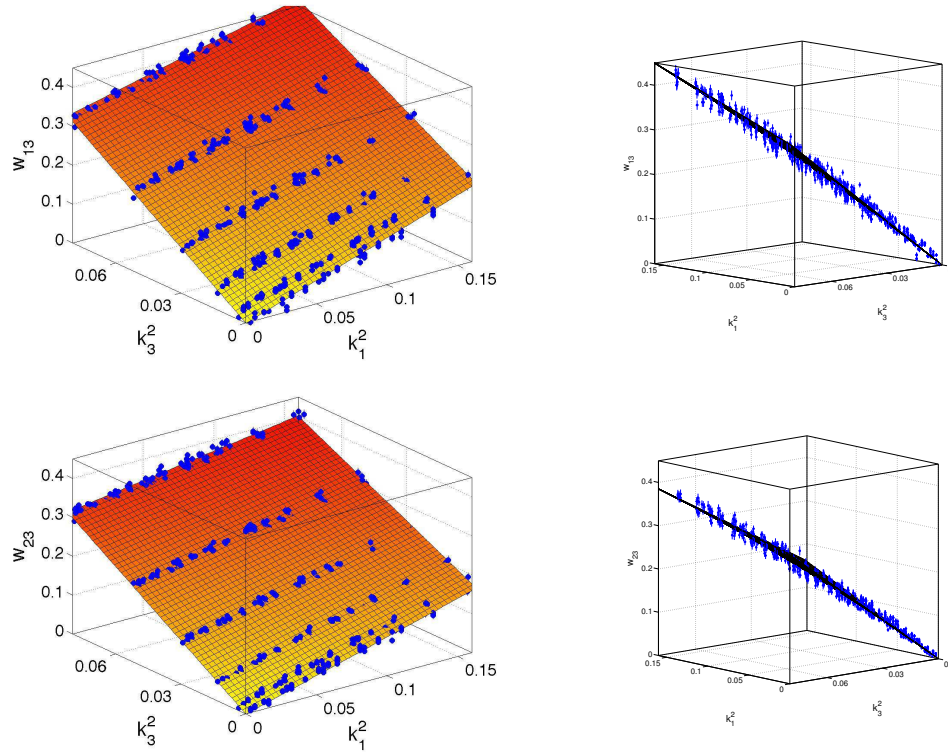


Figure 3.1: Surface fitting results for  $W_{13}$  and  $W_{23}$  as a function of  $k_1^2$  and  $k_3^2$  at temperature  $T = 3.0$  and density  $\rho = 0.38$  for the system GB(3, 5, 2, 1). Simulation results are shown as blue points with error bars. Surface fits are shown from two different angles.

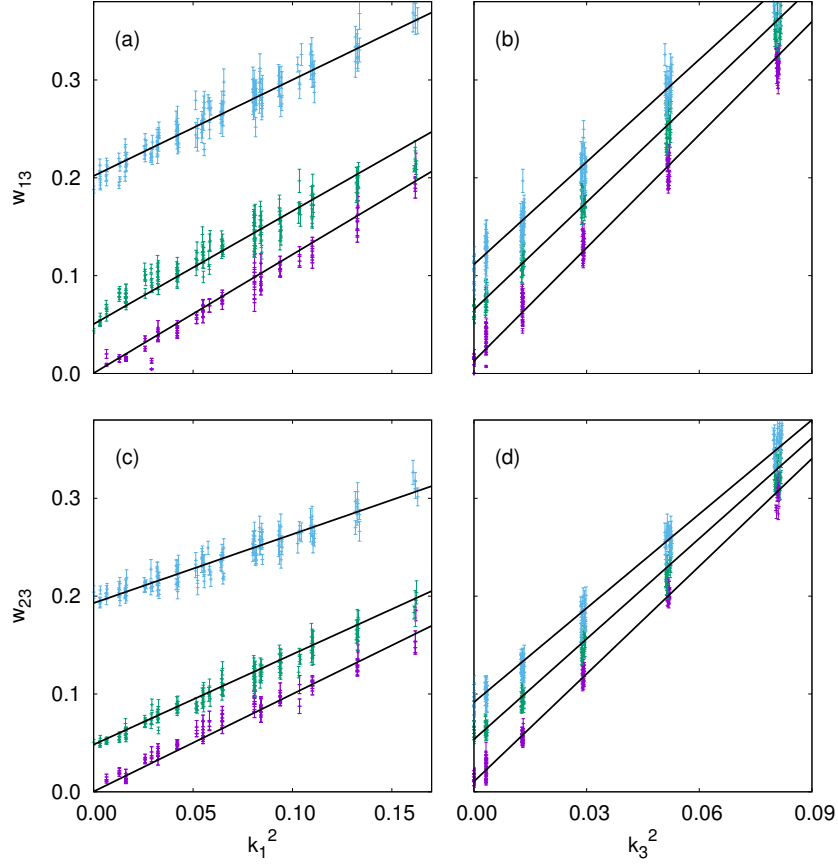


Figure 3.2: Slices through  $W_{13}$  and  $W_{23}$  results and fitted surfaces as a function of  $k_1^2$  and  $k_3^2$ , at temperature  $T = 3.0$  and density  $\rho = 0.38$  for the system GB(3, 5, 2, 1). For clarity only three out of six slices are plotted in each case. (a)  $W_{13}$  splay fluctuations; (b)  $W_{13}$  bend fluctuations; (c)  $W_{23}$  twist fluctuations; (d)  $W_{23}$  bend fluctuations.

we show edge-on views in Figure 3.1, and, in Figure 3.2, slices through the fitted surface along the  $k_1^2$  and  $k_3^2$  axes. In each direction, six slices were chosen such that roughly 1/6 of the data points lay within each slice. The slices perpendicular to  $k_3$  correspond very closely to  $k_3 \sim k_z = 2\pi\kappa_z/L_z$  with  $\kappa_z = 0, \dots, 5$ ; the slices perpendicular to  $k_1$  each contain a range of values (corresponding to combinations of  $k_x$  and  $k_y$  in the box frame). Again, a good fit was observed for all six state points.

The obtained fitting coefficients  $p_{01}$  and  $p_{10}$  correspond directly to  $K_1$ ,  $K_3$  respectively for the  $W_{13}$  fit, and to  $K_2$ ,  $K_3$  respectively for the  $W_{23}$  fit. The elastic constants  $K_1$ ,  $K_2$ ,  $K_3$  obtained from the fits are given in Table 3.1. We observe



that  $K_3$  values obtained from both fits are similar and that  $K_3 \gg K_1 \approx K_2$ . This agrees with observations that, in a nematic phase formed from elongated particles, the splay and twist elastic constants are almost equivalent, whereas bend excitations require most energy. For all GB parameterisations we observe an increase in the elastic constants for denser state points.

A word is needed about the estimated errors on the elastic constants, reported in Table 3.1. The fitting process yields 95% confidence limits on the fit parameters, which reflect the statistical errors on the data points, but these do not tell the whole story. There is an additional uncertainty due to the key choices of how many  $k$ -points to include, and how high a polynomial to use for the fitting surface. These choices are, of course, interconnected. The use of a very large system eliminates most of the curvature in the  $W_{mm'}(k_1^2, k_3^2)$  surfaces and the very high coefficients of determination  $R^2$  justify the use of the low-order function, Equation (3.5). Having done this, we systematically varied the range of  $(k_1^2, k_3^2)$ , and hence the number of points, included in the fit, until  $R^2$  began to fall significantly below the level quoted in Table 3.1. The spread in parameters determined across these fits gave an estimate of the imprecision in elastic constants due to this choice, which was added to the statistical error estimate. The results, given in Table 3.1, are reasonably consistent with the difference in the  $K_3$  values between the independent fits to  $W_{13}$  and  $W_{23}$  surfaces. Without this correction, the error bars would be unreasonably optimistic, typically by a factor of 2–3.

The simulations for GB(3, 5, 2, 1) and GB(3, 5, 1, 3) were repeated with 8000 Gay-Berne molecules, and other details unchanged, to analyse finite size effects. Results are given in Table 3.2. As expected the order parameter is slightly higher than for the large systems. The values of the order tensor fluctuations  $W_{mm'}$  are consistent for both system sizes in the regime of low  $k$  that we analysed for large simulations. However, for the small system, only a relatively small number (20–30) of data points lie in this regime. To obtain a fit with reasonable error bars on the fitting parameters, it is necessary to extend to larger  $k$  and add higher order terms to the fitting function, to account for the curvature observed in the data at higher  $k$ -values. For the 8000-particle system, we added terms in  $k_1^4$  and  $k_3^4$  to the form of Equation (3.5). However, the value of this approach is limited, in the sense that the extra terms simply give a better fit to the higher- $k$  points, and the elastic constants are still determined by the relatively few points near the origin. This can be clearly seen in the figures of Ref. [80], for the same-sized system. For the reasons discussed above, we do not attempt to put error bars on the elastic constant estimates in Table 3.2. We re-emphasise that discrepancies between the values in Tables 3.1 and

Table 3.2: Results for 8000 Gay-Berne molecules. Notation as for Table 3.1. Coefficients of determination  $R^2$  for the fits were 0.99 or better in all cases.

$\rho$	$T$	$\langle S \rangle$	$W_{13}$ fit		$W_{23}$ fit	
			$K_1$	$K_3$	$K_2$	$K_3$
GB(3,5,2,1)						
0.32	0.9	0.59(1)	0.46	1.27	0.54	1.34
0.33	1.0	0.67(1)	0.70	2.31	0.78	2.41
0.35	2.0	0.61(1)	1.36	3.83	1.11	3.90
0.38	3.0	0.72(1)	3.22	11.23	2.35	11.50
GB(3,5,1,3)						
0.3	3.4	0.63(1)	2.92	5.32	2.60	5.43
0.3	3.45	0.59(2)	2.58	4.59	2.29	4.66

3.2 reflect difficulties of fitting the data in the latter case; the measured data points themselves are fully consistent with those of the present study, when the very small differences in order parameter are taken into account.

Our results do not compare so well with the original ones of Allen *et al.* [80]; in particular, their measured order parameters are different from ours. This turns out to be due to the smaller cutoff of  $r_{\text{cut}} = 4\sigma_0$  used in that work, in addition to the use of a potential which was shifted to eliminate the discontinuity (see Section 2.2.3). Both potentials are illustrated in Figure 3.3 for the end-to-end configuration. (The value of  $r_{\text{cut}}$  was not made clear in the original paper, but was stated in an accompanying paper by the same authors [157]; this value, or more generally  $r_{\text{cut}} = (\kappa + 1)\sigma_0$ , was quite standard at the time [117, 158, 159]). As can be seen in Figure 3.3, the effect of truncation, particularly in configurations close to the end-to-end arrangement, can be significant. It is important to realise that, because the shift correction depends on the orientations of the particles and the direction of the centre-centre vector, it does actually generate torques and forces in the simulation, and therefore affects the dynamics and simulation averages. Using the MD package GBMOLDD [124], with the shorter cutoff, we have duplicated the order parameter measurements of Ref [80], confirming that the chosen cutoff makes a significant difference. Therefore, we do not attempt to make a close comparison with the elastic constants measured in that paper. We found that our results are in moderate agreement with the ones found by Joshi *et al.* [152] using free energy perturbation measurements. At density  $\rho = 0.33$  and temperature  $T = 1.0$  (unknown  $r_{\text{cut}}$ ), for GB(3,5,2,1), they obtained  $K_{1,2,3} = \{0.958, 0.91, 2.44\}$ , which may be compared

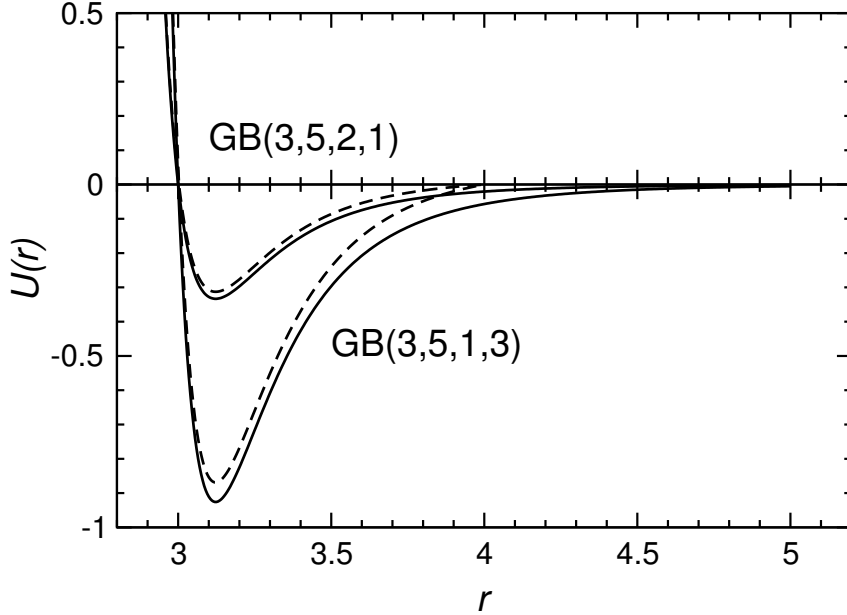


Figure 3.3: Gay-Berne potential for the end-to-end configuration ( $\hat{\mathbf{u}}_i$ ,  $\hat{\mathbf{u}}_j$  and  $\mathbf{r}_{ij}$  all parallel), for the GB(3,5,2,1) and GB(3,5,1,3) models. Solid lines show the unshifted potential, which is cut at  $r_{\text{cut}} = 5\sigma_0$  in this work. Dashed lines show the potential cut at  $r_{\text{cut}} = 4\sigma_0$  and shifted, as used in Ref. [80].

with our values in Tables 3.1 and 3.2. We note that Joshi *et al.* [152] used system sizes  $725 \leq N \leq 8910$ , and claimed to find no evidence of system-size effects in the upper part of this range. Bearing in mind that they measured the free energy associated with a single deformation mode in each case, it is not clear how significant this finding is.

### 3.5 Conclusions

We have calculated the Frank elastic constants of the Gay-Berne fluid for three different parameterisations at various state points using molecular dynamics. We have shown that for a sufficiently large simulation box, the elastic constants can be extrapolated from the equilibrium orientational fluctuations. We found that  $K_3 \gg K_1 \approx K_2$  for all state points and parameterisations. This agrees with the expectation that for elongated particles the bend excitation requires the most energy. The elastic constants depend strongly on the density, showing an increase for higher densities at roughly constant order parameter. In comparing with previous work, we have highlighted the advantages of using a larger simulation box, so as to give a larger range over which the asymptotic behaviour of the director fluctuations may

be fitted. Our fluctuation measurements are consistent with those made on a much smaller system; however the fitting process itself can be somewhat more robust for the larger systems. A limitation, however, is the rapid increase in correlation times, and associated statistical errors, for the lowest- $k$  modes.

## Chapter 4

# Dynamics in nematic liquid crystals

In this Chapter we present the dynamics of Gay-Berne nematics by calculating the time correlation functions of the director and velocity fluctuations. These results were published [1, 2]. The theoretical analysis was contributed by M. P. Allen.

### 4.1 Introduction

Most of the interesting properties of nematic liquid crystals are determined by the Frank elastic constants  $K_1$ ,  $K_2$  and  $K_3$  appearing in the static continuum theory [12, 140, 141], and the various Leslie coefficients  $\alpha_1 \dots \alpha_6$  (viscosities), which enter the equations of nematodynamics [15–17, 20, 146]. The orientational relaxation of the space- and time-dependent nematic director  $\mathbf{n}(\mathbf{r}, t)$ , and its coupling to the hydrodynamic velocity field  $\mathbf{v}(\mathbf{r}, t)$ , may be accessed experimentally at low wavenumber  $k$  and frequency  $\omega$  by dynamic light scattering. Ever since the first analysis of such experiments, it has been argued on the basis of the relative orders of magnitudes of the elastic and viscosity coefficients [160, 161], that these modes decay exponentially, rather than oscillating in time. For example, the review of Stephen and Straley [161] states: “The orientation fluctuations of the director are coupled to the fluid velocity by viscous effects, and in fact are overdamped: the modes which the elastic theory ... predicts do not propagate”. Similar statements appear in the textbook derivations [6, 9] and this view has been supported by experiment over subsequent years [162–165].

Particle-based molecular simulations allow us to connect the values of the coefficients of orientational elasticity and viscosity to molecular structure and in-

teractions, and verify the assumptions of the continuum theory. In this chapter we present the dynamics of the order tensor, which is coupled to hydrodynamic flow, as a function of wave vector. We show how the director fluctuations decay with time, and that the bend fluctuations unexpectedly decay in an oscillatory fashion. We also report the time correlation functions for transverse velocity (momentum), showing how these are also consistent with the equations of nematodynamics [15–17, 20, 146].

In Section 4.2 we summarise the relevant equations for the time correlation functions. Details of the simulation model used, and other simulation details, are given in Section 4.3. Simulation results are presented in Section 4.4 and conclusions are drawn in Section 4.6.

## 4.2 Theoretical background

The dynamics in the nematic phase can be studied by calculating time correlation functions of the components of the director, or equivalently the order tensor. Recall that the order tensor  $\mathbf{Q}$  in reciprocal space is given by

$$\tilde{Q}_{mm'}(\mathbf{k}) = \frac{V}{N} \sum_{i=1}^N \left( \frac{3}{2} \hat{u}_{im} \hat{u}_{im'} - \frac{1}{2} \delta_{mm'} \right) \exp(i\mathbf{k} \cdot \mathbf{r}_i). \quad (4.1)$$

Here  $\delta_{mm'}$  is the Kronecker delta, we define Cartesian components  $m, m' = x, y, z$ ,  $N$  is the number of molecules,  $V$  is the volume and  $\hat{\mathbf{u}}_i$  and  $\mathbf{r}_i$  are the orientation vector and the molecular position vector of each molecule  $i$  respectively and  $\mathbf{k}$  is the wave vector. (We restrict our interest to uniaxial molecules). We define a new orthonormal Cartesian axis system  $(\hat{\mathbf{e}}_1, \hat{\mathbf{e}}_2, \hat{\mathbf{e}}_3)$ , where  $\hat{\mathbf{e}}_3$  is along the director. In this system  $\hat{\mathbf{n}} = (0, 0, 1)$ ; small fluctuations of the director may be expressed  $(n_1, n_2, 0)$  and these are proportional to the elements  $Q_{13}$  and  $Q_{23}$ . Without loss of generality the axes are chosen such that the wave vectors lie in the  $\hat{\mathbf{e}}_1$ – $\hat{\mathbf{e}}_3$  plane, i.e.  $\mathbf{k} = (k_1, 0, k_3)$ . To analyse the dynamics we calculate the time correlation functions of components of the director, or equivalently the order tensor

$$c_m^n(\mathbf{k}, t) = \frac{\langle \tilde{n}_m(\mathbf{k}, t) \tilde{n}_m(-\mathbf{k}, 0) \rangle}{\langle |\tilde{n}_m(\mathbf{k})|^2 \rangle} = \frac{\langle \tilde{Q}_{m3}(\mathbf{k}, t) \tilde{Q}_{m3}(-\mathbf{k}, 0) \rangle}{\langle |\tilde{Q}_{m3}(\mathbf{k})|^2 \rangle}, \quad m = 1, 2 \quad (4.2)$$

where it is understood that, in finite-time simulations, the dynamical variables have their average values subtracted off:  $\tilde{Q}_{mm'} \rightarrow \tilde{Q}_{mm'} - \langle \tilde{Q}_{mm'} \rangle$ . Here, the separate

splay, twist and bend fluctuations are of interest, defined by

$$c_{\text{splay}}^n(k, t) = c_1^n(k\hat{\mathbf{e}}_1, t) , \quad (4.3a)$$

$$c_{\text{twist}}^n(k, t) = c_2^n(k\hat{\mathbf{e}}_1, t) , \quad (4.3b)$$

$$c_{\text{bend}}^n(k, t) = c_1^n(k\hat{\mathbf{e}}_3, t) = c_2^n(k\hat{\mathbf{e}}_3, t) . \quad (4.3c)$$

We also calculate Fourier components of the velocity field  $\mathbf{v}(\mathbf{r})$ , denoted  $\tilde{\mathbf{v}}(\mathbf{k}) = (\tilde{v}_1, \tilde{v}_2, \tilde{v}_3)$

$$\tilde{v}_m(\mathbf{k}) = \frac{V}{N} \sum_{i=1}^N v_{im} \exp(i\mathbf{k} \cdot \mathbf{r}_i) , \quad (4.4)$$

and their time correlation functions

$$c_m^v(\mathbf{k}, t) = \frac{\langle \tilde{v}_m(\mathbf{k}, t) \tilde{v}_m(-\mathbf{k}, 0) \rangle}{\langle |\tilde{v}_m(\mathbf{k})|^2 \rangle} , \quad m = 1, 2, 3 . \quad (4.5)$$

In the regime of interest, it is possible to assume that the fluid is incompressible,  $\nabla \cdot \mathbf{v} = 0$ . In Fourier space, this becomes  $i\mathbf{k} \cdot \tilde{\mathbf{v}} = 0$ , or, in the coordinate system defined above,  $k_1\tilde{v}_1 + k_3\tilde{v}_3 = 0$ . For the pure splay, twist and bend deformations above, either  $k_1$  or  $k_3$  is zero, and so this condition may be used to eliminate one of the velocity components. It turns out that the following modes couple to director fluctuations as follows:

$$c_{\text{splay}}^v(k, t) = c_3^v(k\hat{\mathbf{e}}_1, t) , \quad (4.6a)$$

$$c_{\text{twist}}^v(k, t) = c_2^v(k\hat{\mathbf{e}}_1, t) , \quad (4.6b)$$

$$c_{\text{bend}}^v(k, t) = c_1^v(k\hat{\mathbf{e}}_3, t) = c_2^v(k\hat{\mathbf{e}}_3, t) . \quad (4.6c)$$

These are all transverse (shear) modes, i.e. the velocity component is perpendicular to the wave-vector.

These calculations are simplified if the director can be arranged to lie along one of the box Cartesian axes, for instance  $\hat{\mathbf{e}}_3 = \hat{\mathbf{z}}$ , so that the desired wave vectors are compatible with the cubic periodic boundary conditions. In this case, in Equations (4.3a) and (4.3b), it is possible to choose (at least) two perpendicular wave vector directions  $\hat{\mathbf{e}}_1$  (e.g.  $\hat{\mathbf{e}}_1 = \hat{\mathbf{x}}, \hat{\mathbf{y}}$ ) for each value of  $k$ , thereby improving statistics and giving an additional error estimate. In Equation (4.3c), combining the two equivalent expressions for  $c_{\text{bend}}^n(k, t)$  fulfils a similar function, and corresponding arrangements can be made for Equations (4.6a–4.6c).

At low- $k$ , we expect these correlation functions to be consistent with ne-

Table 4.1: Basic relations for velocity coefficients

Basic relation	Definition
$\gamma_1 = \alpha_3 - \alpha_2$	Rotational or twist viscosity
$\eta_1 = \frac{1}{2}(\alpha_3 + \alpha_4 + \alpha_6)$	Miesowicz viscosity along flow direction $\mathbf{n} \parallel \mathbf{v}$
$\eta_2 = \frac{1}{2}(\alpha_4 + \alpha_5 - \alpha_2)$	Miesowicz viscosity along gradient direction $\mathbf{n} \parallel \nabla \mathbf{v}$
$\eta_3 = \frac{1}{2}\alpha_4$	Miesowicz viscosity along vorticity direction $\mathbf{n} \parallel (\mathbf{v} \times \nabla \mathbf{v})$

matodynamics: the coupled equations in Fourier space for hydrodynamic flow and director reorientation [19, 160, 161]. The link between microscopic time correlation functions, and macroscopic transport equations, is a standard exercise in linear response theory, which may be tackled through the projection operator formalism [166–169]. We consider the twist, splay, and bend modes separately. The basic relations for several viscosity coefficients [160, 161] used in the following derivation are given in Table 4.1.

For the twist deformation,  $k_1 = k$ ,  $k_3 = 0$ , and incompressibility implies that the velocity component  $\tilde{v}_1 \equiv 0$ . The relaxation equations involve the pair of variables  $\{\tilde{n}_2, \tilde{v}_2\}$ :

$$(\gamma_1 \partial_t + K_2 k^2) \tilde{n}_2 = 0 , \quad (4.7a)$$

$$(\rho \partial_t + \eta_3 k^2) \tilde{v}_2 = 0 , \quad (4.7b)$$

where  $\partial_t$  denotes the time derivative;  $\rho$  is the mass density. In Equation (4.7) the director twist  $\tilde{n}_2$  and the transverse velocity  $\tilde{v}_2$  are decoupled, and relax independently:

$$\begin{aligned} \tilde{n}_2 &\propto \exp(-\nu_{\text{twist}}^n t) , & \nu_{\text{twist}}^n &= \lambda_{\text{twist}}^n k^2 , & \lambda_{\text{twist}}^n &= K_2 / \gamma_1 , \\ \tilde{v}_2 &\propto \exp(-\nu_{\text{twist}}^v t) , & \nu_{\text{twist}}^v &= \lambda_{\text{twist}}^v k^2 , & \lambda_{\text{twist}}^v &= \eta_3 / \rho , \end{aligned}$$

where the rotational viscosity  $\eta_{\text{twist}} \equiv \gamma_1$ . For typical values of the transport coefficients, elastic constants, and mass densities, these relaxation rates are well separated:

$$\frac{\nu_{\text{twist}}^n}{\nu_{\text{twist}}^v} = \frac{\lambda_{\text{twist}}^n}{\lambda_{\text{twist}}^v} = \frac{\rho K_2}{\eta_3 \gamma_1} \ll 1 . \quad (4.8)$$

The equilibrium time correlation functions  $c_{\text{twist}}^n(k, t)$  and  $c_{\text{twist}}^v(k, t)$  are predicted to decay exponentially, with corresponding decay rates  $\nu_{\text{twist}}^n$  and  $\nu_{\text{twist}}^v$  respectively.

For the splay deformation, again  $k_1 = k$ ,  $k_3 = 0$ , so  $\tilde{v}_1 \equiv 0$ , and the relaxation



equations in the variables  $\{\tilde{n}_1, \tilde{v}_3\}$ , are

$$(\gamma_1 \partial_t + K_1 k^2) \tilde{n}_1 + i k \alpha_3 \tilde{v}_3 = 0, \quad (4.9a)$$

$$-i k \alpha_3 \partial_t \tilde{n}_1 + (\rho \partial_t + \eta_1 k^2) \tilde{v}_3 = 0, \quad (4.9b)$$

where  $\eta_1$  is another Miesowicz viscosity, and  $\alpha_3$  is a Leslie coefficient. These equations may be solved in standard fashion as a matrix eigenvalue problem. A secular equation for the decay rates is obtained by substituting  $\partial_t \rightarrow -\nu = -\lambda k^2$ :

$$\begin{vmatrix} -\nu \gamma_1 + K_1 k^2 & i k \alpha_3 \\ i k \nu \alpha_3 & -\nu \rho + \eta_1 k^2 \end{vmatrix} = 0$$

$$\Rightarrow \lambda^2 \rho \gamma_1 + \lambda (\alpha_3^2 - \gamma_1 \eta_1 - \rho K_1) + K_1 \eta_1 = 0. \quad (4.10)$$

If the timescale separation still applies, the two roots will be real, and will obey  $\lambda \ll \lambda'$ , in which case

$$\lambda'_{\text{splay}} \approx \frac{\eta_1 - \alpha_3^2/\gamma_1 + \rho K_1/\gamma_1}{\rho},$$

$$\lambda_{\text{splay}} \approx \frac{K_1}{\gamma_1 - \alpha_3^2/\eta_1 + \rho K_1/\eta_1} \equiv \frac{K_1}{\eta_{\text{splay}}},$$

where  $\eta_{\text{splay}} = \gamma_1 - \alpha_3^2/\eta_1 + \rho K_1/\eta_1 \approx \gamma_1 - \alpha_3^2/\eta_1$ . Director splay fluctuations are expected to be dominated by this slow mode  $\lambda_{\text{splay}}$ , relaxing exponentially

$$\begin{aligned} \tilde{n}_1 &\propto \exp(-\nu_{\text{splay}}^n t), & \nu_{\text{splay}}^n &= \lambda_{\text{splay}}^n k^2, & \lambda_{\text{splay}}^n &= K_1/\gamma_1' & \gamma_1' &= \gamma_1(1 - \chi) \\ \tilde{v}_3 &\propto \exp(-\nu_{\text{splay}}^v t), & \nu_{\text{splay}}^v &= \lambda_{\text{splay}}^v k^2, & \lambda_{\text{splay}}^v &= \eta_1'/\rho, & \eta_1' &= \eta_1(1 - \chi). \end{aligned}$$

The factor  $\chi = (\alpha_3^2 - \rho K_1)/\eta_1 \gamma_1$ , where we expect  $|\chi| \ll 1$ , slightly modifies the rotational and Miesowicz viscosities. The timescale separation becomes

$$\frac{\nu_{\text{splay}}^n}{\nu_{\text{splay}}^v} = \frac{\lambda_{\text{splay}}^n}{\lambda_{\text{splay}}^v} = \frac{\rho K_1}{\eta_1' \gamma_1'} \ll 1. \quad (4.11)$$

For bend fluctuations,  $k_1 = 0$ ,  $k_3 = k$ , and  $\tilde{v}_3 \equiv 0$  by incompressibility. The coupled relaxation equations for the pair  $\{\delta \tilde{n}_1, \tilde{v}_1\}$  (and similarly for  $\{\delta \tilde{n}_2, \tilde{v}_2\}$ ) are

$$(\gamma_1 \partial_t + K_3 k^2) \delta \tilde{n}_1 + i k \alpha_2 \tilde{v}_1 = 0, \quad (4.12a)$$

$$-i k \alpha_2 \partial_t \delta \tilde{n}_1 + (\rho \partial_t + \eta_2 k^2) \tilde{v}_1 = 0, \quad (4.12b)$$

where  $K_3$  is the bend elastic constant. Substituting  $\partial_t \rightarrow -\nu = -\lambda k^2$  gives the secular equation

$$\begin{aligned} & \begin{vmatrix} -\nu\gamma_1 + K_3k^2 & ik\alpha_2 \\ ik\nu\alpha_2 & -\nu\rho + \eta_2k^2 \end{vmatrix} = 0 \\ \Rightarrow & \lambda^2\rho\gamma_1 + \lambda(\alpha_2^2 - \gamma_1\eta_2 - \rho K_3) + K_3\eta_2 = 0. \end{aligned} \quad (4.13)$$

A similar argument to the splay case would give well-separated real roots

$$\begin{aligned} \lambda'_{\text{bend}} & \approx \frac{\eta_2 - \alpha_2^2/\gamma_1 + \rho K_3/\gamma_1}{\rho}, \\ \lambda_{\text{bend}} & \approx \frac{K_3}{\gamma_1 - \alpha_2^2/\eta_2 + \rho K_3/\eta_2} \equiv \frac{K_3}{\eta_{\text{bend}}}, \end{aligned}$$

where  $\eta_{\text{bend}} = \gamma_1 - \alpha_2^2/\eta_2 + \rho K_3/\eta_2 \approx \gamma_1 - \alpha_2^2/\eta_2$ . This leads to the usual prediction that bend relaxation is overdamped, occurring at a rate  $\nu_{\text{bend}} = K_3k^2/\eta_{\text{bend}}$ . However, our simulation results clearly do not conform to this: instead they correspond to complex roots (and hence a propagating mode)

$$\lambda_{\text{bend}} = \lambda_{\text{bend}}^{\text{r}} + i\lambda_{\text{bend}}^{\text{i}}.$$

The conditions for which complex roots arise are discussed in detail in the later discussion section.

### 4.3 Simulation details

The time correlation functions were calculated for a cubic system of 512 000 Gay-Berne molecules for the state point  $\rho\sigma_0^3 = 0.3$ ,  $k_{\text{B}}T/\epsilon_0 = 3.4$  with at the GB(3,5,1,3). The system was prepared as described in Section 3.3 with two modifications. Firstly, the timestep was reduced to  $\Delta t = 0.002\tau_0$  and secondly the production run was simulated in the microcanonical  $NVE$  ensemble to confirm that the thermostating does not affect the results obtained. We also calculated the time correlation functions of the director fluctuations  $c_m^n(\mathbf{k}, t)$  for the  $NVT$  data described in Section 3.3. The elastic constants (see Chapter 3) were recalculated using these shorter,  $NVE$ , runs to ensure that none of the changes described influence the results. Indeed we find that the elastic constants only deviate by a few percent from the ones calculated using the longer  $NVT$  runs. The equilibration run was 400 000, followed by a production run of 1 000 000 time steps with snapshots stored every 500 time steps. All

time correlation functions were calculated over the whole length of the production run from the stored configurations.

## 4.4 Data analysis and results

All of our results are calculated as functions of wave vector  $\mathbf{k}$ . In cubic periodic boundary conditions, this is restricted to

$$\mathbf{k} = \frac{2\pi}{L}(\kappa_x, \kappa_y, \kappa_z) . \quad (4.14)$$

Here  $\kappa_x, \kappa_y, \kappa_z$  are integers, and the box length  $L \gtrsim 95\sigma_0$ . In our calculations we restricted interest to  $-5 \leq \kappa_x, \kappa_y \leq 5$  and  $0 \leq \kappa_z \leq 5$ , excluding  $\mathbf{k} = (0, 0, 0)$ .

The time correlation functions of the director  $c_m^n(k, t)$  were calculated from the components of the order tensor  $\tilde{Q}_{13}$  and  $\tilde{Q}_{23}$ , defined in Equation (4.3), which are proportional to the director fluctuations  $\tilde{n}_1$  and  $\tilde{n}_2$ . In Figure 4.1 we can see that these time correlation functions  $c^n(k, t)$  follow an exponential decay for the splay and twist mode with the decay rates increasing with increasing wave number  $k$ . For the bend mode we observe an oscillation in addition to the exponential decay, i.e. it is a propagating mode. Although this possibility had always been allowed by the nematodynamic theory [166], it had not (to our knowledge) been observed before in experiment, or simulation. A detailed description that places these findings into context can be found in the next Section 4.5.

We also calculated the time correlation functions of the velocity fluctuations  $c^v(k, t)$ , defined in Equation (4.6). The results are plotted in Figure 4.2. Similar to the director fluctuations they follow an exponential decay for splay and twist modes, and an oscillatory exponential decay for the bend mode. However both the splay and twist velocity fluctuations decay faster than their corresponding director correlation functions, while the two decay rates for the bend mode are almost identical. All these observations are consistent with the equations of nematodynamics, described in Section 4.2. We estimated the decay rates by fitting the time correlation functions in Figure 4.1 and Figure 4.2 to the function  $\Re \exp(-\nu t)$  allowing complex  $\nu$  ( $\Re$  stands for “real part”).

For the splay and twist mode the decay rates  $\nu_{\text{splay}}$  and  $\nu_{\text{twist}}$  were real with a negligible complex part; whereas for the bend mode we found an oscillatory decay rate corresponding to complex  $\nu_{\text{bend}}$ . In Figure 4.3 the decay rates  $\nu_{\text{splay}}$  and  $\nu_{\text{twist}}$  are plotted against  $k^2$  for the director and velocity fluctuations. Errors were estimated from repeating the fits independently for four equally long subruns of

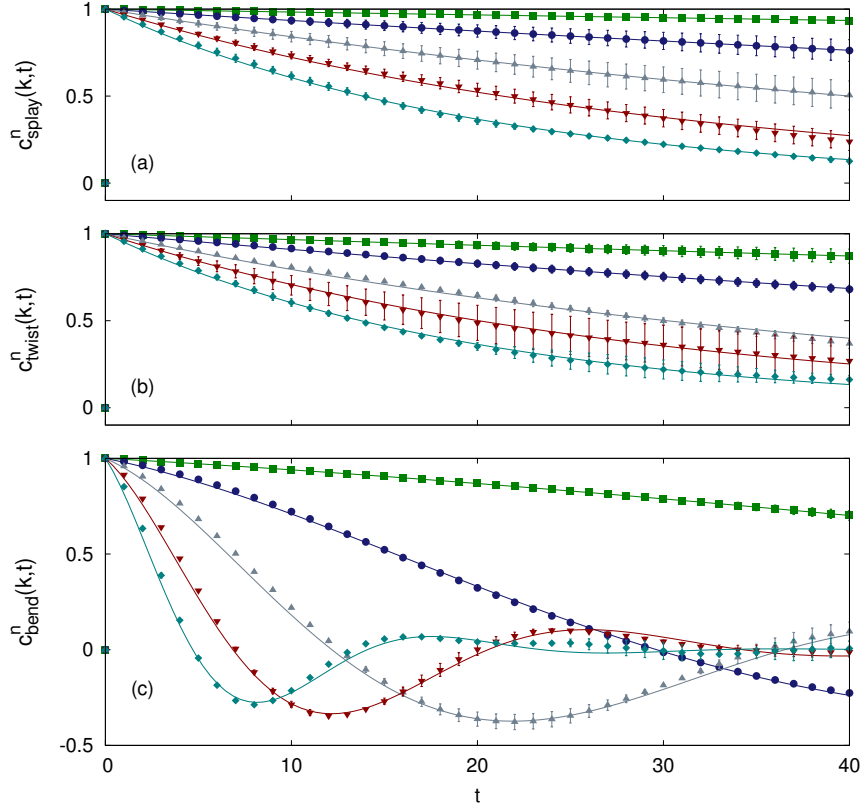


Figure 4.1: Time correlation functions of the director fluctuations  $c^n(k, t)$  plotted versus time  $t$  in units of  $\tau_0$  at  $\rho\sigma_0^3 = 0.3$ ,  $k_B T/\epsilon_0 = 3.4$ , for GB(3,5,1,3). (a)  $c_{\text{splay}}^n(k, t)$  (b)  $c_{\text{twist}}^n(k, t)$  (c)  $c_{\text{bend}}^n(k, t)$ . Points with error bars are simulation results. Continuous lines correspond to fitted curves  $c = \Re \exp(-\nu t)$ , where  $\nu$  is a complex number. Different curves correspond to different wavenumbers  $k = \kappa 2\pi/L$  where  $L$  is the simulation box length:  $\kappa = 1$  (squares, green);  $\kappa = 2$  (circles, blue);  $\kappa = 3$  (up-triangles, grey);  $\kappa = 4$  (down-triangles, red);  $\kappa = 5$  (diamonds, cyan).

250 000 timesteps. All four relaxation rates calculated are accurately proportional to  $k^2$ . There is no significant difference in gradient between the splay and twist for the director fluctuations; whereas for the velocity fluctuations the two gradients differ. We estimate the gradient of the decay rates versus  $k^2$  by calculating a linear fit through the origin for the set of points corresponding to different wave vectors. The proportionality factors  $\lambda^n$  and  $\lambda^v$  are listed in Table 4.2. For the lowest values of  $k$ , the decay times are in the order of magnitude of 100 000 time steps. This confirms the need to take care in assessing errors in the elastic fluctuations in Chapter 3, where elastic constants are calculated, because the decay times become comparable with the run length.

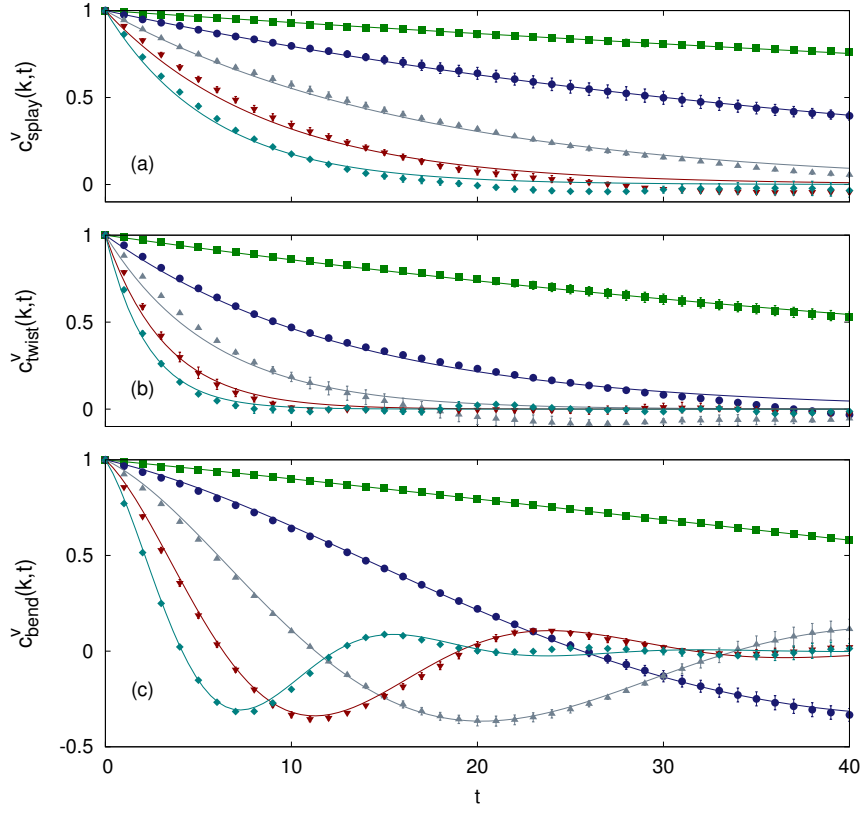


Figure 4.2: Time correlation functions of the velocity fluctuations  $c^v(k, t)$  plotted versus time  $t$  in units of  $\tau_0$  at  $\rho\sigma_0^3 = 0.3$ ,  $k_B T/\epsilon_0 = 3.4$ , for GB(3,5,1,3). (a)  $c_{\text{splay}}^v(k, t)$  (b)  $c_{\text{twist}}^v(k, t)$  (c)  $c_{\text{bend}}^v(k, t)$ . Notation as in Figure 4.1.

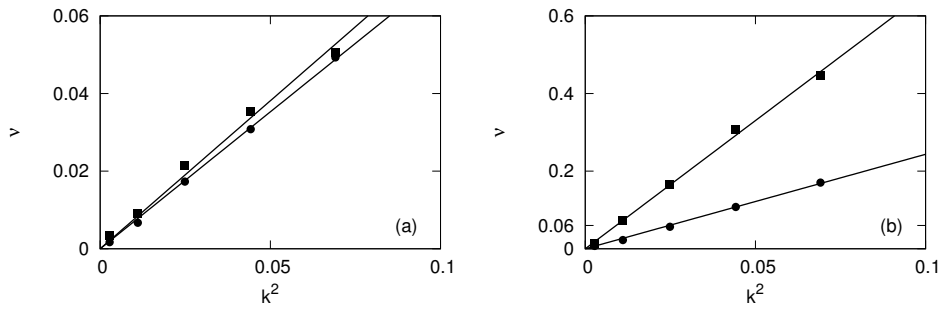


Figure 4.3: Relaxation rates  $\nu$  as a function of  $k^2$  obtained from fitting  $\exp(-\nu t)$  to (a) director time correlation functions  $c_m^n(k, t)$  in Figure 4.1; (b) velocity time correlation functions  $c_m^v(k, t)$  in Figure 4.2. The state point is  $\rho\sigma_0^3 = 0.3$ ,  $k_B T/\epsilon_0 = 3.4$ , for GB(3,5,1,3). Circles and squares correspond to the splay and twist mode respectively. Straight lines are linear regression through origin.

Table 4.2: Proportionality factors  $\lambda$  relating the relaxation rates of the director and velocity correlations to  $k^2$  for GB(3,5,1,3) and  $\rho = 0.3$ ,  $T = 3.4$ . Values are obtained from the gradients of the linear fits through the origin in Figures 4.3 and 4.4.

$\lambda^n$				$\lambda^v$			
$\lambda_{\text{splay}}$	$\lambda_{\text{twist}}$	$\lambda_{\text{bend}}^r$	$\lambda_{\text{bend}}^i$	$\lambda_{\text{splay}}$	$\lambda_{\text{twist}}$	$\lambda_{\text{bend}}^r$	$\lambda_{\text{bend}}^i$
0.7(1)	0.76(15)	1.97(7)	4.95(16)	2.43(9)	6.60(10)	2.11(4)	5.54(12)

For the splay and twist mode it is notable that the decay rates of the velocity fluctuations are almost an order of magnitude larger than for the director fluctuations. For the chosen state point the timescale separation for the twist mode is most prominent with  $\lambda_{\text{twist}}^v/\lambda_{\text{twist}}^n \approx 9$ . For the splay mode the timescale separation is still significant with  $\lambda_{\text{splay}}^v/\lambda_{\text{splay}}^n \approx 3.5$ . This separation of timescales is expected from nematodynamics, Equations (4.8) and (4.11). For the bend mode the real and imaginary parts of the relaxation rate  $\nu$  are plotted against  $k^2$  in Figure 4.4. Once again we find that both decay rates are exactly proportional to  $k^2$  for both the real and the imaginary part. In contrast to the splay and twist modes, the velocity and director bend correlation functions relax and oscillate on almost exactly the same timescales, which we will explain in the discussion. Qualitatively similar dynamics

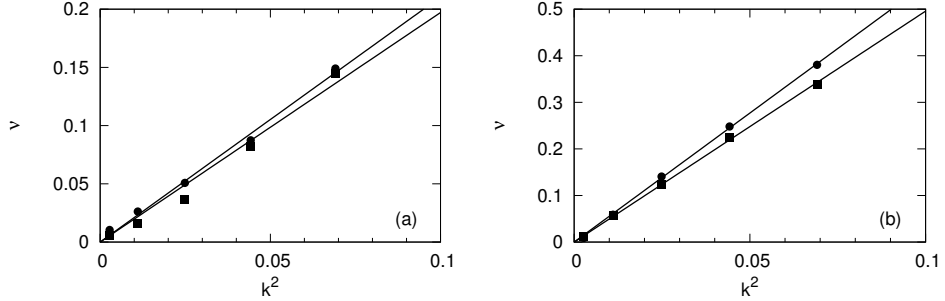


Figure 4.4: Relaxation rates  $\nu_{\text{bend}}$  for bend fluctuations of the director (squares) and the velocity (circles) with (a) the real part (b) the imaginary part. These parameters were obtained from the fits to  $c_m^n(k, t)$  in Figure 4.1(c) and  $c_m^v(k, t)$  in Figure 4.2(c). The state point is  $\rho\sigma_0^3 = 0.3$ ,  $k_B T/\epsilon_0 = 3.4$ , for GB(3,5,1,3). Straight lines are linear regression through origin.

were observed for all other state points analysed in Chapter 3. The proportionality factors of the relaxation rates to  $k^2$  for these are reported in Table 4.3. Note that the run time for these simulations was roughly twice as long as the *NVE* ones and that the time step used was  $\Delta t = 0.004$ .

Table 4.3: Proportionality factors relating the relaxation rates of the director correlations to  $k^2$  for all state points analysed in Chapter 3. Estimated errors in the last quoted digit are given in parentheses.

$\rho$	$T$	$\lambda_{\text{splay}}$	$\lambda_{\text{twist}}$	$\lambda_{\text{bend}}^r$	$\lambda_{\text{bend}}^i$
GB(3, 5, 2, 1)					
0.32	0.9	0.15(1)	0.17(1)	1.4(1)	1.5(1)
0.33	1.0	0.15(1)	0.17(1)	1.6(1)	2.5(1)
0.35	2.0	0.17(1)	0.16(1)	2.1(1)	2.4(1)
0.38	3.0	0.22(1)	0.21(1)	2.9(1)	4.9(1)
GB(3, 5, 1, 3)					
0.3	3.4	0.66(1)	0.64(1)	1.96(2)	4.81(3)
0.3	3.45	0.70(1)	0.70(1)	2.11(6)	4.08(6)

## 4.5 Discussion

In this Section we will argue that some experimental systems might have transport coefficients, which obey an inequality necessary to exhibit the propagating behaviour observed. To see how these arise, it is helpful to define two dimensionless quantities

$$\mu = \frac{\rho K_3}{\gamma_1 \eta_2} , \quad \alpha = 1 - \frac{\alpha_2^2}{\gamma_1 \eta_2} .$$

We expect  $\mu \sim 10^{-2}$  like the similar quantities defined above for twist and splay. Certainly, in both experiment [19, Table D.3], and simulation [81], typically  $\eta_2 \gtrsim \gamma_1$ , but also  $K_3 \gtrsim K_2$ , so  $\mu = \rho K_3 / \gamma_1 \eta_2 \approx \rho K_2 / \gamma_1^2$ . The discriminant of the quadratic equation (4.13) gives complex roots if

$$(\alpha + \mu)^2 < 4\mu \quad \Rightarrow \quad |\alpha| \lesssim 2\sqrt{\mu} ,$$

assuming that  $\mu \ll 1$ . This is quite possible, depending on how close the viscosities  $\gamma_1$ ,  $\eta_2$ , and  $\alpha_2$  happen to be to each other. We already know that  $\gamma_1 = \alpha_3 - \alpha_2 \approx |\alpha_2|$ , since  $\alpha_3$  is typically small, so if  $\eta_2 \approx |\alpha_2|$ , a small value of  $\alpha$  will indeed result.

If  $\mu \sim 10^{-4}$ , then complex roots will only result if  $|\alpha| < 0.02$ ; however, if  $\mu \sim 10^{-2}$ , complex roots will arise if  $|\alpha| < 0.2$ . To put this in context, Table D.3 of Ref. [19] gives typical experimental values of  $\alpha = 0.18, 0.19, 0.23$  for MBBA near 25 °C, 5CB near 26 °C, and PAA near 122 °C, respectively. Wang et al. [170] have estimated the Leslie coefficients for the standard mixture E7, from which  $\alpha = 0.06$

near 20 °C. Even smaller values come from theories, and from molecular simulation measurements of viscosities [81, 171–174]. The simulation results of Wu et al. [82], for the model GB(3.0, 5.0, 1, 2) [175], at  $T = 2.5$ ,  $\rho = 0.295$ , give  $\alpha \approx 0.01$ . The theory of Kuzuu and Doi [176] for rod-like molecules predicts a value of  $\alpha < 0.004$  over the entire nematic range. An affine transformation theory [177, 178] predicts values  $\alpha < 0.1$  for molecules of elongation  $\kappa \geq 3$  at modest nematic order parameters, and  $\alpha \equiv 0$  in the perfectly aligned limit.

The parameter  $\alpha$  appears in the continuum theory of switching phenomena, such as the homeotropic to planar-bend Freedericksz transition (see e.g. Chapter 5 of Ref. [19]). The influence of small values of  $\alpha$  on backflow and kickback effects in such cases is well understood, but the generation of oscillatory director fluctuations in the bulk at low  $k$  seems to have been overlooked. Our results show that these are easily observed in computer simulations of a range of coarse-grained molecular models. Moreover, they suggest that, even though overdamped decay is the norm in experiments, real-life examples might be found for which the secular equation (4.13) has complex roots, and the bend mode propagates. In this event, the roots are given by

$$\begin{aligned}\lambda_{\text{bend}}^{\text{r}} &= (\alpha + \mu) \left( \frac{\eta_2}{2\rho} \right) , \\ \lambda_{\text{bend}}^{\text{i}} &= \sqrt{4\mu - (\alpha + \mu)^2} \left( \frac{\eta_2}{2\rho} \right) ,\end{aligned}$$

both the prefactors being significantly smaller than 1. From the ratios  $\lambda_{\text{bend}}^{\text{i}}/\lambda_{\text{bend}}^{\text{r}}$  measured in our simulations we can estimate  $0.5 \lesssim \mu/(\mu + \alpha)^2 \lesssim 2$ , which is completely consistent with  $\alpha \sim \sqrt{\mu}$ . The velocity field, of course, will be governed by the same dynamics as the director: there is no separation of timescales.

## 4.6 Conclusions

In conclusion, we have observed that the time correlation functions of the director and the velocity fluctuations decay exponentially for the splay and twist modes, but show oscillatory decay for the bend mode. The decay rates were found to be accurately proportional to  $k^2$ . The analysis of the separation of timescales between the director fluctuations and the velocity fluctuations showed that the separation is most prominent for the twist mode and reasonably large for the splay mode. For the bend mode the velocity field is expected to be governed by the same dynamics as the director and, indeed, we did not observe a significant separation of timescales.



We have shown that all these observations are consistent with the equations of nematodynamics [15–17, 20, 146]. In particular we have shown that the propagating modes may occur without violating the (traditionally assumed) condition  $\mu = \rho K_3 / \gamma_1 \eta_2 \ll 1$ . Values of  $\mu \sim 10^{-2}$  may be sufficient to generate such modes, and seem to be quite typical in coarse-grained particle-based simulations, probably because the viscosities of such molecular models are somewhat smaller than in realistic systems. At this point it is worth noting that there are several unrealistic features of the Gay-Berne potential. For example an increase in molecular length makes an unrealistic difference to the density range for which a nematic phase is stable. This in turn has large effects on bulk properties as shown for the rotational viscosities by Cuetos et al. [83]. It would be interesting to analyse the fluctuations in a non-Gay Berne simulation to confirm that the observations are not simply an artefact of the Gay-Berne potential.

The key requirement is that the dimensionless viscosity combination  $\alpha = 1 - \alpha_2^2 / \gamma_1 \eta_2$  satisfies  $\alpha \lesssim 2\sqrt{\mu}$ . This may still be attainable, even for the somewhat smaller values of  $\mu$  typically seen in experiment, depending on the precise values of the viscosities  $\alpha_2$ ,  $\gamma_1$ , and  $\eta_2$ . Therefore, it may not be out of the question to observe such propagating bend modes in real-life experimental systems. Similar conditions are unlikely to be satisfied for the splay modes, because the analogous key quantity is  $1 - \alpha_3^2 / \gamma_1 \eta_1$ , and the Leslie coefficient  $\alpha_3$  is typically quite small compared with the others.

## Chapter 5

# Topological defects around a nanoparticle inserted into a nematic

### 5.1 Introduction

A spherical particle in a nematic host induces the creation of topological defects. A profound understanding of how such defects form and behave is important, since they significantly change the properties of the surrounding liquid crystal (LC). Several types of defects have been observed around spherical particle inclusions. The particular type of defect depends on many different factors. Amongst others the size of the particle, its surface anchoring strength and the boundary conditions are important. In Fig. 5.1 director maps of the different defects observed are shown. For more details refer to Section 1.6.

In this chapter we study defects induced by nanoparticle inclusions with strong surface anchoring using molecular simulations. Here the size of the nanoparticle is comparable to the size of the liquid crystal molecules. Interestingly very small particles with strong surface anchoring create distortions over macroscopic distances, similar to larger particles with weak surface anchoring [46]. The aim of this study is to gain insight into the formation of these defects on a molecular level and to study the properties of the defect core. There are numerous reasons to use computer simulations in addition to experimental and theoretical work. Theoretical predictions have proven to be successful for simple problems; however finding analytical expressions becomes more and more complex the more parameters are considered and the higher the number of particles in the system. For the majority

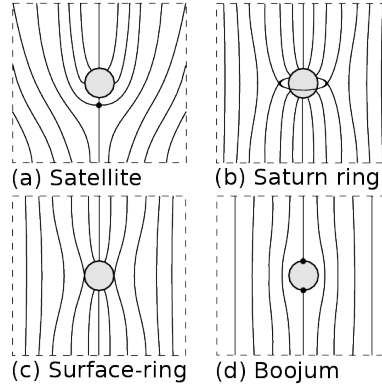


Figure 5.1: Sketch of director field around a particle inclusion: (a) satellite, (b) Saturn ring, (c) Surface-ring and (d) boojum.

of complex systems only approximations can be found. Even though defects can be observed in experiments using crossed polarisers, microscopes cannot provide true real-time 3D imaging. Furthermore defects are extremely difficult to observe for very small particle inclusions or for very high densities of particle inclusions. Numerical calculations using elastic theory are a very powerful tool to study defects. One limitation is that the defect core is treated as an isotropic inclusion, where the energy associated with the defect region is used as an adjustable parameter. However this energy is, in fact, unknown. Moreover the elastic theory treats the liquid crystal as purely uniaxial, however it has been shown that the defect core is biaxial throughout [21, 179]. These difficulties are avoided in molecular simulations and hence they are a valuable additional approach to study defects in liquid crystals. The major limitation of simulations is the system size. Only a small fraction of the LC molecules found in a real experiment can be simulated. In summary, computer simulations provide us with a tool to investigate details of the LC structure that are difficult to study experimentally or using phenomenological theories.

Previous attempts have been made to simulate defects around particles in liquid crystals on a molecular level. Billeter and Pelcovits [98] simulated a small spherical inclusion with homeotropic anchoring embedded in 2048 Gay-Berne molecules (see Section 2.3 for Gay-Berne potential), which induced a Saturn ring. Later Andrienko et al. [25] showed that finite size effects are important. For a purely repulsive Gay-Berne system with a spherical inclusion, they found the Saturn ring to be stable for all inclusions with radii ranging from  $3 - 15\sigma_0$ . In addition they discovered that the satellite defect is metastable (on the timescale of the simulations) for the largest particles investigated. Here the particle was embedded in 1 million Gay-Berne host molecules, which allows for the far field deformations of the director field necessary

to stabilise a dipolar defect (see Fig. 5.1 (a)). They also observed an off-centre ring defect structure, which is an unstable intermediate structure between the Saturn ring and the satellite. This defect structure has not been observed in experiments [46] and numerical LdG free energy minimisations do also not predict a stable off-centre ring. Recently Ilnytskyi et al. [107] studied defects induced by soft colloids using molecular dynamics simulations. Here a soft colloid is not a particle itself; instead it consists of a spherical region in which the LC molecules are exposed to an external ordering field. As for hard colloids a Saturn ring or a boojum defect were observed depending on the orientation of the anchoring field.

Both theoretical work and Monte Carlo simulations suggest that the satellite defect tends to be stable for large particles and that the Saturn ring is stable for small particles [23, 27, 28]. Attempts were made to estimate the threshold, for which the dipolar structure becomes unstable, as a function of particle size. However analytical calculations and experiments seem to contradict each other. On the one hand, theoretically the Saturn ring is predicted to be the only stable defect for particle radii of less than a few hundred nanometers [29]. On the other hand, dipoles were observed in experiments with particles as small as 125 nm [30] and even 35 nm [31]. In addition, Gu and Abbott [180] and Mondain-Monval et al. [181] observed Saturn rings around solid microspheres, although theory suggests a satellite for particles this size. A possible explanation is the strong confinement due to the cell thickness.

As discussed in Chapter 1 two particles in a nematic interact due to the elastic forces trying to minimise the deformation of the LC, which can lead to the formation of complex networks [37, 43, 48, 49, 182]. These systems have mostly been studied for micron-sized inclusions, for which the surrounding defects can be observed under the microscope and the interaction forces can be measured accurately using dual beam laser trapping [36, 183]. Only few experiments have studied the interactions of nanoparticles in nematics. Poulin et al. [184] and Raghunathan et al. [185] observed the formation of chains and clusters of latex particles of size 60 – 120 nm in lyotropic liquid crystals and Koenig et al. [186] found weak long-range interactions for gold nanoparticles of radius 85 nm. During the self-assembly of micron-sized particles, the particles often become trapped in states of higher energy, since the thermal energy is too low to overcome the barrier towards the lowest energy state. Koenig et al. [186] showed that the interactions of nanoparticles are reversible allowing the assembly of well-ordered nanoparticle structures. Tomar et al. [106] studied pair interactions of nanoparticles with both homeotropic and planar anchoring. Both showed attractive interactions, which are stronger for homeotropic anchoring in comparison to planar anchoring.

Table 5.1: Simulation parameters of simulations of nanoparticle inclusions in a nematic host. #GB and #NP correspond to the number of Gay-Berne molecules and number of nanoparticles respectively.  $U_{\text{GB}}$  describes the version of GB potential used (see text).  $T$ ,  $I$  and  $\rho$  are the temperature, the moment of inertia and the bulk density respectively in GB units  $\epsilon_0 = \sigma_0 = 1$ .  $\langle S \rangle$  is the time averaged bulk order parameter.  $R_{\text{NP}}$  denotes the radius of the nanoparticle and SA indicates the surface anchoring used.

ID	#GB	#NP	$U_{\text{GB}}$	$T$	$I$	$\rho$	$\langle S \rangle$	$R_{\text{NP}}$	SA
(1)	512 000	1	GB(3, 5, 1, 3)	3.0	2.5	0.3	0.75	3-15	homeo
(2)	512 000	1	GB(3, 5, 1, 3)	3.0	0.5	0.3	0.75	13	planar
(3)	1 000 000	1	GB(3, 0, 0)	1.0	2.5	0.35	0.81	15	homeo
(4)	1 000 000	1	GB(3, 0, 0)	1.0	2.5	0.354	0.835	20	homeo
(5)	1 000 000	1	GB(5, 0, 0)	1.0	7.0	0.15	0.86	15	homeo
(6)	588 000	2	GB(3, 5, 1, 3)	3.0	2.5	0.31	0.80	15	homeo

In this chapter we investigate the behaviour of nanoparticle inclusions in a nematic host and study the interactions of two nanoparticles using molecular simulations. For particles in very close vicinity entanglement of the particles by a single defect line was observed. These results are discussed in detail in Chapter 6.

## 5.2 Model and simulation details

Molecular simulations were carried out over a range of different interaction potentials, surface anchoring conditions and sizes of nanoparticle inclusions. The corresponding simulation details for the various simulation runs are listed in Table 5.1. The nematic host was simulated using the Gay-Berne (GB) potential (see Section 2.3). The notation  $\text{GB}(\kappa, \kappa', \mu, \nu)$  is used to refer to different versions of the standard potential and  $\text{GB}(\kappa, 0, 0)$  for the purely repulsive one. For all simulations the time step was set to  $\Delta t = 0.004$ . The GB-GB potential cutoff was chosen to be  $5.0\sigma_0$  for the standard GB potential and  $6.0\sigma_0$  for the purely repulsive one. At the cutoff distances the energy is negligibly small even for the end-to-end interactions. For simulation (1)-(5) a cubic simulation box was used, whereas for simulation (6) the ratio was 1.7:1:1 to accommodate for the second particle. Simulation (1) was repeated with nanoparticle inclusions of radii 3, 5, 10 and  $15\sigma_0$ . The different defect structures were visualised using the various methods described in Section 2.4. In the following the potential used for the interaction of the nanoparticle with the GB molecules is introduced. For simulations (1)-(5) the nanoparticles' position was

fixed at the origin, whereas for simulation (6) the particles were allowed to move freely throughout the production run.

## Homeotropic and planar surface anchoring potential

### Homeotropic

Instead of using a specific anchoring potential, a simple variation of the standard Lennard-Jones (LJ) 12-6 potential is used. Here the anchoring is entirely induced by the packing effects of the LC particles near the surface of the nanoparticle. For the homeotropic surface anchoring the GB molecules are allowed to penetrate the nanoparticles' surface. To prevent GB molecules from entirely entering the particle, a shifted purely repulsive LJ interaction potential  $U_{\text{homeo}}$

$$U_{\text{homeo}}(\mathbf{r}) = \begin{cases} 4\epsilon_0 (\varrho^{-12} - \varrho^{-6}) + \epsilon_0 & \text{if } \varrho^6 < 2 \\ 0 & \text{else} \end{cases} \quad (5.1)$$

is used.  $\epsilon_0$  is an energy parameter chosen to be unity and  $\varrho$  is given by

$$\varrho = \frac{|\mathbf{r}| - \sigma_c + \sigma_0}{\sigma_0}. \quad (5.2)$$

Here  $\mathbf{r}$  is the vector connecting the positions of the nanoparticle and the GB molecule and  $\hat{\mathbf{r}}$  is the corresponding unit vector.  $\sigma_0$  is a size parameter and defined as the smallest diameter of the GB molecule; in this system  $\sigma_0 = 1$ .  $\sigma_c$  is the distance of the closest approach between the GB molecule and the nanoparticle and is set to

$$\sigma_c = R_{\text{NP}} + \sigma_0/2, \quad (5.3)$$

where  $R_{\text{NP}}$  is the radius of the spherical nanoparticle. For this interaction potential the potential cutoff is chosen to be  $R_{\text{NP}} + 1$ .

### Planar

The potential used to induce planar surface anchoring is very similar to  $U_{\text{homeo}}$ . However  $\sigma_c$  is defined to be orientation dependent, such that the GB molecules are repelled when they overlap with the nanoparticle. The potential  $U_{\text{planar}}$  is given by

$$U_{\text{planar}}(\mathbf{r}, \hat{\mathbf{u}}_i) = \begin{cases} 4\epsilon_0 (\varrho^{-12} - \varrho^{-6}) + \epsilon_0 & \text{if } \varrho^6 < 2 \\ 0 & \text{else.} \end{cases} \quad (5.4)$$

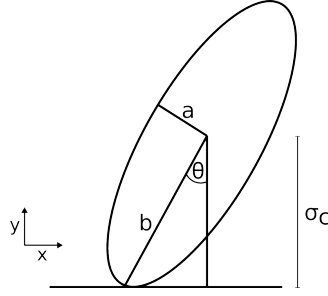


Figure 5.2: Schematic to illustrate notation  $x$ ,  $y$  and  $\theta$  used in the derivation of the closest approach distance  $\sigma_c$  for planar surface anchoring.

$\mathbf{r}$ ,  $\hat{\mathbf{r}}$  and  $\epsilon_0$  are defined as before,  $\hat{\mathbf{u}}_i$  is the orientation vector of the GB molecule  $i$  and  $\varrho$  is given by Equation (5.2). If the minor axis of the GB molecule is defined as  $a = \sigma_0/2$  and the major axis as  $b = \kappa\sigma_0/2$ , the distance of closest approach  $\sigma_c$  can be defined as

$$\sigma_c(\hat{\mathbf{u}}_i) = R_{\text{NP}} + \sqrt{a^2(1 - (\hat{\mathbf{r}} \cdot \hat{\mathbf{u}}_i)^2) + b^2(\hat{\mathbf{r}} \cdot \hat{\mathbf{u}}_i)^2}. \quad (5.5)$$

This can be derived as follows. Consider the plane defined by the ellipsoid's axis and the surface normal of the nanoparticle, see Fig. 5.2, where  $x$ ,  $y$ ,  $\theta$  and  $\sigma_c$  are defined, then the equation describing the shape of the GB molecule centred at the origin and rotated by  $\theta$  in 2D is given by

$$\frac{(x \cos \theta + y \sin \theta)^2}{a^2} + \frac{(x \sin \theta - y \cos \theta)^2}{b^2} = 1. \quad (5.6)$$

By evaluating  $dy/dx$  and equating the numerator to zero the horizontal tangents of the ellipse can be found. The distance of the closest approach can alternatively be expressed in terms of  $\theta$

$$\sigma_c(\theta) = R_{\text{NP}} + \sqrt{a^2 \sin^2 \theta + b^2 \cos^2 \theta}, \quad (5.7)$$

the angle enclosed by  $\mathbf{r}$  and  $\hat{\mathbf{u}}_i$ . For this interaction potential the potential cutoff is chosen to be  $R_{\text{NP}} + \kappa$ .

### External potential favouring the satellite or Saturn ring defect structure

As discussed earlier a spherical particle inclusion in a nematic distorts the surrounding director field. For large particles with homeotropic anchoring the director shows a dipolar structure and for smaller particles it usually shows a quadrupolar struc-

ture (see Fig. 5.1). Here analytical expressions for the surrounding director field are introduced for both, the satellite and the Saturn ring. Spherical polar coordinates are used and the nanoparticle is assumed to be centred at the origin.

### Satellite

Theoretical studies by Shiyanovskii and Kuksenok [24] proposed a trial function for the distortion angle  $\beta$  for the satellite defect

$$\beta(r, \theta) = \theta - \arctan \left( \frac{\sin \theta}{1/f(r) + \cos \theta} \right). \quad (5.8)$$

Here  $r$  and  $\theta$  are the radial component and azimuthal angle respectively.  $f(r)$  is introduced later. Note that Equation (5.8) was modified by removing the factor of 0.5 in front of the arctan function. With the factor the director field has a  $-1/2$  disclination around the defect, instead of the expected  $-1$ . Furthermore the total defect strength is  $+1/2$  instead of the zero. For a given distortion function  $\beta$  the theoretical director orientation  $\hat{\mathbf{n}}(\mathbf{r})$  can be calculated. For given angles  $\phi$  and  $\beta$ ,  $\hat{\mathbf{n}}(\mathbf{r})$  is given by a combination of a clockwise rotation by  $\beta$  around the  $y$ -axis and a clockwise rotation by  $\phi$  around the  $z$ -axis

$$\hat{\mathbf{n}}(\mathbf{r}) = \begin{pmatrix} \cos \phi \cdot \sin \beta \\ \sin \phi \cdot \sin \beta \\ \cos \beta \end{pmatrix}. \quad (5.9)$$

The function  $f(r)$  in Equation (5.8) has to fulfil two boundary conditions that (1)  $1/f(\infty) = 0$  hence  $\beta = 0$  corresponding to the absence of distortion in the director far field and (2) that  $f(a) = 1$ , where  $a$  is the distance between the centre of the defect core and the centre of the particle inclusion. Kuksenok et al. [26] proposed

$$f(r) = (r/a)^3. \quad (5.10)$$

Theoretical calculations suggest  $a \sim 1.46R_{\text{NP}}$  [24],  $a \sim 1.23R_{\text{NP}}$  [13] and  $a \sim 1.19R_{\text{NP}}$  [28] for the satellite defect. Far away from the particle inclusion the director distortion behaves as

$$\beta \sim \left( \frac{R}{r} \right)^2 \sin \theta. \quad (5.11)$$



### Saturn ring

For a quadrupolar defect the distortion angle  $\beta$  can be described by

$$\beta = \theta - 0.5 \arctan \left( \frac{\sin(2\theta)}{1/f(r) + \cos(2\theta)} \right). \quad (5.12)$$

The core of the defect is predicted to be closer to the surface than for the dipole with  $a \sim 1.25R_{\text{NP}}$  [26]. For the quadrupole the distortion of the surrounding director field decays significantly quicker with

$$\beta \sim \left( \frac{R}{r} \right)^3 \sin 2\theta. \quad (5.13)$$

An external field can be applied to the Gay-Berne molecules to favour a dipolar or quadrupolar defect structure around the nanoparticle. The field induces an energy penalty if the orientation of the molecules  $\hat{\mathbf{u}}$  deviates from the theoretical director field  $\hat{\mathbf{n}}$ . The external potential for a molecule  $i$  can be written as

$$U_i(r, \theta, \phi, \hat{\mathbf{u}}_i) = -\epsilon_{\text{sat}}(\hat{\mathbf{n}} \cdot \hat{\mathbf{u}}_i)^2, \quad (5.14)$$

where  $\epsilon_{\text{sat}}$  is the strength of the external field.

GBMOLDD was modified to include the homeotropic and planar interaction potential as well as the external potential favouring the satellite or Saturn ring defect as described in this and the previous section.

## 5.3 Data analysis and results

### 5.3.1 Saturn ring defect

System (1) (Table 5.1) was equilibrated over  $3 \times 10^5$  time steps in the absence of a nanoparticle inclusion with a final bulk order parameter  $S = 0.750 \pm 0.001$ . A nanoparticle was gradually grown in size over  $1 \times 10^4$  time steps to radii ranging from  $3$  to  $15\sigma_0$ . Once the particle had reached the desired size, the system was equilibrated ( $NVT$  ensemble) over  $6 \times 10^5$  time steps, followed by a production run ( $NVE$  ensemble) of  $4 \times 10^5$  time steps with system snapshots stored every 2500 time steps. For particles with radii of  $R_{\text{NP}} = 3\sigma_0$  and  $5\sigma_0$  a surface-ring defect can be seen and for radii  $10\sigma_0$  and  $15\sigma_0$  a Saturn ring was observed. In Fig. 5.3 the time averaged order parameter, biaxiality, director field and density are plotted in the  $x$ - $z$  plane with the particle at the origin for a bin size of  $\sim 1\sigma_0$ . In addition a QMGA snapshot of the simulation is shown for a single snapshot and

the corresponding defect regions of low uniaxial order ( $c_l < 0.12$ ) are visualised. In the QMGA snapshots blue molecules are parallel to the director and red molecules are perpendicular with intermediate orientations corresponding to green molecules. The local order parameter maps show that the uniaxial order drops significantly in the region of the defect core. Simultaneously the biaxiality defined by the lowest ( $S_3$ ) and intermediate ( $S_2$ ) eigenvalue of the order tensor

$$\alpha = \frac{1}{3}(S_2 - S_3) \quad (5.15)$$

increases in the defect region. One can also see that larger particles induce longer ranged distortions, which is in agreement with Equation (5.13). The surrounding nematic shows strong oscillations in density near the particle. Each oscillation reflects one molecular layer that can be seen in the QMGA system snapshot. Larger particle inclusions induce more oscillations. Note that the oscillations appear to be damped near the defect core. The Westin visualisation shows the defect region for a single time step. A Saturn ring can be seen for nanoparticles of size  $5\sigma_0$ ,  $10\sigma_0$  and  $15\sigma_0$  confirming that this visualisation method is very useful for extracting information about an instantaneous snapshot. Furthermore thermal fluctuations can be resolved, which usually disappear in the averaging process. We see that for larger particles the distance of the defect from the particle increases. For each nanoparticle size the distance of the defect core from the nanoparticle's surface  $a - R_{\text{NP}}$  is calculated by fitting a circular function to all bins with  $S < 0.3$ . In Fig. 5.4 the average distance of the defect region from the surface of the particle is plotted over different radii.

From Fig. 5.4 we can deduce that the distance of the defect core from the surface of the nanoparticle is  $a - R_{\text{NP}} \sim 0.13R_{\text{NP}} + 0.8\sigma_0$ . Note that this is likely to be subject to a larger error due to the low number of points; the gradient obtained should be regarded as an indicator only. The estimate compares well with Andrienko et al. [25]'s simulation, which estimated  $a - R_{\text{NP}} \sim 0.16R_{\text{NP}} - 0.33\sigma_0$ . Here the difference is likely to be caused by the choice in locating the core region and the choice of state point. The results compare well to theoretical predictions leading to values of  $a \sim 1.25R_{\text{NP}}$  [26] and  $a \sim 1.08R_{\text{NP}}$  [28] as well as Landau-de Gennes free energy minimisation estimating  $a \sim 1.15R_{\text{NP}}$ .

### 5.3.2 Boojum defect

System (2) (Table 5.1) was equilibrated ( $NpT$ ) over  $10 \times 10^6$  time steps, followed by a production run ( $NpT$ ) of  $6 \times 10^4$  time steps with snapshots stored every 100

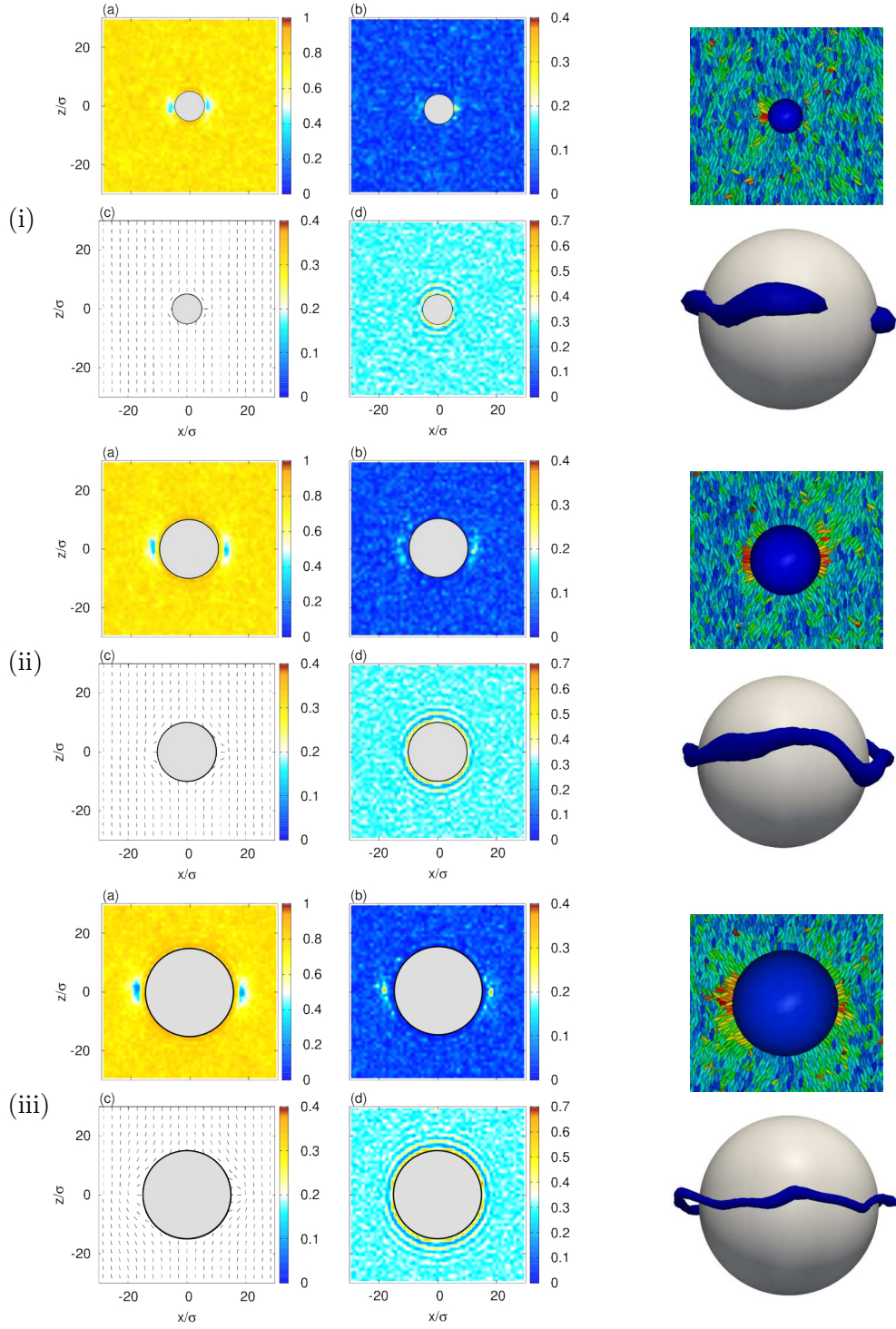


Figure 5.3: Analysis for single nanoparticle inclusion in a nematic host with (i)  $R_{\text{NP}} = 5\sigma_0$ , (ii)  $R_{\text{NP}} = 10\sigma_0$  and (iii)  $R_{\text{NP}} = 15\sigma_0$ . Left shows time averaged maps correspond to (a) local order parameter  $S$ , (b) local biaxiality  $\alpha$ , (c) local director  $\hat{\mathbf{n}}$  and (d) local density  $\rho$ . Right shows QMGA snapshot for a single time step. It also shows the Westin defect region corresponding to  $c_l < 0.12$ .

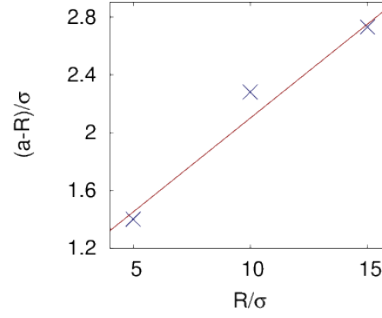


Figure 5.4: Distance of the defect region from the surface of the nanoparticle  $a - R_{\text{NP}}$  plotted versus the radius of the nanoparticle.

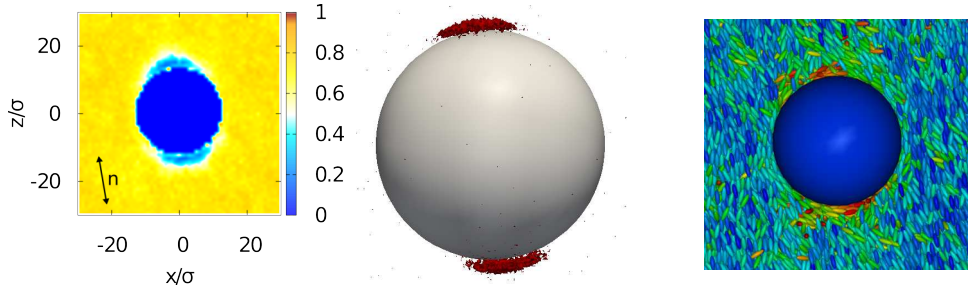


Figure 5.5: Left: local order  $S$  plotted in the  $x$ - $z$  plane with the nanoparticle at the origin. The director orientation is indicated by the black two-headed arrow. Centre: regions of low uniaxial order  $S < 0.3$  (red) are plotted for time-averaged simulation results. Right: QMGA snapshot of nanoparticle with planar anchoring.

time steps. In Fig. 5.3 the time averaged local order parameter map is plotted. Note that in this simulation the director is not parallel to  $z$ ; its orientation is indicated by the two-headed arrow. In addition, Fig. 5.3 shows the time averaged defect regions corresponding to  $S < 0.3$  visualised in 3D. One can see the two boojums defect regions, in which the uniaxial order drops significantly. The defects are positioned directly on the surface at opposites poles with respect to the director.

### 5.3.3 Satellite defect

In the following we describe the attempts made to stabilise the satellite defect around a nanoparticle inclusion for several Gay-Berne systems. System (3) was equilibrated over  $2 \times 10^5$  time steps using the purely repulsive GB potential and a molecule length-to-width ratio  $\kappa = 3$ . A spherical nanoparticle of radius  $R_{\text{NP}} = 15\sigma_0$  was placed at the centre of the simulation box. Throughout the  $4 \times 10^5$  time steps long production run ( $NVT$ ) the external potential, given in Equation (5.14), was applied

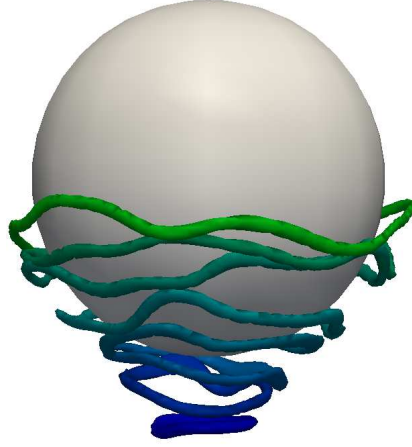


Figure 5.6: Visualisation of defect regions ( $c_l < 0.1$ ) for different time steps with fixed nanoparticle at the centre. Time steps shown correspond to  $0.5 \times 10^4$  (blue),  $2 \times 10^4$ ,  $2.5 \times 10^4$ ,  $3.5 \times 10^4$ ,  $5 \times 10^4$ ,  $10 \times 10^4$ ,  $20 \times 10^4$ ,  $50 \times 10^4$  (green).

to support the satellite defect. Throughout the production run the strength of the external field was steadily reduced from  $\epsilon_{\text{sat}} = 1 \rightarrow 0$ . Initially ( $\epsilon_{\text{sat}} = 1$ ) a small disclination loop can be observed below the pole of the nanoparticle with respect to the director. Note that the position could equally be above the opposite pole due to symmetry; however it is determined by our choice of Equation (5.8). The radius of the loop is comparable to the length of the GB molecules. When the external field is weak ( $\epsilon_{\text{sat}} \lesssim 0.3$ ), the disclination loop rapidly (within a few thousands time steps) increases in size and its centre shifts towards the equator of the nanoparticle. The simulation was continued for  $5 \times 10^5$  time steps in the absence of the external field. Fig. 5.6 shows the disclination lines for different time steps. Since the dynamics are fast at the start and then decelerate significantly, snapshots are shown more frequently for earlier time steps. To quantify the dynamics of the transition, Fig. 5.7 shows the average  $z$  position of the defect line versus time, as well as the  $z$  position versus the average radius of the defect ring. It can be seen that the defect moves towards the equator of the nanoparticle. Initially the transition dynamics are very fast and follow an exponential behaviour. These dynamics are in agreement with observation made by Andrienko et al. [25]. The speed of the transition explains why off-centre rings are not observed in experiments. The average  $z$  position versus  $R$  shows that the defect line closely follows the contours of the spherical nanoparticle. Fig. 5.7 suggests that once the absolute  $z$  position of the defect is smaller than the radius of the nanoparticle, the  $z$  position can be estimated accurately with  $a = 1.123R_{\text{NP}}$ , see blue fitted curve, to calculate the distance of the defect from the

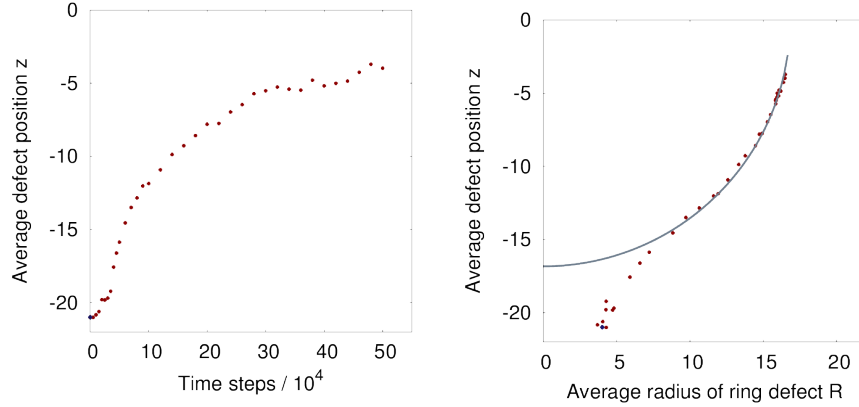


Figure 5.7: Left: average  $z$  position of the defect line obtained by averaging all  $z$  coordinates with  $c_l < 0.1$  for each time step respectively. The first ten points are in  $5 \times 10^3$  time step intervals, the next five in  $1 \times 10^4$  and all remaining points are  $2 \times 10^4$  time steps apart. Right: average  $z$  position versus the average radius of the ring defect calculated by fitting all  $x$  and  $y$  values with  $c_l < 0.1$  to a circle. The blue circle corresponds to the radius  $R = 16.845$ .

centre of the particle.

The simulation was repeated with more elongated LC molecules with  $\kappa = 5$ . System details are given in Table 5.1 system (5). As before the external field favouring the satellite structure was continuously applied with  $\epsilon_{\text{sat}} = 1 \rightarrow 0$  over  $3 \times 10^5$  time steps and the simulation was continued in the absence of an external field.  $5 \times 10^4$  time steps after the field was switched off the defect ring had moved towards the equator and the radius of the defect ring had increased significantly. The structural changes in the defect and the time scale of this transition were very similar to the previous simulation with  $\kappa = 3$ .

Since the size of the nanoparticle is a crucial factor to determine the stability of the satellite defect structure, the runs were repeated with a larger nanoparticle of radius  $R_{\text{NP}} = 20\sigma_0$ , see system (4). When the external field was applied with  $\epsilon_{\text{sat}} = 1$ , the small disclination loop collapsed into a single point defect. However, once again, the satellite defect was found to be unstable once the external field is removed and the defect expands into a small disclination loop that increases in size over a few thousand time steps. Here the axis of the loop (normal to the loop) is perpendicular to the director direction (north-south). In Fig. 5.8 the defect regions are shown in intervals of  $1 \times 10^4$  time steps. One can see that the point defect initially expands to a small disclination loop. The defect ring continues to increase in

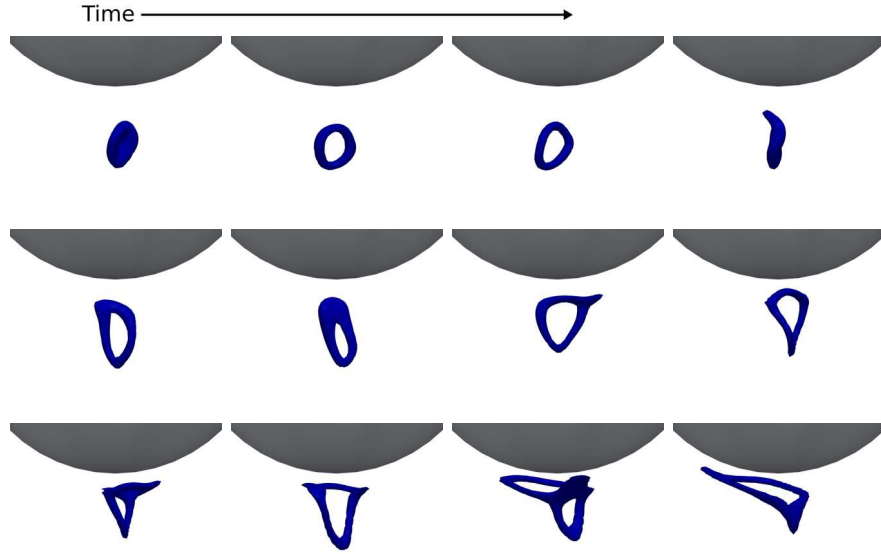
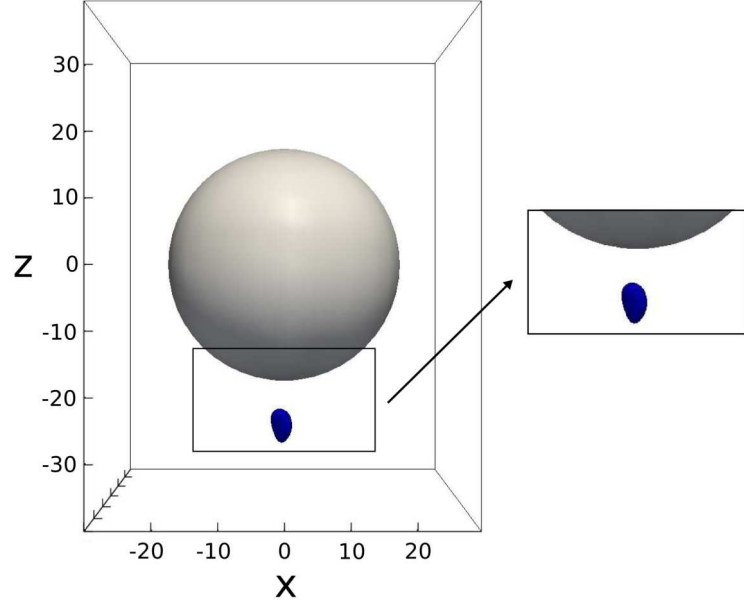


Figure 5.8: Transition from the satellite to the Saturn ring defect for system (4) with  $\kappa = 3$  and  $R_{\text{NP}} = 20\sigma_0$  in intervals of  $1 \times 10^4$ . Dark blue defect region corresponds to  $c_l < 0.1$ .

size and rotates around the axis of the director ( $z$  axis). Once the defect loop reaches a critical size a ‘kink’ was observed, where the bottom half of the loop remains in the original plane and the top half bends to follow the contours of the nanoparticle. The ‘kinked’ loop continues to rotate around the axis of the director. Quantitatively similar behaviour was observed for the transitions in previous simulations.

The simulation was repeated with a modified trial function for  $\beta$ . The trial function depends on the distance of the defect core from the centre of the nanoparticle  $a$ . For the satellite defect we used  $a = 1.46R_{\text{NP}}$  in all simulations as suggested by theoretical predictions by Shiyanovskii and Kuksenok [24]. Andrienko et al. [25] found that in molecular simulations layers of GB molecules form near the surface with large fluctuations in the local density and order. The effective radius of the nanoparticle could hence differ from the radius itself affecting the distance of the defect from the surface of the particle. This in turn affects the arbitrary function used in Equation (5.8). Hence  $a$  was reduced to  $a = 1.4R_{\text{NP}}$  in this simulation as measured in molecular simulations [25]. The elongation was set to  $\kappa = 3$  and the radius to  $R_{\text{NP}} = 20\sigma_0$ . As before, when the external field was switched off, the satellite was observed to quickly transform into a Saturn ring.

In summary, the satellite defect is neither stable nor metastable for the system and nanoparticle sizes studied here. In all four simulations the initial small disclination loop starts moving towards the equator and its radius increases. Once it is in close vicinity of the nanoparticle its shape closely follows the contours of the nanoparticle’s surface. The dynamics of the transition are in agreement with the observations made by Andrienko et al. [25]. However they found the satellite structure to be metastable for a particle radius of  $R_{\text{NP}} = 15\sigma_0$ , which we did not observe. To further investigate the satellite defect, the size of the nanoparticles should be increased, which would require a significant increase in system size to accommodate the long-range director deformations, see Fig. 5.1 (a). Due to the periodic boundaries the director is restricted along the edges of the simulation box mimicking the presence of walls. If these edges/walls are in close proximity to the nanoparticle, there can be a significant mismatch between the director field orientation induced by the nanoparticle and the surface anchoring. The mismatch can be seen in Fig. 5.1 (a) and (b): Near the edges the director field does not align with the director field at the opposite edge of the box. Therefore the simulation box size has to be sufficiently large, so that the confinement has no influence on the defect type formation. Another interesting subject of future investigations is the impact of the elastic constants. In our model the bend elastic constants are much higher than the splay and twist ones, which differs from most values obtained in experiments.



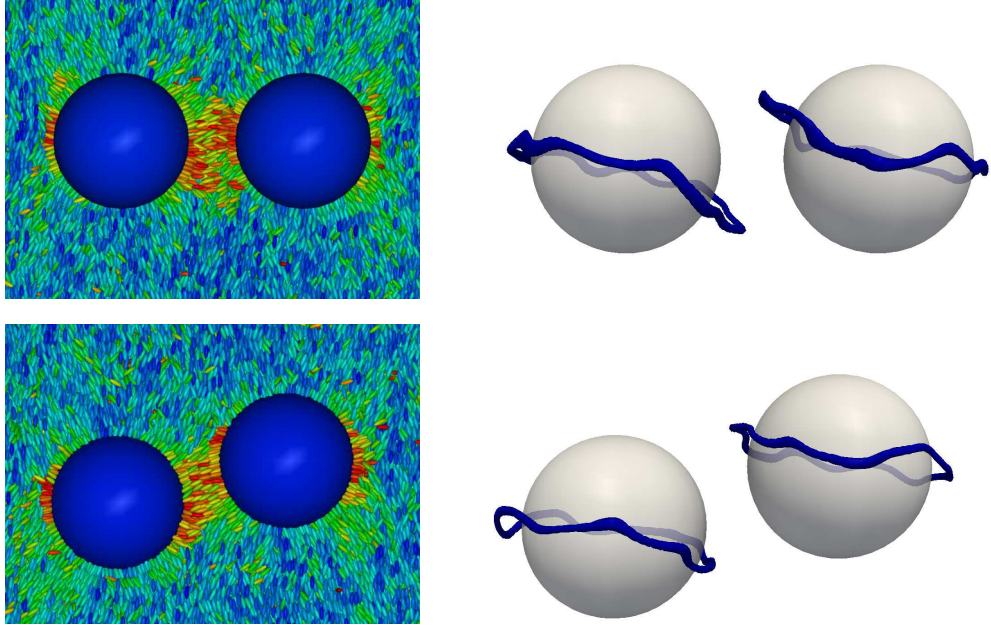


Figure 5.9: Snapshots shown for the first (top row) and last (bottom row) time step of the production run with two nanoparticles (grey) of  $R_{\text{NP}} = 15\sigma_0$  with an initial surface-to-surface distance  $10\sigma_0$ . Left column shows QMGA snapshots of the simulation. The major axes of blue liquid crystal molecules are parallel to the director and red molecules are perpendicular to it. Green indicates intermediate orientations. Right column shows the defect regions (blue) corresponding to isosurface with low uniaxial order with  $c_l < 0.12$ .

Future work should address how different ratios influence the defect formation.

### 5.3.4 Nanoparticle pair interactions

System (6) (Table 5.1) was equilibrated over  $4 \times 10^5$  time steps with two nanoparticles of radius  $R_{\text{NP}} = 15\sigma_0$  and mass  $m = 50$  separated by  $40\sigma_0$  perpendicular to the director, i.e. a surface-to-surface distance of  $10\sigma_0$ . This was followed by a production run of length  $11 \times 10^5$ , in which the nanoparticles moved freely and their positions were recorded every 2500 time steps. Fig. 5.9 shows QMGA snapshots of the first and last time step of the production run and their corresponding Westin visualisation. For the first time step the Saturn rings are strongly bent to minimise free energy. This structure is the stable configuration for two particles with fixed positions separated perpendicular to the director. Throughout the run the direction of the bend did not change. Once the particles were released, they moved towards each other and sat at an angle to each other with respect to the director. This shift allows the Saturn rings to be straight, which minimises the surrounding distortions

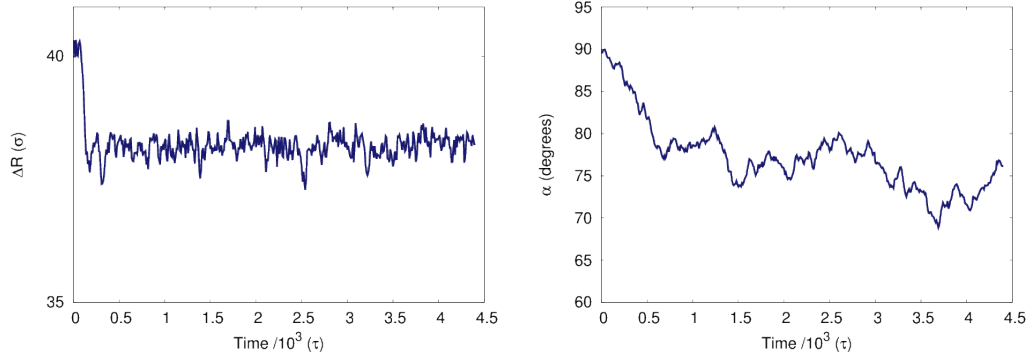


Figure 5.10: Dynamics of two nanoparticles in close proximity. Left shows separation  $\Delta R$  and right shows the angle  $\alpha$  with respect to the far field director versus time.

of the director field and hence the free energy. These observations are in agreement with mean-field Landau-de Gennes calculations [144]. To quantify the dynamics, the separation  $\Delta R$  and their angle with respect to the director  $\alpha$  are plotted over time in Fig. 5.10. After the initial approach the separation remains constant at an equilibrium value  $\Delta R = 38.17 \pm 0.22$ . This corresponds to roughly three layers of Gay-Berne molecules in between the particles as one can see in Fig. 5.9. The separation equilibrates on the order of a few hundred  $\tau$ . In contrast the angle  $\alpha$  approaches its equilibrium slowly on the order of a few thousand  $\tau$  comparable to the length of the simulation. From the simulation results we estimate  $\alpha = 75^\circ \pm 3^\circ$ . This is in reasonable agreement with observations in the Landau-de Gennes free energy framework, which showed an equilibrium angle  $\alpha = 79^\circ$  [13].

## 5.4 Conclusions

In conclusion, we have successfully simulated nanoparticle inclusions in nematic liquid crystals using molecular simulations. For particle inclusions with homeotropic anchoring the Saturn ring was observed with a defect distance  $a = 1.13R_{\text{NP}} + 0.8\sigma_0$ , which is in agreement with theoretical predictions and experimental observations. For very small particles ( $< 6\sigma_0$ ) the defect ring sits directly on the surface of the nanoparticle. For particle inclusions with planar surface anchoring the boojum defect was observed with two point defects at the top and bottom of the particle with respect to the far field director. Attempts were made to stabilise the dipolar satellite defect; however for the particle sizes investigated here, with up to  $R_{\text{NP}} = 20\sigma_0$ , it was found to be neither stable nor metastable. The structural transition from a Saturn ring to a satellite defect was reported. To further investigate this defect structure

larger system sizes ( $\gg 10 \times 10^6$ ) are necessary, which would allow the study of larger particle inclusions. Finally the pair interactions between two nanoparticle inclusions were analysed. Particles were observed to attract each other until they reached an equilibrium separation. The particles, which were surrounded by a Saturn ring each, prefer to sit at an angle with respect to the director to minimise the free energy. Such molecular simulations could be used in future investigations to study the aggregation of clusters of nanoparticles inside a nematic. In experiments dense clusters are difficult to observe in 3D and in mean-field approaches calculations get increasingly more complex with more inclusions. In contrast, in simulations a larger number of nanoparticles does not present a problem.

## Chapter 6

# Entangled defect structures around nanoparticles in nematics

### 6.1 Introduction

From theory and experiments we know that nanoparticles with homeotropic anchoring behave as quadrupoles. Even particles of several orders of magnitude larger can form a quadrupole, if confined to a thin nematic cell. [187]. For two quadrupoles in close vicinity entangled defects were found to spontaneously arise when the surrounding nematic is distorted by thermal quenching or laser beam manipulation. Here ‘entangled’ means that both particles are surrounded by a single disclination line. Using laser tweezers, which allow easy manipulation with great precision, a range of reproducible different entangled objects have been found [39, 43, 105, 128, 144, 188, 189]. Namely the three different structures are the figure of eight, the figure of omega and the figure of theta. Micrographs of these entangled defect structures produced by Tkalec and Muševič [5] are shown in Fig. 6.1. For the figure of eight defect a single strength  $-1/2$  disclination line winds around the particles forming a figure of eight ( $\infty$ ). The figure of omega consists of one disclination line that surrounds both particles near the equator with respect to the director. The disclination line escapes into the space in between the particles where it shapes like the Greek letter omega  $\Omega$ . Note the spontaneous symmetry breaking with both these defect structures being chiral. The two states are degenerate and hence left-handed and right-handed structures occur with the same frequency. The only non-chiral entangled defect observed is the figure of theta ( $\Theta$ ), which consists of

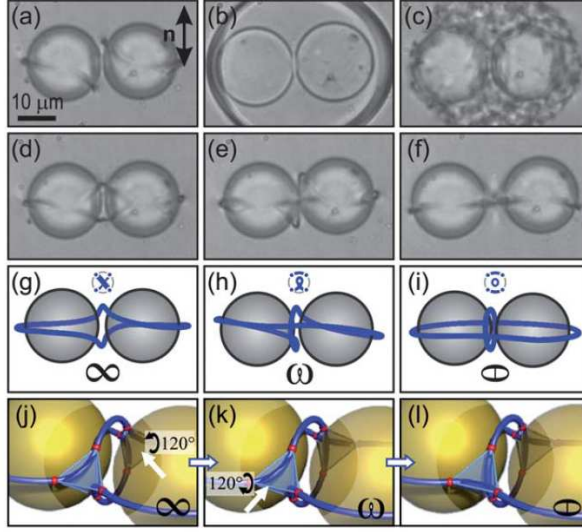


Figure 6.1: Micrographs of particles in a nematic entangled by disclination lines and their respective schematic: (a-c) Micrographs of the initial quenching process with a laser and the equilibration phase. (d,g,j) Figure of eight, (e,h,k) figure of omega, (f,i,l) figure of theta. Reproduced from Ref. [5] with permission from The Royal Society of Chemistry.

a disclination line surrounding both particles and an additional second defect loop in the plane in between the particles. The smaller ring in fact is a -1 hyperbolic point defect with an escaped core. These entangled defects were observed in experiments and predicted numerically using phenomenological mean-field calculations based on Landau-de Gennes free energy minimisation [13, 144]. Interestingly, the figure of omega and figure of theta were predicted by Landau-de Gennes free energy minimisation first and were later observed in experiments [188].

In experiments with micron-sized particles in strong confinement two separate quadrupoles are the only stable structure. They were observed in 48% of all laser tweezers manipulations. For entangled structures the figure of eight was found most frequently (36%), followed by the figure of omega (13%). The figure of theta was observed rarely (3%) [188]. All three entangled structures were found to be metastable with a free energy  $\sim 1\%$  higher than the energy of two well-separated particles each surrounded by a Saturn ring [188]. The binding energy for entangled pairs of particles was calculated to be an order of magnitude stronger than the unbound pair and several thousand times stronger than particles dispersed in water [188].

Čopar and Žumer [189] showed that the director field of these entangled

defects only differs in the region where the lines initially cross, see in Fig. 6.1 (j-l). Theoretically, by rotating the tetrahedron shown, one entangled state can be transformed into another. In practice, this is equivalent to cutting and reconnecting the disclination lines. In experiments, this rewiring is achieved by locally applying laser tweezers to heat the region of the tetrahedron. An interesting question arises: two particles with homeotropic anchoring have a topological charge  $q = +2$ . Hence a single disclination line entangling both particles must have a topological charge of  $q = -2$ . Čopar and Žumer [189] explained this by considering the three fold symmetry of the disclination line. Rather than a simple line, a disclination line should be thought of as a ribbon. The ribbon is defined by the centre of the defect core and a curve that follows the orientation of the director field in the cross section of the disclination. The amount of twist of the ribbon around its own axis can be described by a self-linking number  $sl$ . One can write a generalised conservation of topological charge  $q$  including  $sl$  and the linking number  $lk$  for loops  $A_i$  [189]

$$\frac{3}{2} \left[ \left( \sum_i^n sl(A_i) + 2 \sum_{i>j}^n lk(A_i, A_j) \right) \right] + n = q \pmod{2}. \quad (6.1)$$

Čopar and Žumer [189] showed that the figure of theta has  $sl = 0$ , whereas the figure of eight and the figure of omega show  $sl = \pm \frac{2}{3}$ .

The system of two entangled particles can be thought of as a building block for more complex systems. For example a one-dimensional chain of particle was found to be entangled by defect lines. Here the disclination line winds around all the particles: a chiral sequence of figure of eight as well as a non-chiral series of figures of theta were observed in experiments [188]. Theoretically the assembly of two-dimensional colloidal crystals was predicted [190, 191]. However in experiments this was found to be somewhat more challenging. Only in chiral nematic cells particles were found to spontaneously aggregate in 2D [192]. Here the chirality allows easier interlinking of defect loops, because the director can point out of plane.

Nikkhou et al. [193] recently showed that entangled defect structures can also be observed around a microsphere and a microfibre in a nematic liquid crystal in experiments. Note that a fibre is topologically equivalent to a sphere. By locally heating the LC surrounding the fibre an arbitrary number of pairs of ring defects can be created with opposite charges and winding numbers [194]. When a microsphere is brought into close vicinity of the  $-1/2$  ring defect on the fibre, entanglement was observed. The probability of creating a figure of eight was highest (57%), followed by the figure of theta (42%). The figure of omega was unstable and observed rarely

(1%) [193].

When bringing many particles into close vicinity and applying laser tweezers, knotted structures can be created [192, 195, 196]. Here several disclination lines are knotted showing a variety of different knots: Trefoil knot, Solomon link, Pentafoil knot and the Star of David. As before, this can be modified by locally applying laser tweezers, which corresponds to a rotation of the tetrahedron. By applying the laser tweezers in unknotted regions, additional knots can be created and vice versa.

The systems can be manipulated not only by the use of laser tweezers, but also by using strong local electric fields, hydrodynamic flow, temperature changes and the use of different boundary conditions and confined geometries. This allows to create and modify defects in liquid crystals in a rather controllable way and by tuning these parameters a variety of complex systems can be designed. For example, Wood et al. [197] show that liquid crystals with a high number of colloidal inclusions can be used to synthesise a soft solid with high rigidity. The rigidity is caused by the particle entanglement in the network of defect lines. These materials have important features for the potential use in biosensors [198].

Molecular studies of two quadrupoles in close vicinity showed a three ring structure for particle inclusions of nanometre size [39, 41, 105]. This structure is similar to the figure of  $\Theta$ ; however the inner loop connects with the outer loop at two nodes. Two possible explanations have been proposed to why the structure differs from the ones observed in experiments. In earlier studies it was declared as a transient state, before it reaches the final entangled structure [128]. Later studies proposed that the size of the particles is crucial and that the three ring structure appears for particles of nanometre scale, whereas micron-sized particles form the three different entangled defects ( $\infty$ ,  $\Theta$  and  $\Omega$ ). In this chapter we study entangled defect structures around nanoparticles and analyse how they rearrange from one configuration to another. Furthermore we propose an explanation for the three ring structure.

## 6.2 Model and simulation details

Five different systems were studied with particle radii of  $10\sigma_0$ ,  $15\sigma_0$  and  $20\sigma_0$  and several different particle separations. Simulation details are given in the following subsections.

### Nanoparticles of radius $R_{\text{NP}} = 10\sigma_0$

To simulate the nematic host the GB(3, 5, 1, 3) variation of the Gay-Berne potential was used with a cutoff of  $5\sigma_0$ . The initial director orientation was chosen along the  $z$  direction. Two spherical particle inclusion of radius  $R_{\text{NP}} = 10\sigma_0$  were placed in the box interacting via a purely repulsive LJ potential (see Section 5.2) with a cutoff of  $(R_{\text{NP}} + 1)\sigma_0$ . Throughout the simulation their position was fixed. The system was simulated for particles separated along  $x$  with a surface-to-surface separation of  $\Delta = 2.94\sigma_0$  as well as  $\Delta = 10.3\sigma_0$ . The temperature was set to  $T = 3.0$  leading to a bulk density of  $\rho \sim 0.3$  in the cubic simulation box of length  $\sim 120\sigma_0$ . The system was equilibrated over  $1.6 \times 10^6$  time steps using an  $NpT$  ensemble, followed by a production run ( $NpT$  ensemble) of  $2.5 \times 10^5$  time steps with a time step  $\Delta t = 0.004$ . Molecular positions and orientations were stored every 500 time steps. The total number of GB molecules was 512 000. Their moment of inertia was set to  $I = 0.5$  and their mass to unity.

### Nanoparticles of radius $R_{\text{NP}} = 15\sigma_0$

The simulation was repeated with particles of size  $R_{\text{NP}} = 15\sigma_0$  separated along  $x$  from surface-to-surface by  $\Delta = 5\sigma_0$  as well as  $\Delta = 10\sigma_0$ . Other simulation details were unchanged. Two modifications were made to reduce computational cost. The simulation box length  $L_x$  was reduced to  $2R_{\text{NP}} + \Delta$  and one nanoparticle was placed at  $(-L_x, 0, 0)$ . With periodic boundaries along  $x$  (and  $y$ ) this represents an infinite chain of nanoparticles along the  $x$  direction. This allows to reduce the total number of Gay-Berne molecules by over 50%, with  $N = 182\,000$  for  $\Delta = 5$  and  $N = 210\,000$  for  $\Delta = 10$ . Furthermore walls were introduced at the  $z$  boundaries using a simple Lennard-Jones 12-6 potential with  $\epsilon = \sigma = 1$  and a potential cutoff of  $2.5\sigma_0$ . This has the advantage that  $L_z$  can be chosen to be smaller than, for example, in the system described above without the danger of long-range interactions across the boundaries. The length was chosen sufficiently long to accommodate for the density and order parameter fluctuations near the walls ensuring bulk behaviour in the centre of the simulation box. The simulation box dimensions were  $\sim (35 \times 136 \times 136)\sigma_0^3$  and  $\sim (40 \times 136 \times 136)\sigma_0^3$  for the larger separation. The bulk density for both was  $\rho \sim 0.3$  with 210 000 Gay-Berne molecules. The system was equilibrated over  $7.5 \times 10^5$  time steps ( $\Delta t = 0.004$ ) using an  $NVT$  ensemble, followed by a production run ( $NVT$  ensemble) of  $4 \times 10^5$  time steps. Molecular positions and orientations were stored every 500 time steps.



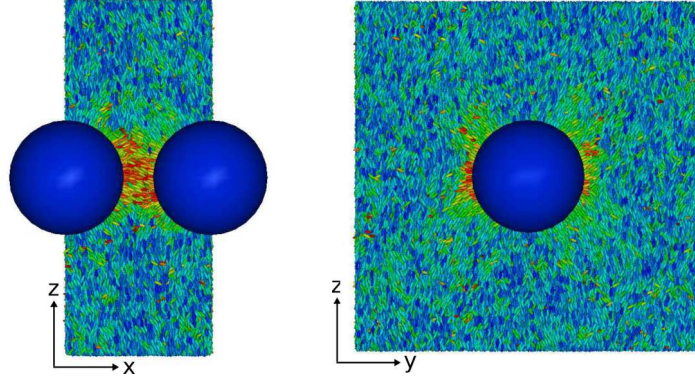


Figure 6.2: QMGA snapshot of the setup from two different angles. The nanoparticle and one of its images are coloured blue. Liquid crystal molecules are colour coded depending on their orientation. Blue molecules are parallel to the director and red molecules are perpendicular to it and green indicates intermediate angles.

### Nanoparticles of radius $R_{\text{NP}} = 20\sigma_0$

In this simulation the nanoparticles' radii was increased to  $R_{\text{NP}} = 20\sigma_0$ . Other system parameters were chosen as for the system with  $R_{\text{NP}} = 15\sigma_0$ . No wall potential was applied and instead periodic boundaries were used across  $z$ . The total number of Gay-Berne molecules was 214 000 with a moment of inertia of  $I = 2.5$ . The box dimension was chosen to be  $\sim(50 \times 120 \times 120)\sigma_0^3$ ; hence the separation between neighbouring nanoparticles was  $\Delta = 10\sigma_0$ . QMGA snapshots of the setup are shown in Fig. 6.2. This system was equilibrated over  $8 \times 10^5$  time steps ( $\Delta t = 0.004$ ) using an  $NVT$  ensemble, followed by a production run ( $NVE$  ensemble) of  $6.5 \times 10^5$  time steps. Molecular positions and orientations were stored every 500 time steps.

## 6.3 Data analysis and results

To analyse the defect structures formed around the nanoparticles, the Westin metrics were calculated on a regular 3D grid with a spacing of  $0.25\sigma_0$  and regions of low uniaxial order corresponding to  $c_l < 0.05$  were determined. Five different structures were observed: two separate Saturn rings, figure of eight, figure of omega, figure of theta as well as a structure that resembles the three ring figure with one node. For each of these structures a typical example is shown in Fig. 6.3. The only non-entangled structure found was two nanoparticles surrounded by a Saturn ring each shown in Fig. 6.3 (a). The Saturn rings are strongly bent away from each other to minimise the distortion of the director field, which minimises free energy. The

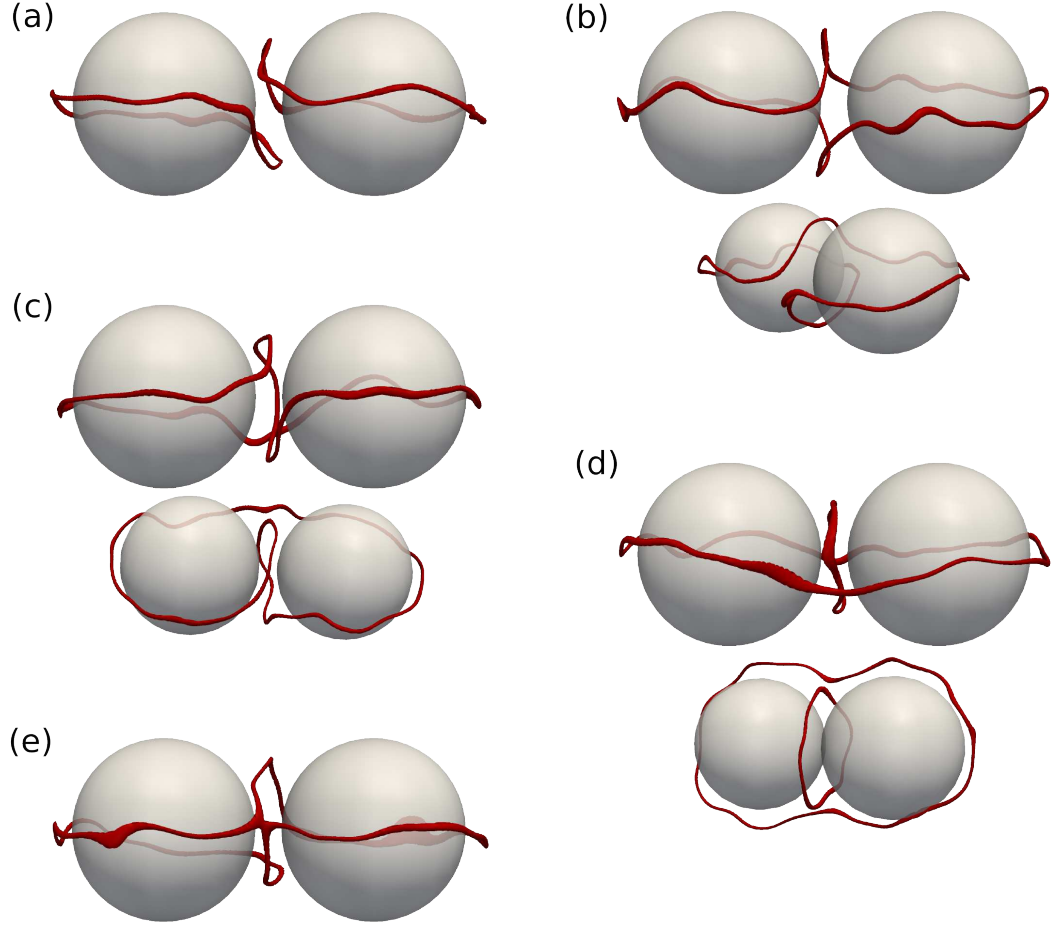


Figure 6.3: Defect structures observed for two nanoparticles of radius  $R_{\text{NP}} = 10\sigma_0$  in close proximity ( $\Delta = 2.94\sigma_0$ ). Some are shown from two angles for clarity. (a) two separate Saturn rings, (b) figure of eight, (c) figure of omega, (d) figure of theta and (e) three ring defect with one node.

bending effect was also observed for Landau-de Gennes free energy minimisations [199]. Fig. 6.3 (b-d) show typical snapshots of the figure of eight, the figure of omega and the figure of theta from two different angles. The shape of the defect line is in good agreement with the observations for micron-sized particles in experiments. Fig. 6.3 (e) shows an intermediate structure, where two segments of the disclination line are linked. To rearrange from one entangled structure to another the linked structure has to form. We expect this phase to be high in energy for micron-sized particles and hence it cannot be observed on real timescales. Since we avoided time averaging thermal fluctuations of the disclinations are visible. With the exception of the intermediate defect structure all other defect structures were also observed in experiments and using Landau-de Gennes minimisation for micron-sized particles [199].

To calculate the frequencies with which the five structures occur and to gain a better understanding of the dynamics of the system the defect structure was determined for each system snapshot. Especially interesting is how defects rearrange from one configuration to another. Due to the high number of snapshots this process was automated and the defects classified as follows.

- All grid points of the defect core corresponding to  $c_l < 0.05$  were identified and stored. Note that we did not distinguish between different values of  $c_l$  and hence only the positions were stored. All data points with values above the threshold were ignored.
- To identify data points that belong to the same disclination line, the flood fill algorithm was used: An arbitrary starting point is chosen and added to an empty list. In the next step all neighbours of this starting point were added to the list, whereas the starting point itself was removed. Note that only defect regions were stored, hence there might not be a neighbour in all six directions. The process was repeated, by adding all neighbours of all particles inside the list to the list and by removing the points itself, until the list is empty. All points removed form a continuous object.
- Since disclination lines can only exist in the form of closed loops (or lines across periodic boundaries), each defect line was checked for this criterion.
- For each disclination line the length was approximated using a ‘sphere-tracking’ algorithm. This is particularly interesting, because the energy associated with the disclination line is proportional to its length. Firstly, two arbitrary starting points were chosen, that were close to each other. We defined the unit

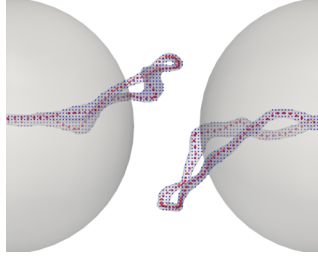


Figure 6.4: Disclination lines around two nanoparticles (grey). Blue dots correspond to data points with  $c_l$  below the threshold and red points correspond to points calculated using the ‘sphere-tracking’ (see text).

vector connecting these points as our direction of travel. For each step we moved a short distance along the direction of travel. At the new point the average position of the defect line was calculated by averaging the positions of the nearest 10 neighbours. This method proved itself as very accurate and reliable. The process is finished once the initial starting point is reached. The length was estimated by adding the distances between neighbouring averaged positions. In Fig. 6.4 the red points indicated the average positions calculated using this method for an example snapshot.

- To accurately distinguish between the different defect types the connections between the red regions in Fig. 6.5 were evaluated using the flood fill algorithm. Here the boundaries were treated as fixed. The connections in conjunction with the number of disclinations and their respective length allow to determine the defect structure. For the figure of eight we further distinguished the direction of the twist, depending on which path crosses on top of the other one. In over 99.9% of the snapshots this automated analysis was conclusive. Exceptions were inspected visually.

The different defect structures over time are plotted for all five simulations in Figs. 6.6–6.10. For nanoparticles with radius  $R_{\text{NP}} = 10\sigma_0$  the defect transitions frequently between different structures. No structure persists for more than  $\sim 250\tau$  ( $\sim 62\,500$  time steps). It appears, at least for the time simulated, that two separate Saturn rings are the most frequent structure. The figure of eight can be seen occasionally, whereas the figure of theta and omega are very rare. The exact frequencies are given in Table 6.1 for all five simulations. The intermediate structure with one node formed frequently. This is interesting as this structure is not observed in experiments suggesting it is unstable. This suggests that the particle size does indeed

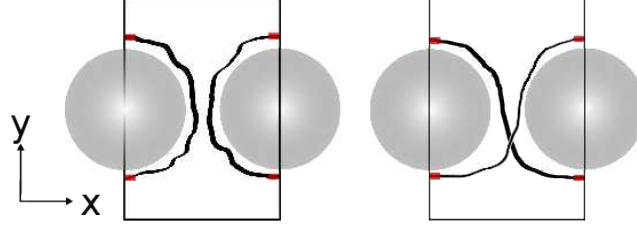


Figure 6.5: Schematic of two nanoparticles (grey) and the surrounding disclination lines (black) in the  $x$ - $y$  plane. Red regions show the starting areas for the flood fill to distinguish different defect structures. Depending on which red regions are connected the defect type was determined.

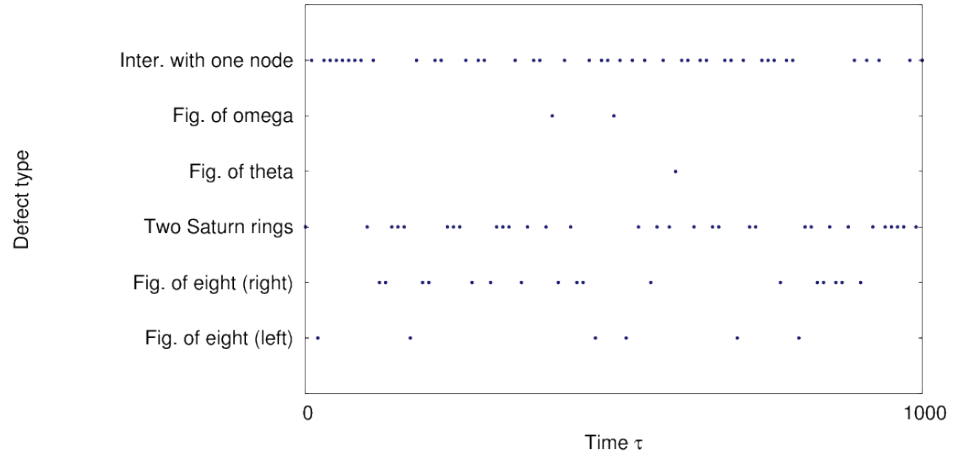


Figure 6.6: Defect structure versus time for  $R_{\text{NP}} = 10\sigma_0$  and a surface-to-surface separation  $\Delta = 2.94\sigma_0$ .

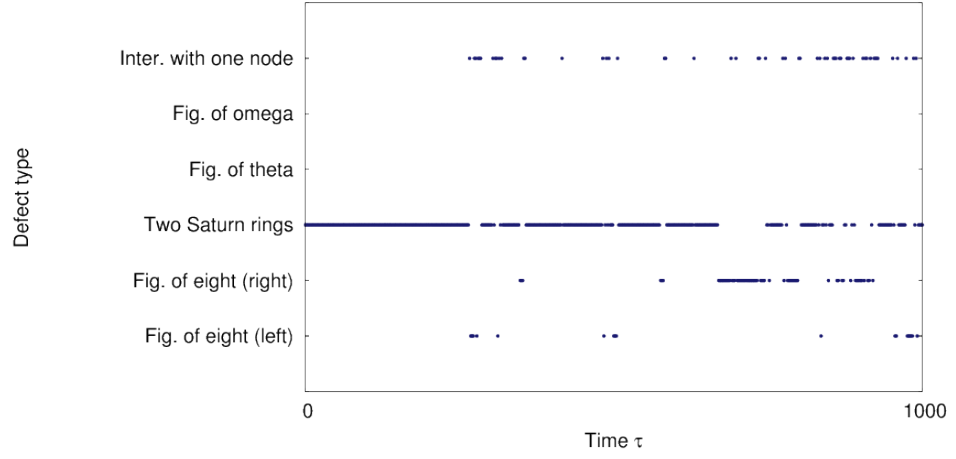


Figure 6.7: Defect structure versus time for  $R_{NP} = 10\sigma_0$  and a surface-to-surface separation  $\Delta = 10.3\sigma_0$ .

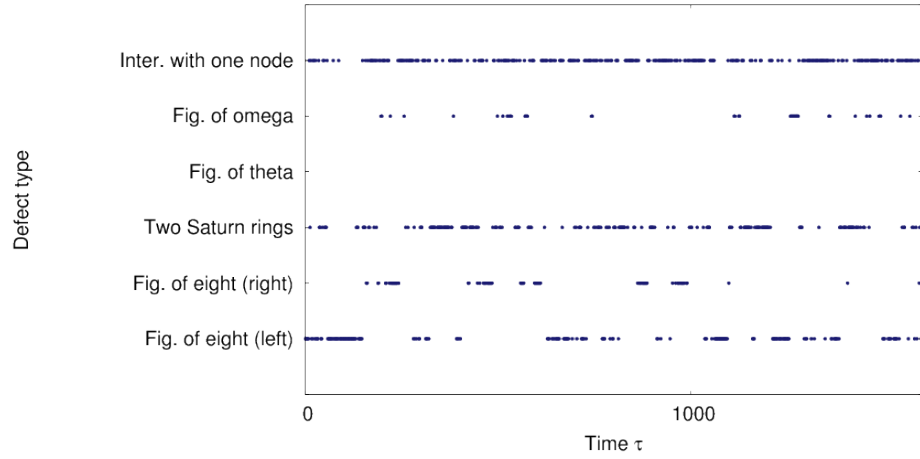


Figure 6.8: Defect structure versus time for  $R_{NP} = 15\sigma_0$  and a surface-to-surface separation  $\Delta = 5\sigma_0$ .

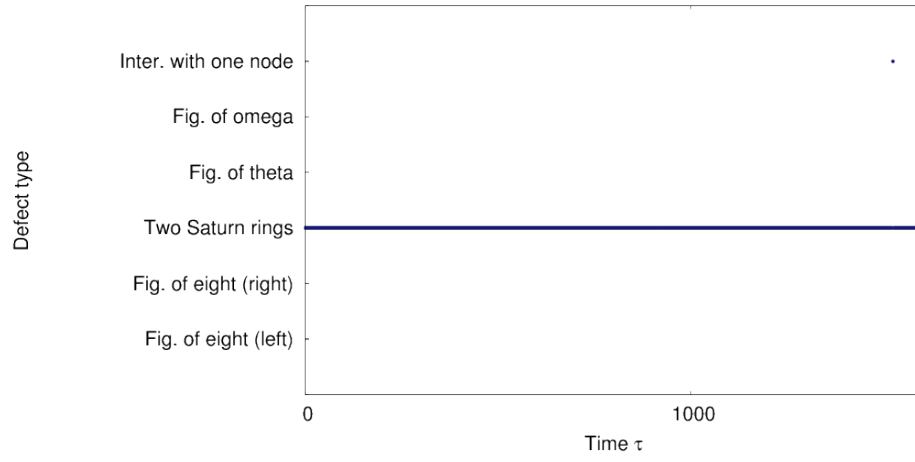


Figure 6.9: Defect structure versus time for  $R_{\text{NP}} = 15\sigma_0$  and a surface-to-surface separation  $\Delta = 10\sigma_0$ .

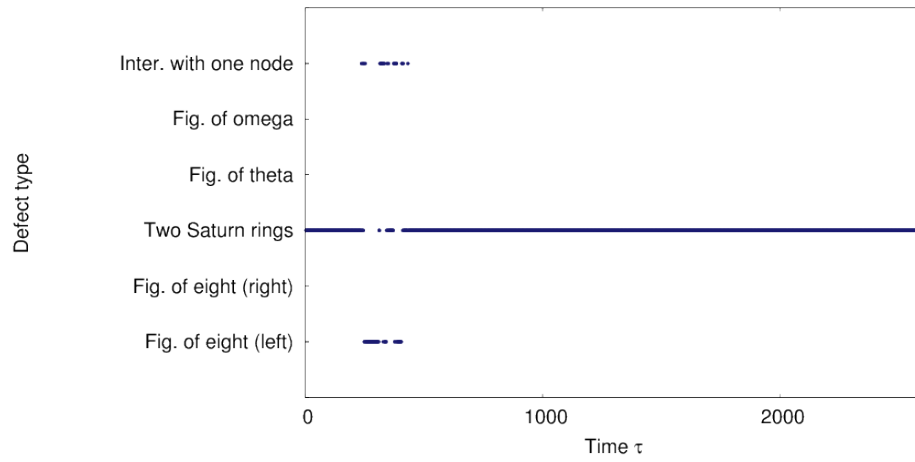


Figure 6.10: Defect structure versus time for  $R_{\text{NP}} = 20$  and a surface-to-surface separation  $\Delta = 10\sigma_0$ .

have a significant impact on the entanglement. For particles with radius  $R_{\text{NP}} = 15\sigma_0$  and a surface-to-surface separation of  $\Delta = 5\sigma_0$  the defect structures formed and the frequency of transitions are very similar to the ones for smaller particles. With the separation increased to  $\Delta = 10\sigma_0$  no transitions were observed throughout the production run and the only structure seen was the two separate Saturn rings. For particles with radius  $R_{\text{NP}} = 20\sigma_0$  and a surface-to-surface separation of  $\Delta = 10\sigma_0$  two Saturn rings were observed most frequently. For  $\sim 150\tau$  the figure of eight with a right-hand twist forms.

Table 6.1: Frequency of observations of different entangled defect structures for a different particle radii and separations given in %.  $R_{\text{NP}}$  and  $\Delta$  are the particle radii and their surface-to-surface separation respectively.  $\infty_{\text{left}}$  and  $\infty_{\text{right}}$  correspond to the figure of eight with left- and right-handed twist respectively. ‘Saturn rings’, ‘Fig.  $\Theta$ ’ and ‘Fig.  $\omega$ ’ correspond to two well-separated Saturn rings, the figure of theta and the figure of omega. ‘Linked one node’ includes all structures where separate line segments of the disclination were connect forming a three ring structure with one node.

$\Delta(\sigma_0)$	$\infty_{\text{left}}$	$\infty_{\text{right}}$	Saturn rings	Fig. $\Theta$	Fig. $\omega$	Linked one node
$R_{\text{NP}} = 10\sigma$						
2.94	5.9	16.8	31.7	1.0	2.0	42.6
10.30	3.6	13.4	71.9	0.0	0.0	11.2
$R_{\text{NP}} = 15\sigma$						
5.0	22.2	9.0	24.3	0.0	5.2	39.2
10.0	0.0	0.0	99.88	0.0	0.0	0.12
$R_{\text{NP}} = 20\sigma$						
10.0	3.6	0.0	94.5	0.0	0.0	1.8

The results suggest that the entanglement for nanoparticles of sizes studied here are too small to observe stable entangled defects and that they frequently transition between different states and often intermediate structures are formed that we expected to be highly unstable. Future work should address larger particle inclusions to generate more stable defect structures. This could be possible using the simulation box of a infinitely long chain to reduce the total number of particles as described earlier. The question remains whether a molecular simulation could access the longer length scales necessary to observe stable entangled defects.

We tried to analyse the relation between the length of the disclination line and the occurrence of a transition and the state the defect structure is in. However



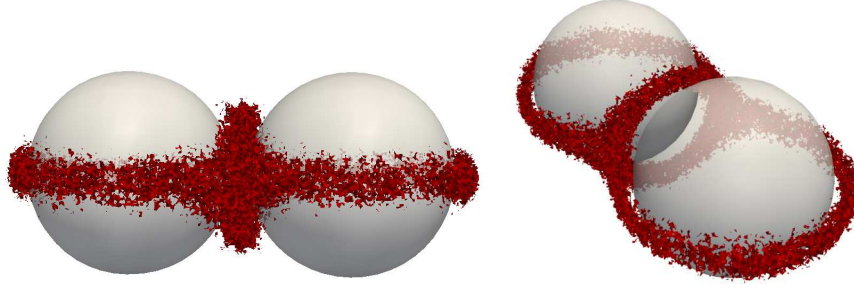


Figure 6.11: Disclination line (red) corresponding to  $S < 0.4$  time-averaged over entire production run for  $R_{\text{NP}} = 10\sigma_0$  and  $\Delta = 2.94\sigma_0$

we found no significant relation. This is partially due to the high fluctuations in length, where the line stretched or shrank by a few  $\sigma_0$  within 500 time steps and also due to the inaccuracy of the measurement that only provides estimates within  $\pm 5\sigma_0$ . Nonetheless it would be an interesting feature to study more stable entangled defects.

Finally we address the three ring structure that was observed in previous molecular simulations [39, 41, 105]. In Fig. 6.11 the isosurface corresponding to  $S < 0.4$  was plotted for the time-averaged results for the entire production run for  $R_{\text{NP}} = 10\sigma_0$  and  $\Delta = 2.94\sigma_0$ . The time-averaged disclination line forms the three ring structure with two nodes previously observed. It appears that it is a product of the frequent transitions and not a stable defect structure itself. For none of our simulations did we observe such structure with two nodes form. Furthermore the visualisation technique here is important: the common approach using small bins is inadequate to capture the fast fluctuations. Using a weighted order tensor including roughly 30 neighbouring molecules with a spacing of  $0.25\sigma_0$  has proven itself as a very accurate method to locate defect regions.

Our results are in good agreement with calculations by Araki and Tanaka [128]. In addition we have observed the figure of omega and figure of theta for the first time in molecular simulations. These structures formed very rarely.

## 6.4 Conclusions

Molecular simulations were successfully used to simulate defects around two spherical nanoparticle inclusions in close vicinity. In our exploratory simulations we studied three different radii and five different surface-to-surface separations. Five different different defect structures formed: two well-separated Saturn rings, figure

of eight, figure of omega, figure of theta and an intermediate structure with one node. These are qualitatively similar to observations made for micron-sized particles; however for the particle sizes studied here the transitions are very fast and none of the entangled structures persist for more than a few hundred time steps. This suggests that very small particles cannot be effectively bound together by entangled lines and that thermal energies are higher than the energy barriers between different entangled defect structures. To further explore this phenomenon we suggest a significant increase in nanoparticle size to possibly find more robust structures. However one has to keep in mind that this would require much longer simulation times to study transitions.

## Chapter 7

# Dynamics of a single disclination line

### 7.1 Introduction

In Chapter 5 and 6 we have shown that disclination lines play a major role in liquid crystals with particle inclusions, because the particles distort the surrounding director field inducing defects. However even in pure liquid crystalline systems disclinations arise naturally, especially near boundaries. The static properties of disclinations are well understood. More recent studies have focused on their hydrodynamic properties [200–206]: the movement of disclinations through a liquid crystalline medium, the annihilation of defect pairs, the collapse of disclination loops, the response to local distortion and thermal fluctuations. The time scales of these phenomena were shown to be governed almost entirely by the line tension associated with the disclination and the viscous drag of the medium.

In this chapter we study the fluctuation dynamics of a single disclination stabilised by an appropriate choice of boundaries. Although single disclinations are technically not observed in experiments, the separation between lines is often large enough that the surface anchoring effects, for example on the cell walls, screen the interactions between disclinations. Therefore we can think of them as separate disclinations with independent dynamics.

Mertelj and Čopič [207] recorded the equilibrium fluctuations of disclinations spanning between two glass plates and used these to estimate the line tension and viscous drag. Osterman et al. [208] used laser tweezers to stretch a disclination. From the relaxation dynamics the line tension and viscous drag were estimated. Smalyukh et al. [209] used nanoparticles and laser tweezers to pull the disclination

line. We will show in Chapter 8 that nanoparticles can become entangled by a disclination and hence we can indirectly control the movement of a disclination by moving the nanoparticle with laser tweezers. For a range of pulling forces they evaluated the equilibrium position of the particle and extracted the line tension. Theoretical descriptions of the disclination line motion were evaluated by Tóth et al. [202] as well as Svenšek and Žumer [201] based on the tensor order parameter description.

To our knowledge simulations of the dynamics of disclinations on a molecular level have received limited attention. Jose et al. [67] used a lattice Lebwohl-Lasher simulation to study the dynamics of disclinations and their interactions with nanoparticles. This is a computationally very inexpensive approach, but may suffer from inaccuracy due to the lattice site limitation.

In this study we chose an off-lattice simulation based on the soft Gay-Berne potential to stabilise a disclination. This approach complements Landau-de Gennes calculations by allowing access to smaller length scales and by omitting the one-elastic-constant approximation. Furthermore molecular simulations can reveal full information about the defect core and lets us identify possible density variations and biaxiality.

In this chapter a wedge disclination was simulated and its equilibration process and its defect core structure were analysed. Furthermore the equilibrium fluctuations and the relaxation times were measured, which provide a direct route to calculate the line tension of the defect line and the effective viscous drag.

## 7.2 Theoretical background

The elastic energy per unit length associated with a straight disclination line in the bulk can be approximated by [6]

$$\mathcal{F}_0 = \pi K s^2 \ln(r_1/r_0) + \mathcal{F}_{\text{core}} , \quad (7.1)$$

where  $K$  is the one-elastic-constant,  $s$  the strength of the disclination and  $\mathcal{F}_{\text{core}}$  the energy of the defect core.  $r_1$  and  $r_0$  are the size of the sample and the size of the defect core respectively. Here small inaccuracies in the values  $r_0$  and  $r_1$  are insignificant due to the logarithm. Note that each deformation of the disclination increases its length and hence its energy. The theoretical prediction for the effective friction coefficient of a disclination line moving slowly in a nematic was derived as [205]

$$R = \pi \gamma_1 s^2 \ln(r_1/r_0) , \quad (7.2)$$

where  $\gamma_1$  is the rotational viscosity.

The dynamics of the disclination can be described in analogy with a massless, damped, vibrating string. Here we consider a straight wedge disclination in the centre of the simulation box along  $z$  with deformations described by the displacement distance in the  $x$ - $y$ -plane  $u(z, t)$ . In addition we assume that a restoring force of strength  $\gamma$  is acting on the disclination, which effectively attracts each line segment towards the origin. By combining these forces the equation of motion can be written as

$$\Lambda \frac{\partial^2 u(z, t)}{\partial z^2} - R \frac{\partial u(z, t)}{\partial t} - \gamma u(z, t) = 0, \quad (7.3)$$

where  $\Lambda$  and  $R$  are the line tension and the viscous drag respectively. The discrete fluctuations may be expanded in Fourier components

$$\tilde{u}(k) = \frac{L_z}{N} \sum_{z=1}^N u(z) \exp(ikz), \quad (7.4)$$

where  $L_z$  is the length of the straight disclination. Substituting  $\tilde{u}(k)$  into Equation (7.3) with  $\partial^2/\partial z^2 \rightarrow -k^2$ , we obtain

$$\tilde{u}(k, t) = \tilde{u}(k, 0) \exp\left(-\frac{\gamma + \Lambda k^2}{R} t\right). \quad (7.5)$$

Hence the inverse of the decay rate  $1/\tau$

$$\frac{1}{\tau} = \frac{\gamma}{R} + \frac{\Lambda}{R} k^2 \quad (7.6)$$

is expected to be a linear function of  $k^2$  and from the gradient and intercept the ratio of line tension  $\Lambda$  and viscous drag  $R$  and the strength  $\gamma$  can be extrapolated. The decay rates can be obtained from the normalised time autocorrelation function of the Fourier components of the displacement

$$c(k, t) = \frac{\langle \tilde{u}(k, t) \tilde{u}(-k, 0) \rangle}{\langle |\tilde{u}(k)|^2 \rangle}, \quad (7.7)$$

where the angular brackets denote an ensemble average. Due to the finite-time constraint in simulations the average value was subtracted  $\tilde{u} \rightarrow \tilde{u} - \langle \tilde{u} \rangle$ .  $c(k, t)$  can be fitted to an exponential for each allowed wave vector  $k$  to extrapolate the decay rates, see Equation (7.6).

The effective Hamiltonian of the disclination is given by

$$\mathcal{F}[u] = \int dz \frac{1}{2} \gamma u(z)^2 + \frac{1}{2} \Lambda u'(z)^2. \quad (7.8)$$

Applying Parseval's theorem leads to

$$\mathcal{F} = \frac{1}{2L} \sum_k (\gamma + \Lambda k^2) |\tilde{u}(k)|^2. \quad (7.9)$$

By applying the equipartition theorem, that states that the average energy of each mode is equal to  $\frac{1}{2} k_B T$ , we can derive

$$\langle |\tilde{u}(k)|^2 \rangle = \frac{L k_B T}{\gamma + \Lambda k^2} \Leftrightarrow \frac{1}{\langle |\hat{u}(k)|^2 \rangle} = \frac{\gamma}{L k_B T} + \frac{\Lambda}{L k_B T} k^2, \quad (7.10)$$

where  $k_B$  and  $T$  are the Boltzmann's constant and temperature respectively. Hence the line tension  $\Lambda$  and the strength  $\gamma$  can be directly calculated from the gradient of the inverse square amplitude of the fluctuations versus  $k^2$ .

### 7.3 Model and simulation details

Initially a nematic mono-domain was equilibrated using 125 000 Gay-Berne molecules in a cubic box of length  $L$  with periodic boundaries. The molecules of length  $\kappa = 5$  were interacting via the purely repulsive GB potential, described in Section 2.3, with a cutoff of  $6.0\sigma_0$ . As in previous chapters, reduced units were used throughout. The mass of the molecules was set to unity and the moment of inertia to  $I = 7.0$ . Initially  $\kappa$  was set to unity with all molecules orientated along the  $z$ -axis. The molecules were slowly elongated along their major axes until they reached the desired elongation  $\kappa = 5$ . The initial director orientation remained close to the  $z$  axis. The density was chosen to be  $\rho = 0.15$  and the temperature  $T = 1.0$ . For this state point, the bulk order parameter  $\langle S \rangle \sim 0.82$ . Note that the purely repulsive GB potential is not sensitively dependent on the temperature, due to the absence of attractive forces. After the initial growth an external field is applied near the edges of the box, which supports a stable half-integer strength disclination. This potential, introduced in the next section, was implemented in GBMOLDD. The system was equilibrated over  $8 \times 10^6$  time steps with  $\Delta t = 0.002$  using a  $NVT$  ensemble. The equilibration run was followed by a  $6 \times 10^6$  time steps long production run ( $NVE$  ensemble) with snapshots of the molecular positions and orientations stored every 2500 time steps.

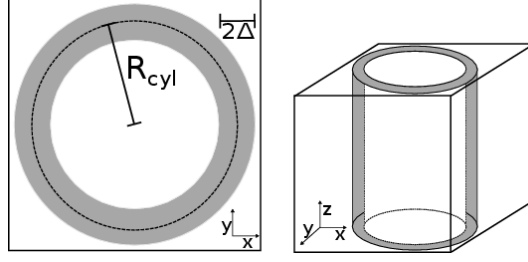


Figure 7.1: Left shows a sketch of the  $x$ - $y$  plane of the simulation box and right shows a 3D sketch of the simulation box. The field is non-zero inside the dark grey ring region and zero outside of the region. The dashed line corresponds to the virtual cylinder wall ( $R = R_{\text{cyl}}$ ), where the external field reaches its maximum. Towards the boundaries it smoothly decays to zero.

### External field to stabilise disclination line of strength $-1/2$

To stabilise a single disclination line an external field was applied near the boundaries of the simulation boxes, that favours molecules to lie in the  $x$ - $y$  plane following the ideal director field of a  $-1/2$  defect in that plane. In Fig. 7.1 the dark grey region illustrates the cylinder region, in which the external field was applied. Cylindrical polar coordinates were used with  $R$ ,  $\phi$  and  $z$  being the radial, azimuthal and height coordinate respectively. The potential reaches its maximum at the cylinder walls where  $R = R_{\text{cyl}}$  and decays smoothly to zero at the boundaries of the region  $R = R_{\text{cyl}} \pm \Delta$ . It was applied along the entire height of the simulation box.

The potential induces an energy penalty, if particles are not aligned along the theoretical director field of a  $-1/2$  defect in the  $x$ - $y$  plane. For a particle  $j$  it can be expressed as

$$U_j(R, \phi, \hat{\mathbf{u}}_j) = -f(R) [\hat{\mathbf{u}}_j \cdot \hat{\mathbf{n}}(\phi)]^2, \quad (7.11)$$

Here the energy is minimised when the orientation of a molecule  $\hat{\mathbf{u}}_j$  is parallel to the theoretical director field  $\hat{\mathbf{n}}(\phi)$ .  $f(R)$  is a strength function. The director field of a  $-1/2$  defect in the  $x$ - $y$  plane can be described by

$$\hat{\mathbf{n}}(\phi) = (\cos(-\frac{1}{2}\phi), \sin(-\frac{1}{2}\phi), 0). \quad (7.12)$$

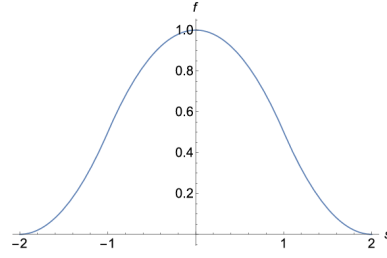


Figure 7.2: Strength function  $f$  plotted vs.  $s$ .  $s = 0$  corresponds to the virtual cylinder wall.  $s = \pm 2$  corresponds to  $R = R_{\text{cyl}} \mp \Delta$ .

The strength function  $f(R)$  was given by

$$f(R) = f_0 \begin{cases} (s+2)^2/2 & \text{if } -2 \leq s \leq -1 \\ (2-s^2)/2 & \text{if } -1 < s \leq +1 \\ (s-2)^2/2 & \text{if } +1 < s \leq +2 \\ 0 & \text{else,} \end{cases} \quad (7.13)$$

where  $s(R) = 2(R_{\text{cyl}} - R)/\Delta$ . The potential parameters were chosen to be  $f_0 = 2.0$ ,  $R_{\text{cyl}} = 40.0\sigma_0$  and  $\Delta = 7.0\sigma_0$  and hence  $R_{\text{cyl}} + \Delta = 47\sigma_0$ , which is slightly smaller than half the box length. For these parameters we observed the intended disclination line of strength  $-1/2$  as we will show later. We expect that for other parameters, system sizes or elastic constants a defect escaped into the third dimension could be observed, where the centre molecules align along the  $z$  axis [210]. Note that the external field effectively acts as a restoring force on the disclination line attracting it towards the centre.

## 7.4 Data analysis and results

In Fig. 7.3 the dynamics of the formation of the disclination line are shown in the two dimensional cross-section of the simulation box in the  $x$ - $y$  plane. The colour coding of the molecules is based on the azimuthal coordinate  $\phi$ . One can see that initially the molecules were orientated along  $z$  (out of the plane). Near the virtual cylinder walls the molecules slowly started to rotate into the  $x$ - $y$  plane and their averaged orientations followed the director field determined by Equation (7.12). The change in orientation propagated throughout the entire system due to the nematic elasticity until the average orientation of the molecules was in the  $x$ - $y$  plane. Several molecules near the centre of the simulation box are frustrated and have no preferred



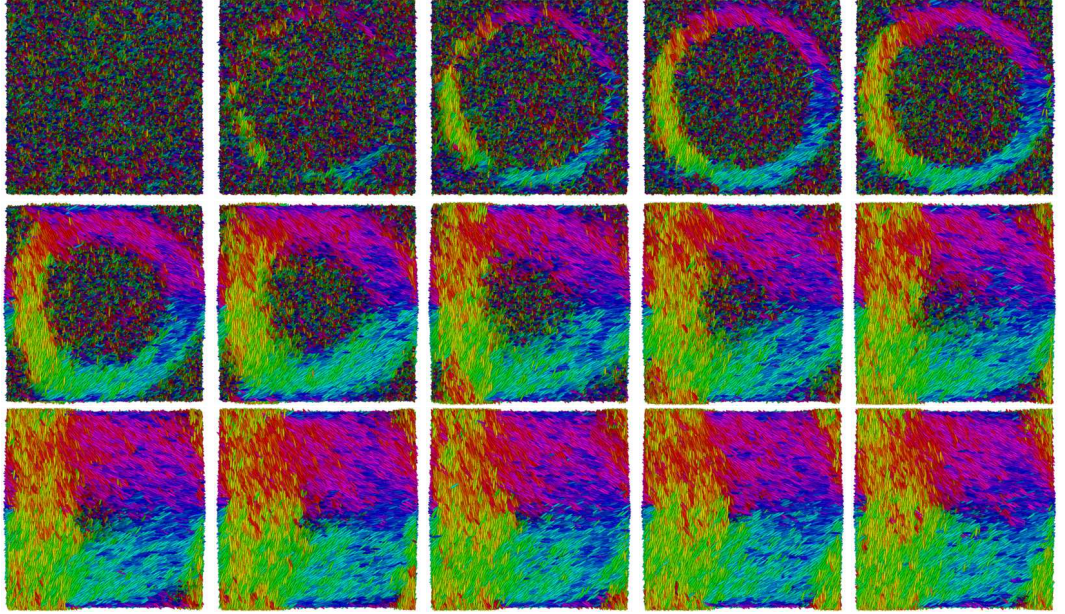


Figure 7.3: Two dimensional cross-section of the simulation box in the  $x$ - $y$  plane. The colour coding is chosen depending on the azimuthal coordinate  $\phi$ . The top row shows a snapshot for the first time step, followed by time steps in intervals of  $1 \times 10^4$ . The bottom two rows show consecutive time steps in intervals of  $1 \times 10^5$ .

orientation. This region corresponds to the cross-section of the disclination.

For all system snapshots shown in Fig. 7.3 the Westin metrics were calculated with a grid spacing of 0.5 and a kernel radius  $r_k = 7.3$ . Regions of low uniaxial order corresponding to  $c_l < 0.12$  are visualised in 3D in Fig. 7.4. Initially a zoo of defect lines forms in the regions where the external field is applied. These shrink over time and smaller loops vanish entirely. Very similar networks of disclinations can be seen in experiments in regions where laser tweezers were applied. After  $\sim 1000\tau$  a single defect line has stabilised at the centre of the simulation box surrounded by a defect-free nematic phase. Some defects are observed near the edges of the boundary box. In Fig. 7.5 the total number of Westin grid points with  $c_l < 0.12$  are plotted as a function of time. Here the number of defect regions  $N$  is expected to be proportional to the total length of disclinations in the system. Initially  $N$  decreases, following an exponential decay, until it plateaus to its final equilibrium value. The final value corresponds to the single disclination in the centre and the defects seen near the edges. Note that the number  $N$  itself has no physical meaning and depends on both the chosen spacing and the threshold for  $c_l$ . Similar relaxation behaviours were observed in experiments for the annihilation of defect loops [204] and annihilation of pairs of disclinations [203].

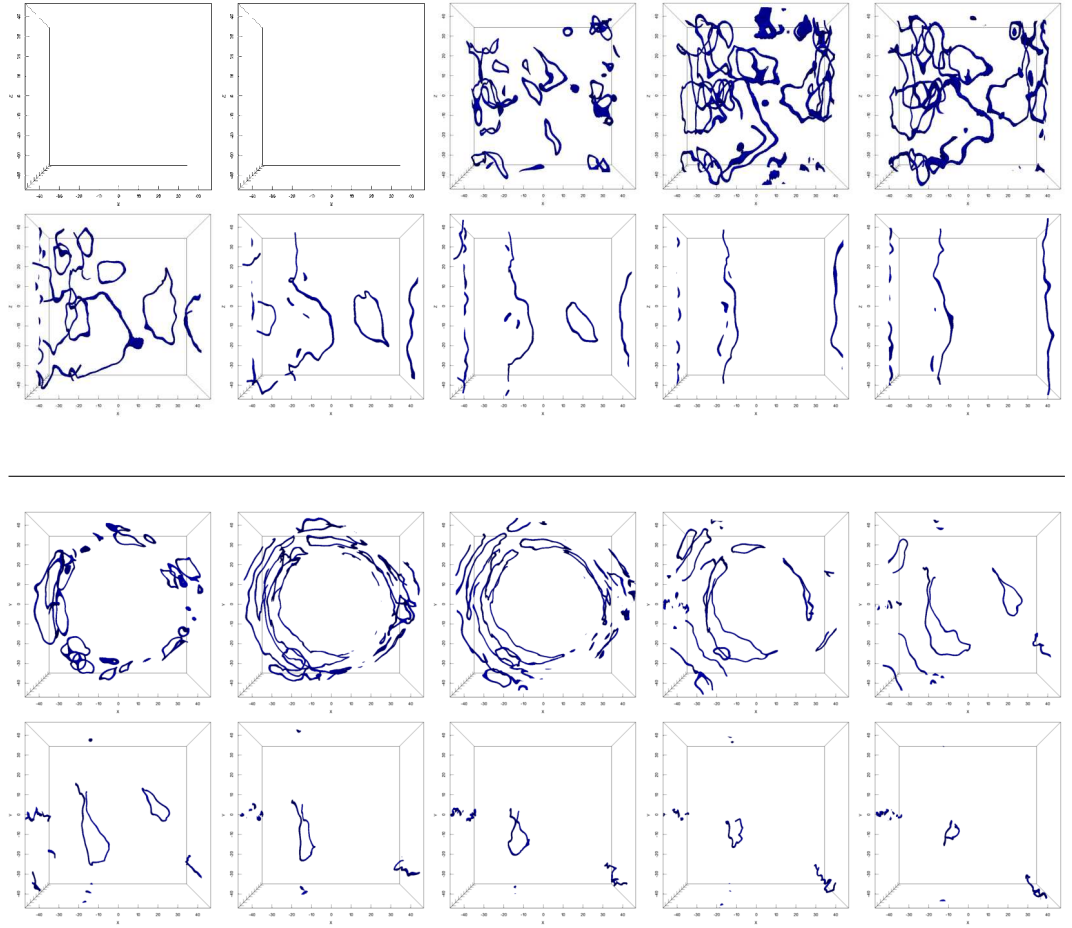


Figure 7.4: 3D visualisation of disclination lines for the system snapshots of Fig. 7.3. The defect regions correspond to low uniaxial order with  $c_l < 0.12$ . The intervals are chosen as in Fig. 7.3. Note only the first ten time steps are shown, for which the changes are most prominent. The top two rows show the side view of the simulation box and the bottom two rows show the corresponding view from the top.

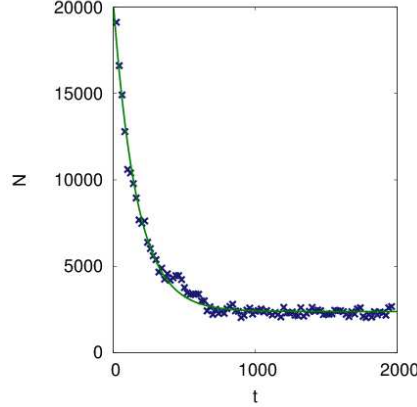


Figure 7.5: Number of Westin grid points with  $c_l < 0.12$  versus time throughout the equilibration of the single disclination. The external field was switched on at  $t = 0$ . The green line corresponds to a vertically shifted exponential fit.

In Fig. 7.6 order parameter, biaxiality, director field and density maps are shown for the 2D cross-section of the disclination line. The maps were obtained by time-averaging over  $1 \times 10^6$  time steps with cubic bins of length  $0.8\sigma_0$ . Inside the defect core region the order parameter drops significantly and simultaneously the biaxiality increases, see Fig. 7.6 (a) and (b) respectively. This is in agreement with calculations in the Landau-de Gennes framework [179] and molecular simulations [21]. Fig. 7.6 (c) shows that the local director field clearly follows a defect structure of strength  $-1/2$  as intended by the external field. It is noticeable that the order parameter and the density are higher in the regions, where the external field is applied, than inside the bulk. Outside the regions the order and density quickly decay to their bulk equilibrium value.

The study of the equilibrium fluctuations of the disclination divides into several parts. Firstly, the Westin metrics were calculated on a regular grid with a kernel radius  $r_k = 7.3$ . The grid spacing was chosen to be  $\sim 0.5\sigma_0$  leading to exactly 188 points along  $z$  between the periodic boundaries. For the  $x$  and  $y$  direction the Westin metrics were calculated for  $-20\sigma_0 \leq x, y \leq 20\sigma_0$  corresponding to 80 data points each. We consider all points with  $c_l < 0.12$  to belong to the disclination. For each  $z$  grid point, the displacement  $u(z, t)$  was calculated by averaging all  $x$  and  $y$  coordinates. We tried to resolve fluctuations in the  $x$  and  $y$  direction separately; however these were degenerate and hence we combined them to improve statistics. In Fig. 7.7 the disclination line is shown for snapshots in  $1 \times 10^6$  time step intervals. By visual inspection one can already see that the fluctuations are highly correlated

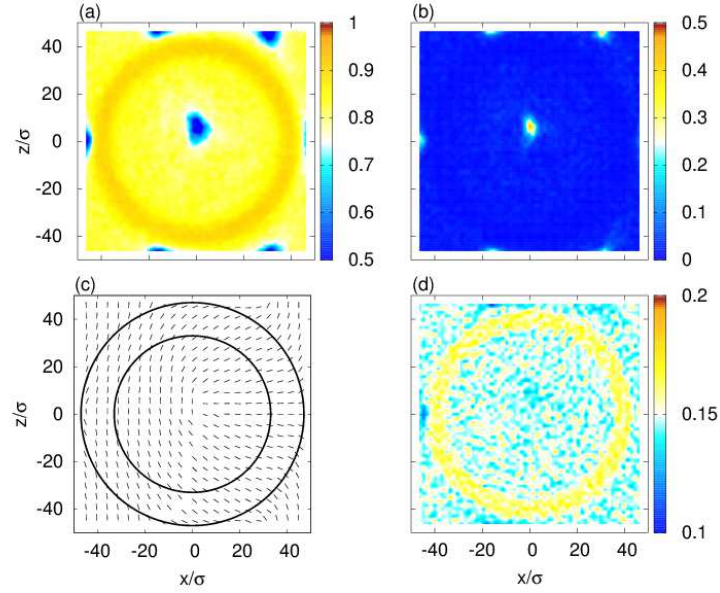


Figure 7.6: Two-dimensional cross-section of the disclination line in the  $x$ - $y$  plane. Data was time averaged over  $1 \times 10^6$  time steps with a bin size of  $0.8\sigma_0$ . Maps show (a) order parameter  $S$ , (b) biaxiality  $\alpha$ , (c) director field  $\hat{n}$  (Black lines corresponding to  $R_{\text{cyl}} \pm \Delta$ .) and (d) density.

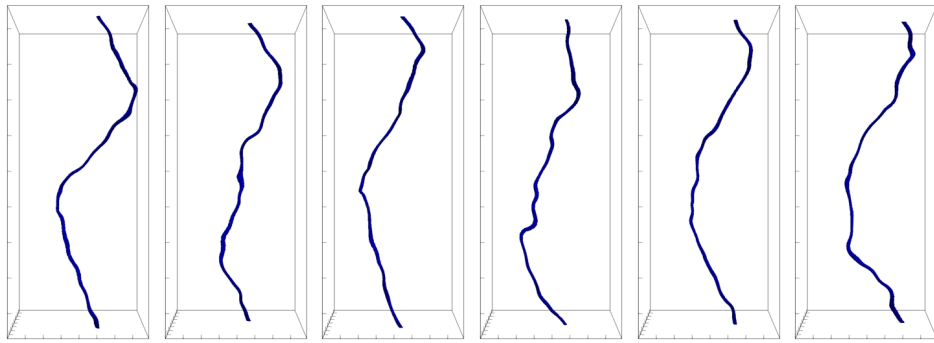


Figure 7.7: Visualisation of the defect line at intervals of  $1 \times 10^6$ . Isosurfaces shown correspond to Westin metrics  $c_l < 0.12$ .

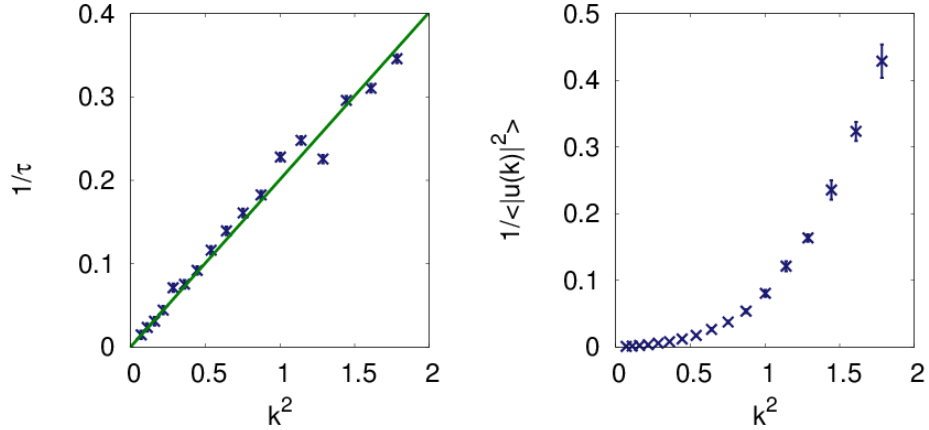


Figure 7.8: Inverse of decay times  $\tau$  and inverse of square amplitudes of the fluctuations versus  $k^2$ .

and that the lowest eigenmodes decay slowly on the order of several million time steps. For each stored configuration snapshot the spatial Fourier components of the fluctuations were evaluated using Equation (7.4) for a range of wave vectors (Equation (7.14)) and their time correlation function  $c(k, t)$  were calculated using Equation (7.7). Due to the periodic boundaries the wave vector  $k$  was restricted to

$$k = \frac{2\pi}{L_z} m. \quad (7.14)$$

Here  $m$  is an integer and the box length along  $z$   $L_z \sim 94.1\sigma_0$ . We limited our interest to  $1 \leq m \leq 20$ .

Decay coefficients  $\tau$  were obtained from exponential fits and are plotted over  $k^2$  in Fig. 7.8. In addition the inverse of the square amplitudes of the fluctuations are shown versus  $k^2$ . The statistical errors on these quantities were estimated by a block averaging procedure with 10 blocks. The error on the decay times ( $\pm 0.005$ ) was obtained from the observed variations when varying our choices of the origin of  $u$  or the fitting range for  $c(t)$ . The lowest three eigenmodes ( $k = 1 \rightarrow 3$ ) were neglected, since their relaxation times are long compared to the length of the simulation. In both graphs the intercept is marginally small and we therefore argue that  $\gamma = 0$ . In other words the external field chosen here has no impact on the fluctuation dynamics. The inverse of the decay rates  $1/\tau$  is directly proportional to  $k^2$ , as we expected from theoretical predictions (Equation (7.6)). The gradient obtained from the linear fit corresponds directly to the ratio of line tension and the viscous

drag  $\Lambda/R = 0.20 \pm 0.01$ . From Equation (7.1) and Equation (7.2) we evaluated a crude theoretical estimate for the ratio giving  $\Lambda/R = 0.68$ . Our measure value is  $\sim 71\%$  less than the theoretical predicted one. This observation is in agreement with [201, 202, 207], who observed deviations ranging from 50% to 85%. This confirms that Equation (7.2) does not estimate the viscous drag adequately and the coupling of the director to the flow field is indeed important.

For inverse amplitudes of the fluctuations we do not observe the expected linear relation of  $k^2$ . In addition they appear to depend on the higher order term  $k^6$ . This is not captured in our theoretical description and will require further analysis.

## 7.5 Conclusions

A single  $-1/2$  disclination line was stabilised in a molecular simulation by applying an external field. The equilibration process of the disclination was presented showing the single disclination develop out of a network of disclinations similar to observations made in experiments in regions where laser tweezers are applied. The total lengths of disclinations in the system followed an exponential decay until it plateaus to its equilibrium value. We have confirmed that there is significant decrease in uniaxial order in the defect core region and that the defect core is strongly biaxial. The equilibration fluctuation dynamics of the disclination were analysed in reciprocal space allowing to estimate the ratio of the line tension and the viscous drag. We obtained  $\Lambda/R = 0.2 \pm 0.01$ . This differs from the theoretical prediction, that does not consider the backflow confirming that the coupling is important and has to be incorporated. Future work is required to understand the dependence of the inverse amplitudes of the fluctuations on  $k^6$ , which was not captured in our theoretical model. The cylindrical external field perturbs the local director fluctuations out of the  $x$ - $y$  plane and within it, which might have an effect on the fluctuation amplitudes. To analyse the impact of surface anchoring a nanoparticle could be pinned at the centre of the boundary to fix the ends of the disclinations.

## Chapter 8

# Interaction of nanoparticles with a single disclination line

### 8.1 Introduction

In recent years the interactions of particles with disclination lines have attracted great research interest. Particles placed in close vicinity of a  $-1/2$  defect line were shown to experience attractive non-radial forces, which move the particle towards the disclination line [211–213]. The forces strongly depend on the particle size, its surface treatment and the separation  $r$  between the particle and the line. This interaction can be utilised to control the motion of particles inside a liquid crystal as well as to trap particles in defect sites. Here the trapping occurs, because the disclination line is trying to minimise the effective volume of its disordered defect core. While small particles are trapped in the defect line itself, large particles were also shown to be trapped in particular points in between lines [214]. The trapped particles can easily be controlled with the laser tweezers [208, 209] and therefore one has indirect control of the movement of the disclination line.

Pires et al. [211] studied the trajectories of micron sized particles near a single defect line under the microscope and observed that the particles slowly approach the defect line in a curved motion. The measured trajectories were found to be in good agreement with hydrodynamics predictions. The interaction potential appears to be proportional to  $\sim r^{-3}$  for dipoles and  $\sim r^{-5}$  for quadrupoles [211]. Their work suggests that the motion is initially driven by Brownian motion, until the attraction by the defect line dominates. Due to the deformation of the disclination line caused by thermal fluctuations obscuring the view under the microscope, the dynamics could not be studied, when the particles were in very close proximity of



the line. The study was limited to micron sized particles that are accompanied by a dipolar defect.

Experimental work by Škarabot et al. [43] and Gharbi et al. [215] also showed strong attraction of small particles towards the Saturn ring of a larger particle. Once the particles reach the disclination line, they became trapped with energies several orders of magnitude higher than thermal fluctuations. Again, during the approach the nanoparticle was observed to follow a bent trajectory, when it was allowed to move freely. Using laser tweezers an energy barrier of several  $100k_{\text{B}}T$  was measured for particles which were forced to move towards the Saturn ring in a straight line, underlining the highly non-linear interactions. In addition, trapping of particles was observed for nanoparticles in defects in smectic LC [216].

Landau-de Gennes free energy minimisation confirms that the migration of nanoparticles into the defect line minimises the total free energy [199]. Here anchoring strength and particle size were identified as key properties for the possibility of trapping. The trapping can be utilised to form superstructures with a mixture of large particles and small particles, where the small particles are trapped in the defect lines of the large particles forming strongly-bound networks [217]. This opens a new pathway to design colloidal liquid crystal materials with controllable properties. A profound understanding of the mechanism is required in order to utilise it for potential applications.

Engström et al. [218] have recently exploited the trapping mechanism of nanowires in defects in chiral nematics. Since the axes of the wires spontaneously orient along the director, they can provide nondestructive visualisation of the changes in the director field over space and time. Other experiments have successfully assembled fixed chains of colloids by trapping them in disclination lines and joining them permanently by the use of electropolymerization [212]. Sengupta et al. [219] explored the possibility of using liquid crystals in microfluidic devices; the disclination line forming inside the channel can act as a guide for the trapped particles and Y junctions can be used to switch between different targets.

Another area of interest are colloidal liquid crystal blue phases, which can occur in strongly chiral nematics. Blue phases have a characteristic periodic network of disclination lines. To understand the impact of nanoparticle inclusions in blue phases Ravník et al. [220] used Landau-de Gennes free energy minimisation. They observed that the defects act as trapping sites with strong binding energies of up to several thousands  $k_{\text{B}}T$  between the defect lines and the trapped particle.

Although particle interactions with defects are reasonably well understood for micron sized particles, little has been researched about particles of nanometre



size [31, 186, 221, 222]. The tracking of small particles in experiments is rather challenging. Jose et al. [67] recently attempted to simulate the trapping of nanoparticles in a disclination line on a molecular scale using Monte Carlo and the Lebwohl-Lasher model. The  $-1/2$  disclination line was stabilised by confining the LC to a prismatic nanochannel. They qualitatively studied the deformation of the defect line caused by particles in close vicinity and measured the force on the nanoparticle to estimate the line tension. Such lattice simulations have the advantage of being computationally inexpensive. The question arises however whether the lattice restriction has a significant impact on the results. Especially the movement of the nanoparticle, which is large compared to the lattice site, is somewhat abrupt and nonphysical.

In this chapter the trapping mechanism is studied for nanoparticles on a molecular level using the off-lattice Gay-Berne interaction potential to simulate a bulk nematic. The defect structures arising due to particles in the close vicinity of the defect line and the forces acting upon them are analysed. Furthermore the trajectories of particles near a disclination line are studied to aid understanding the interactions between defect lines and nanoparticles. In the last part the particle-particle interactions are investigated for two particles trapped in the same disclination line.

## 8.2 Model and simulation details

A simulation box filled with 125 000 GB molecules of elongation  $\kappa = 5.0$  and a moment of inertia  $I = 7.0$  was equilibrated at a density  $\rho = 0.15$  and  $T = 1.0$ . The interaction potential is the purely repulsive Gay-Berne potential with a potential cutoff of  $6\sigma_0$  (see Section 2.3). A nanoparticle was inserted into the nematic that interacts via the purely repulsive LJ potential inducing homeotropic surface anchoring (see Section 5.2). The size of the nanoparticle was set to  $R_{\text{NP}} = 10\sigma_0$  with a mass  $m = 50$ . A single defect line is stabilised by applying the external field, described in Chapter 7, near the boundaries of the simulation box. The boundary region is defined by a cylinder with its axis along  $z$  and a radius of  $R_{\text{cyl}} = 40.0\sigma_0$ . The external field with maximum strength  $f_0 = 2.0$  is applied within the region  $R_{\text{cyl}} \pm \Delta$ , with  $\Delta = 7.0\sigma_0$ . As shown in Chapter 7 this external field stabilises a single disclination line, which follows the direction of the cylinder axis undergoing thermal fluctuations. The simulation was repeated for eight different initial positions of the nanoparticle, which are indicated in Fig. 8.1 to account for the varying structure of the  $-1/2$  defect for varying  $\phi = \text{atan}(y/x)$ . We will refer to these runs as setup0, setup30, setup60, setup90, setup120, setup150, setup180 and setupC, where

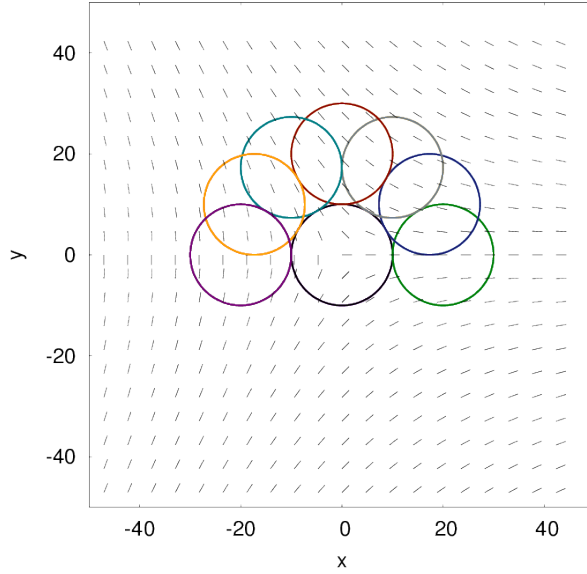


Figure 8.1: Sketch of the director field corresponding to a  $-1/2$  defect in the  $x$ - $y$ -plane. The circles indicate the initial position of the nanoparticle  $(x, y, 0)$  in the simulation box with setupC (black), setup0 (green), setup30 (blue), setup60 (grey), setup90 (red), setup120 (cyan), setup150 (orange) and setup180 (purple).

the number corresponds to the angle  $\phi$  and the C indicates the positioning at the centre of the box. In Chapter 7 we have shown that the dynamics of the system evolve slowly; hence the equilibration run ( $NVT$  ensemble) had to be sufficiently long. For each setup it was chosen to be  $3 \times 10^6$  steps with a time step  $\Delta t = 0.002$ . This was followed by a  $NVE$  production run of  $2 \times 10^6$  time steps with system snapshots stored every 2500 time steps. For these runs the position of the nanoparticle was fixed. In a second production run ( $NVT$  ensemble) of length  $12 \times 10^6$  steps the nanoparticles were allowed to move freely and their position was recorded every 2500 time steps.

In addition three systems were studied with two nanoparticle inclusions in close vicinity of a defect line. For the first one, the simulation box was duplicated twice along  $z$  giving a total of 375 000 GB molecules and a simulation box ratio of 1:1:3. Two nanoparticles were placed in the centre of the box separated by  $\sim 94\sigma_0$  along  $z$ . The system was equilibrated over  $3.5 \times 10^6$  time steps ( $NVT$  ensemble), followed by a production run ( $NVT$  ensemble) of length  $3.5 \times 10^6$  steps storing a snapshot every 2500 time steps. The other two simulations were conducted in the previous setup with 125 000 GB molecules with two nanoparticles separated

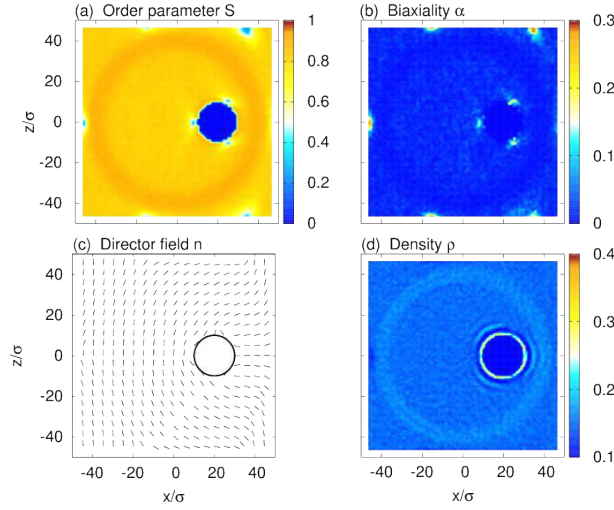


Figure 8.2: Maps of the local order, biaxiality, director field and density in the  $x$ - $y$  plane with the nanoparticle at  $z = 0$  for setup0. Data was accumulated over  $2 \times 10^6$  time steps with intervals of 2500. The bin size was chosen to be  $0.6\sigma_0$  giving an average of over 180 molecules per bin.

perpendicular and parallel to the defect line. The initial positions of the nanoparticles are given by  $\mathbf{r}_1 = (-15\sigma_0, 0, 0)$ ,  $\mathbf{r}_2 = (15\sigma_0, 0, 0)$  and  $\mathbf{r}_1 = (0, 0, -15\sigma_0)$ ,  $\mathbf{r}_2 = (0, 0, 15\sigma_0)$  respectively. The production run length was  $12 \times 10^6$  steps.

### 8.3 Data analysis and results

#### Interactions of disclinations with fixed nanoparticles in close vicinity

A nanoparticle inserted into a nematic distorts the surrounding director field. Complex defect structures arise due to the competition between the director field enforced by the external field and the distortion around the particle. In Fig. 8.2 the time-averaged maps of the order parameter, biaxiality, director field and density are shown in the  $x$ - $y$  plane with the nanoparticle at the origin (setup0). Three distinct defect regions can be seen near the surface of the nanoparticle with  $a \sim 1.15R_{\text{NP}}$ . Inside the defect core region the order parameter drops and the biaxiality increases significantly. The defects are equally spaced around the nanoparticle maximising the distance between each other. 3D analysis confirms that the two defects further away from the origin correspond to a Saturn ring surrounding the nanoparticle and the third defect is the cross-section of the disclination line in the centre of the simulation box induced by the external field. Interestingly the Saturn ring is positioned off-centre; shifted roughly  $5\sigma_0$  away from the equator. The cylinder region where

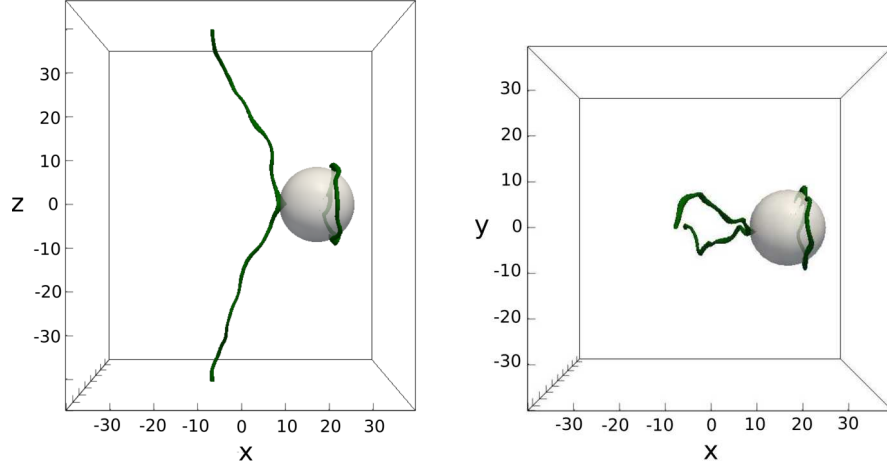


Figure 8.3: 3D visualisation of defect lines (blue) for setup0 from the  $x$ - $z$  perspective (left) and the  $x$ - $y$  perspective (right) for a single time step. Defect corresponds to regions of low uniaxial order ( $c_l < 0.12$ ).

the external field is applied is visible showing a higher order than inside the bulk as well as lower biaxiality and higher density. These effects do not propagate into the bulk.

In Fig. 8.3 a typical defect structure, corresponding to  $c_l < 0.12$ , is shown in 3D for setup0. The shifted Saturn ring surrounding the nanoparticle can clearly be seen. Furthermore the disclination line is strongly bent and ‘touches’ the surface of the nanoparticle. The distance of the defect line from the surface of the nanoparticle is comparable to the distance of the Saturn ring from the nanoparticle’s surface. Thermal fluctuations are visible in the disclination line as well as the Saturn ring. For setup0 this defect configuration was the only one observed for the duration of the production run.

What defect structures arise when the nanoparticle is placed in the centre of the simulation box? In Fig. 8.4 time-averaged order parameter and director field plots are shown as well as a 3D visualisation of defect regions for a single time step. As before, in the 2D maps three defect regions were observed near the surface of the nanoparticle. However the 3D visualisation shows that these correspond to an entangled defect structure, where the line closely follows the contours of the particle. It appears that the distance between different segments of the defect line is maximised. For the duration of the production run the entangled defect structure persists and no other configuration was observed. A stable entangled defect structure was only observed for setupC. Note that for the entangled defect the symmetry

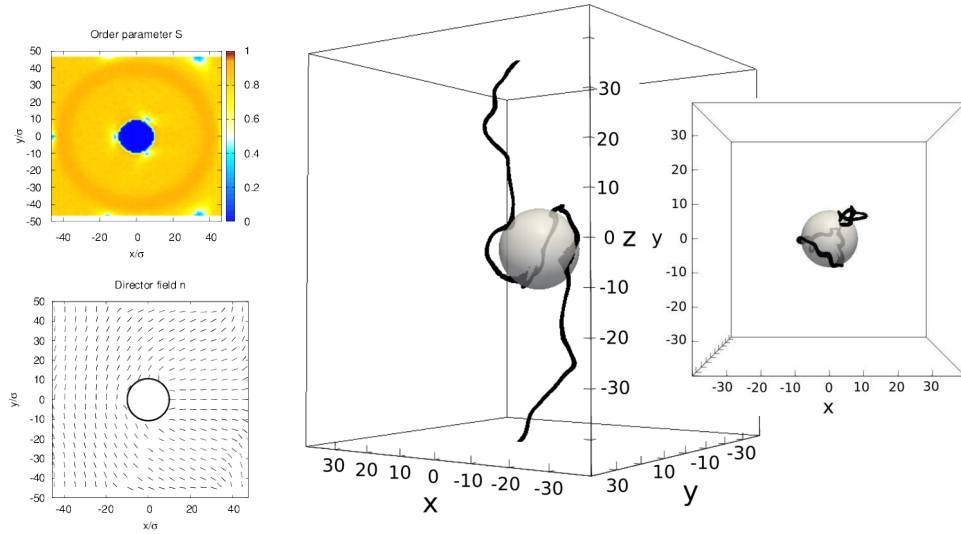


Figure 8.4: Defect visualisation for setupC. Notation as in Fig. 8.2 and Fig. 8.3.

is spontaneously broken. Throughout the duration of the production run the defect did not change handedness, suggesting an energy barrier higher than thermal energies. These observations are in qualitative agreement with the off-lattice simulations by Jose et al. [67], who observed the same entanglement. They reported occasional transformation between different entanglements. A possible explanation is the difference in particle size in their simulation. Fig. 8.5 shows the time-averaged isosurface corresponding to low uniaxial order with  $S < 0.5$ . One can see that the structure remains unchanged throughout the production run and that its shape closely follows the contours of the nanoparticle.

In Fig. 8.6 the time-averaged local order maps and director fields are shown for the remaining systems setup30  $\rightarrow$  setup180 and Fig. 8.7 shows the defect regions in 3D for a single time step. For all setups the defect region closest to the origin is the cross-section of the single disclination line and the remaining two defects correspond to a Saturn ring defect. The orientation of the Saturn ring strongly depends on the orientation of the surrounding  $-1/2$  defect. The plane described by the Saturn ring, is perpendicular to the ideal director orientation at the position of the nanoparticle. For setup60 and setup180 one can observe a strong bending of the single defect line away from the Saturn ring. Both left and right bends occur equally often confirming that the two states are degenerate. For setup60 and setup180 only, entangled as well as non-entangled defect structures were observed with several transitions between the different states. We suspect that the strong bending of the disclination associated with the non-entangled state increases the total length and hence the energy



Figure 8.5: Disclination line (red) corresponding to the isosurface of low uniaxial order with  $S < 0.5$  for time-averaged production run for setupC.

associated with it, making it a less stable state and allowing transitions to the entangled structure. For setup60 and setup180 a variety of intermediate defect structures were observed during the transitions. Snapshots of these as well as entangled defect structures are shown in Fig. 8.8. No entangled or intermediate defect structures were observed for setup0, setup30, setup90, setup120, setup150 suggesting that the bent single disclination line and a Saturn ring perpendicular to the direction of the director field is the only stable configuration.

### Dynamics of nanoparticles in close vicinity of a disclination line

In the following the trajectories of the freely moving nanoparticles are studied. Fig. 8.9 shows the trajectories of the nanoparticles for each setup in the  $x$ - $y$  plane over the entire length of the production run. The initial positions of the nanoparticles are indicated by a grey circle. Translations in the  $z$  direction were neglected, because they are energetically degenerate since the director field surrounding the disclination line is nearly identical everywhere along  $z$ . Two different mechanisms seem to drive the nanoparticles: (1) all particles move towards the centre of the simulation box remaining at a distance of roughly  $10\sigma_0$  from the origin. This distance is equivalent to the radius of the nanoparticle  $R_{NP}$  and hence minimises the bending of the disclination line, which minimises the free energy associated with the defect line. The nanoparticles reach this position after roughly  $1 \times 10^6$  time steps. (2) particles appear to have an angular preference. Their final average positions correspond to  $\phi = 0$  and  $\phi = 2\pi/3$ .  $\phi = 4\pi/3$  was not observed due to our choice of initial positions, but is degenerate due to the three fold symmetry of the disclination line. At their final equilibrium positions the particles undergo thermal fluctuations.

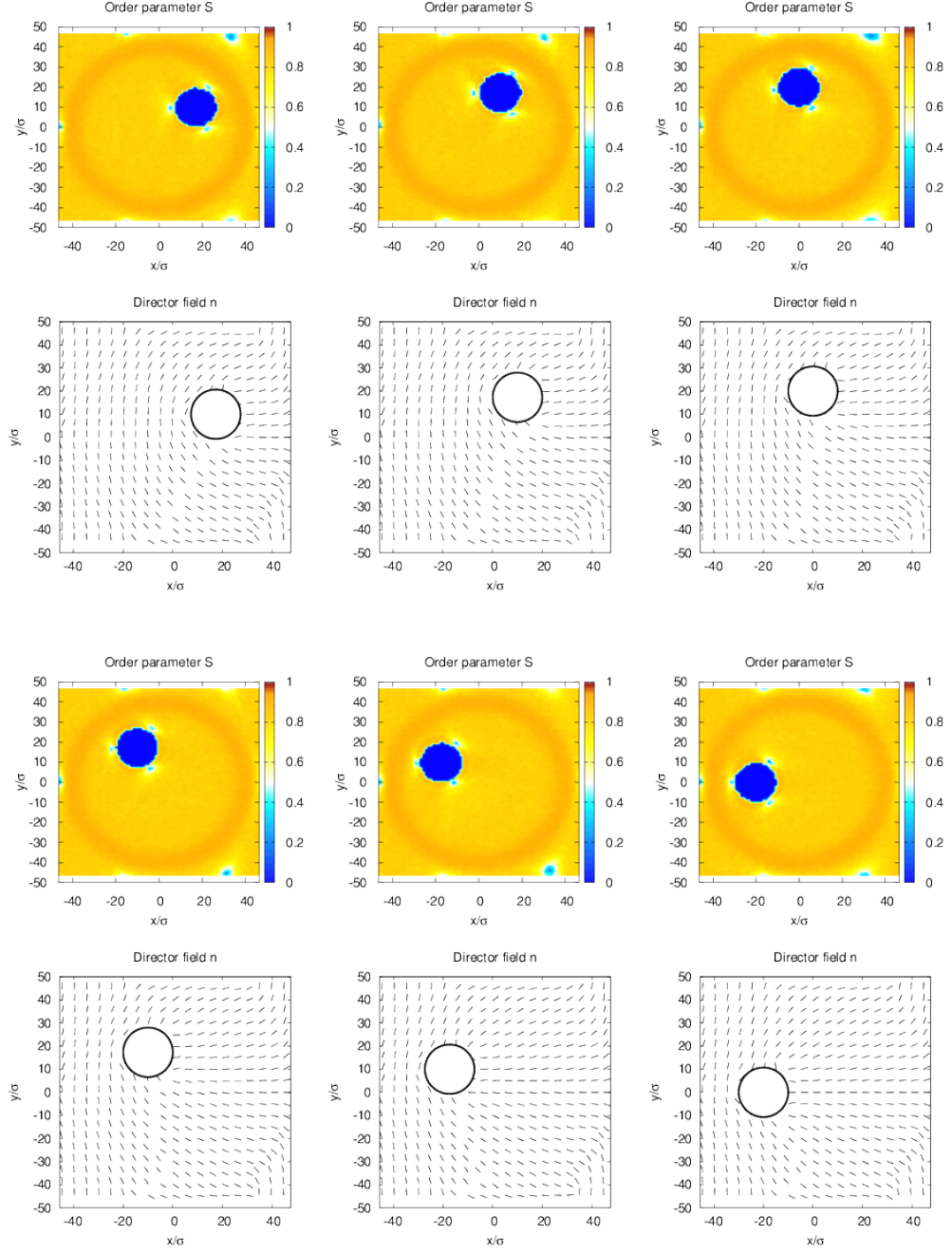


Figure 8.6: 2D time-averaged local order parameter and director field maps. From top left to bottom right: setup30, setup60, setup90, setup120, setup150 and setup180. Notation as in Fig. 8.2.

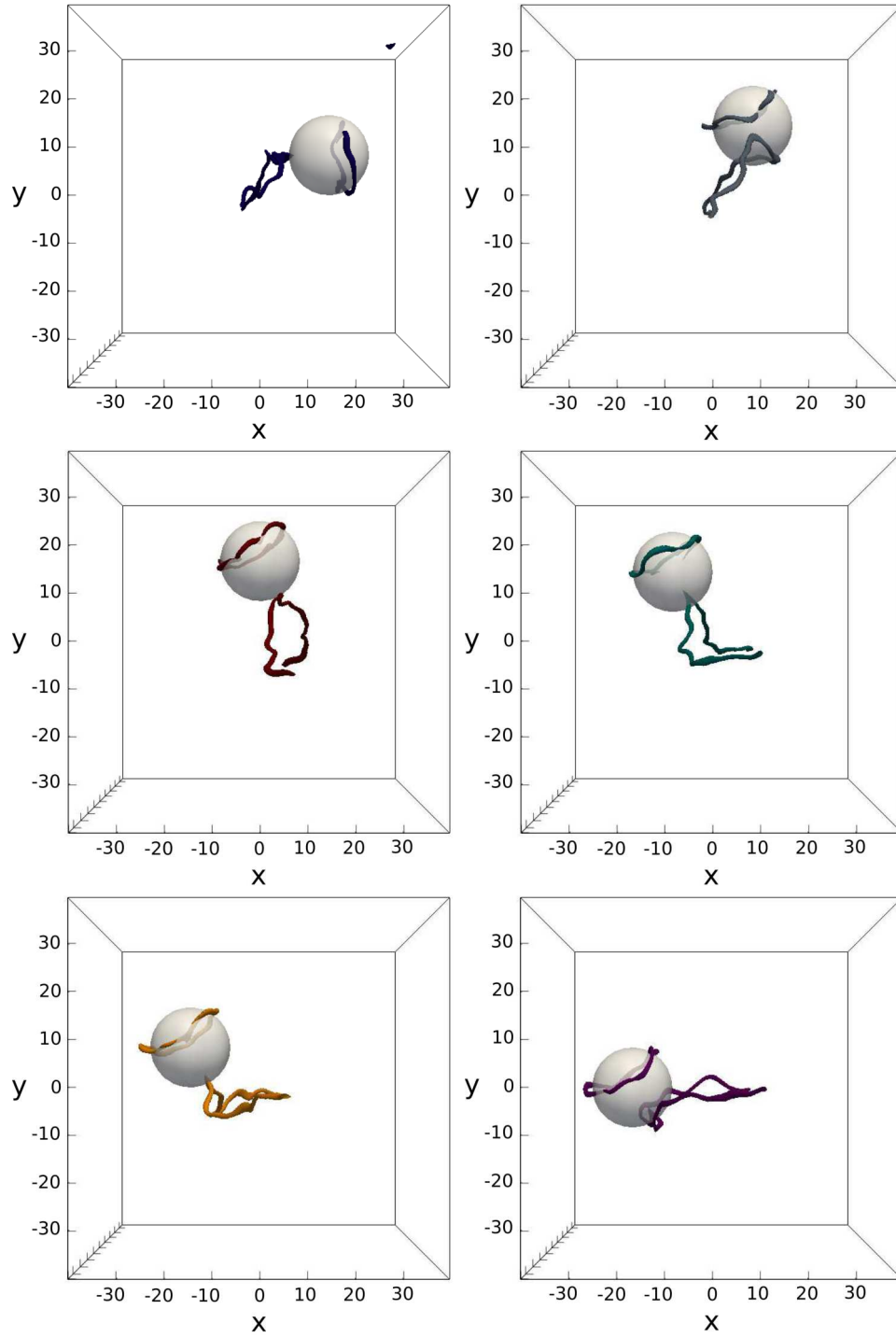


Figure 8.7: 3D visualisation of typical defect structures observed for setup30  $\rightarrow$  setup180 from the  $x$ - $y$  perspective (topview). Colour scheme used as introduced in Fig. 8.1.



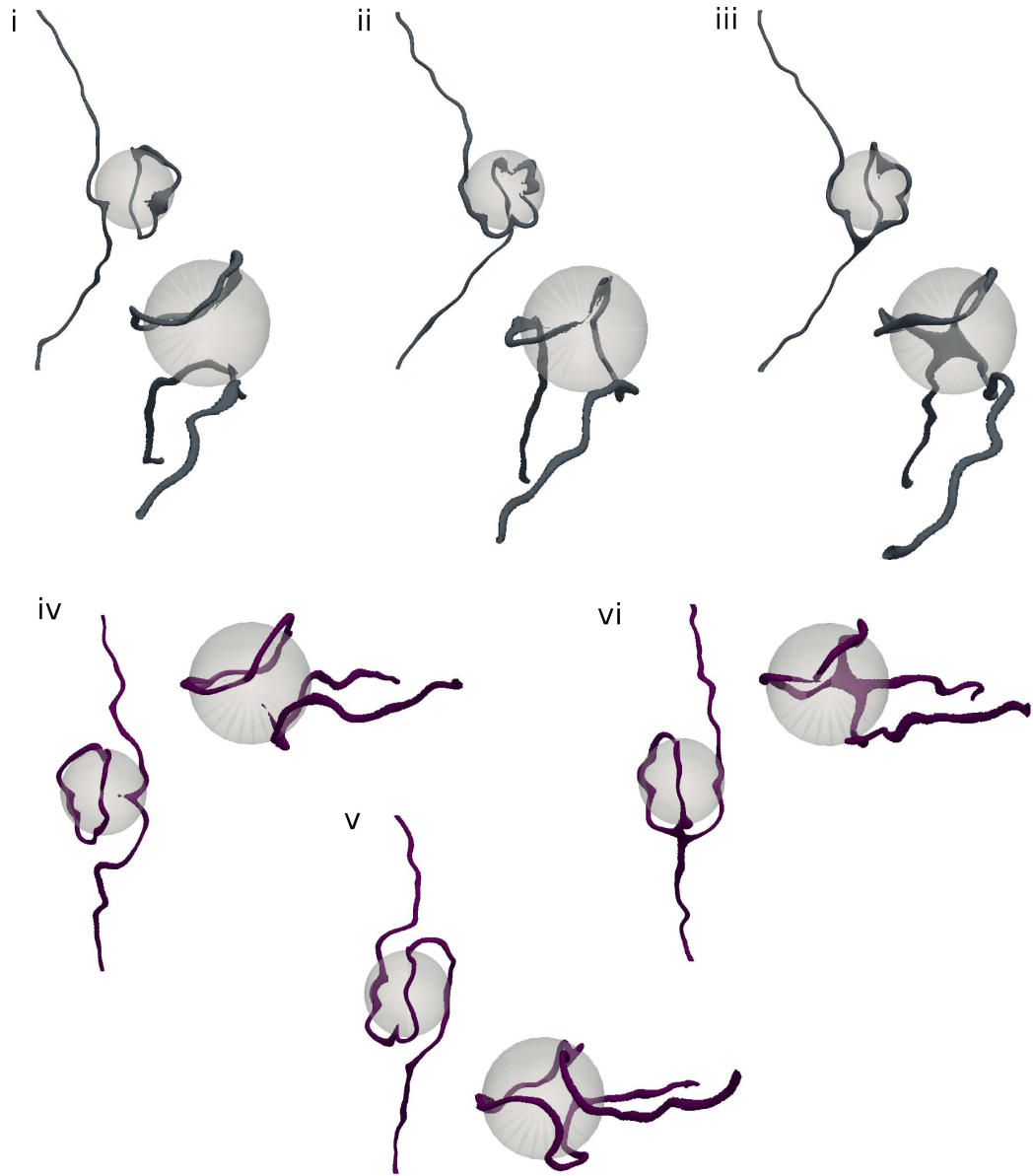


Figure 8.8: Six examples of entangled and intermediate defect structures observed for setup60 (grey) and setup180 (purple). All examples are shown from two different angles.

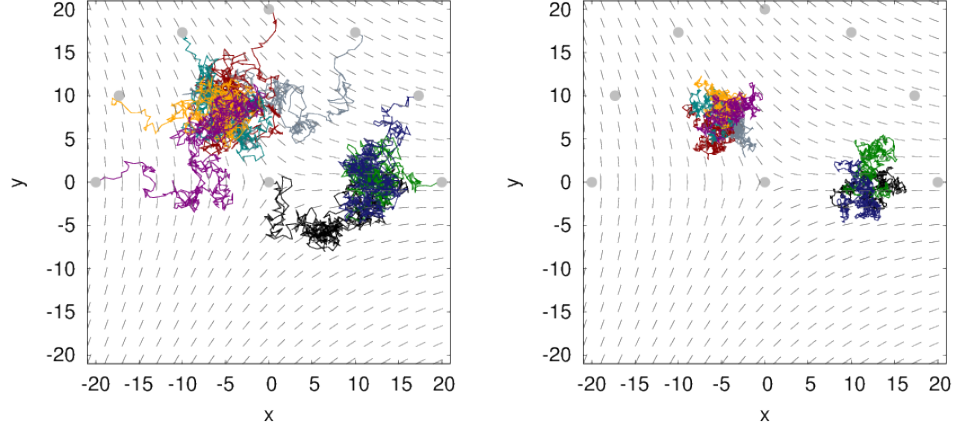


Figure 8.9: Trajectories of nanoparticles for all setups in the  $x$ - $y$  plane. Left shows the trajectories over the entire length of the production run. Right only shows the trajectories for the last  $2 \times 10^6$  time steps. Grey circles indicate the initial positions.

Throughout the length of the run no translations to a different equilibrium position were observed. For all setups the particles remain connected to the disclination line at all times. The nanoparticle placed at the centre of the box, moves outwards and the defect disentangles suggesting that the entangled structure is of higher energy for the system studied here.

In the following the net forces on the fixed nanoparticles due to the interactions with the liquid crystal molecules were analysed. The forces, time-averaged over the entire length of the production run, are plotted in Fig. 8.10. Again the theory is supported that there are two main mechanism: (1) all particles experience a strong attractive force towards the disclination line. Only the particle placed at the origin is exposed to a weak repulsive force. (2) the forces have a non-radial component and show an angular tendency towards  $\phi = 0$  and  $2\pi/3$ .

### Interactions of two nanoparticles in close vicinity of a disclination

Three different setups were studied with two nanoparticles in close vicinity of a disclination varying their separation and their relative positions with respect to the disclination. The systems were equilibrated with the positions of the nanoparticles fixed. Throughout the production run the nanoparticles were moving freely and their positions were tracked. To analyse their trajectories the vector connecting the positions of the nanoparticles  $\mathbf{r}_{12} = \mathbf{r}_2 - \mathbf{r}_1$  was calculated for each snapshot.

For the first simulation two nanoparticles were placed at the centre of the

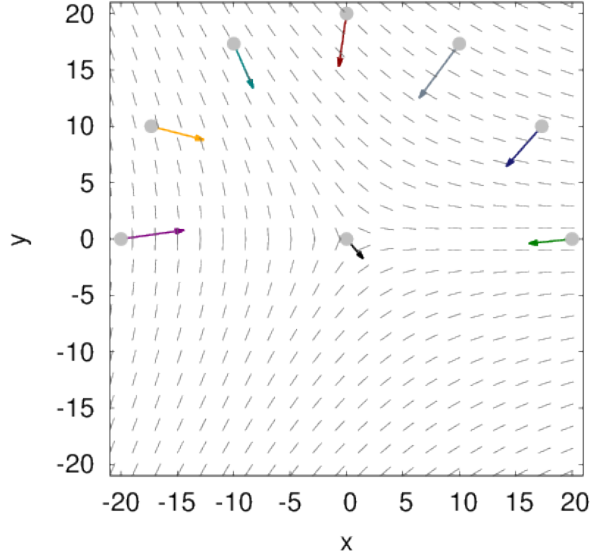


Figure 8.10: Time-averaged forces acting on the nanoparticles due the interactions with the liquid crystal molecules plotted for all setups.

disclination line separated by  $\sim 94\sigma_0$  along the  $z$  axis. Within a few thousand time steps both nanoparticles became entangled by the defect line. In Fig. 8.11 the  $x$ ,  $y$  and  $z$  component of  $\mathbf{r}_{12}$  are plotted for the entire duration of the production run, in which the nanoparticles were allowed to move freely. Both particles undergo diffusion around the centre of the defect line. The separation along  $z$  suggests that there is no significant interaction between the particles; at least not on the short time scales accessible in simulations.

The simulation was repeated in a smaller simulation box with 125 000 Gay-Berne molecules and a smaller separation of  $30\sigma_0$  along  $z$ . In Fig. 8.12 the defect lines are shown for the first and the final time step of the production run. One can see that both particles are initially entangled by the defect line and for the length of the simulation they were never observed to become disentangled. As for the larger system the  $x$ ,  $y$  and  $z$  component of  $\mathbf{r}_{12}$  are plotted for the entire duration of the production run, see Fig. 8.13. The separation along  $x$  and  $y$  increases over the first  $5 \times 10^5$  time steps suggesting that the particles prefer to sit slightly shifted with respect to each other. Afterwards these components do not change for the remainder of the production run and they solely fluctuate around their equilibrium value. To further investigate the separation between the particles in the  $x$ - $y$  plane  $R_{xy}$  (see red line) was identified.  $R_{xy} = 7.0\sigma_0 \pm 1.8\sigma_0$  for the last half of the

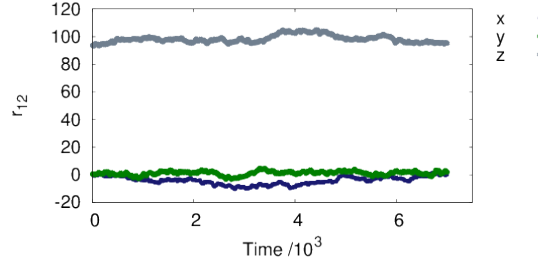


Figure 8.11: The  $x$  (blue),  $y$  (green) and  $z$  (grey) components of the vector  $\mathbf{r}_{12}$  connecting the positions of the two nanoparticles over time. The particles were initially placed in the centre of a simulation box with 375 000 Gay-Berne molecules separated by  $94\sigma_0$  along  $z$ .

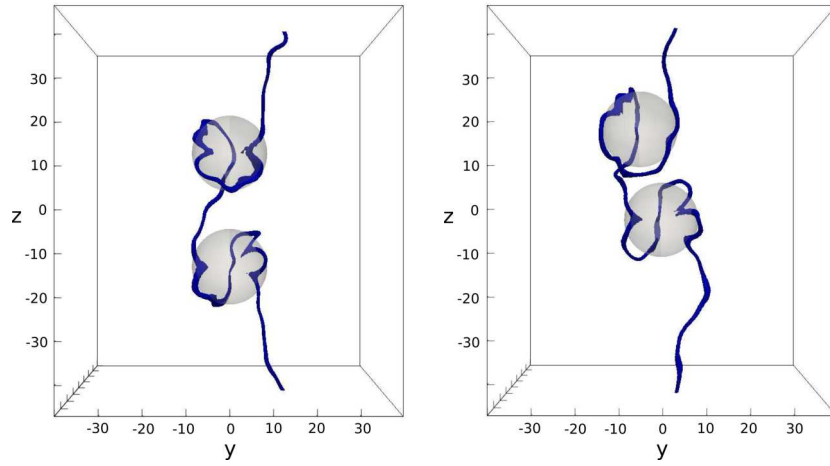


Figure 8.12: Two nanoparticles initially placed at centre of disclination line separated along  $z$  by  $30\sigma_0$ . Left shows disclination line (blue) for the first time step of production run and right shows the last time step.

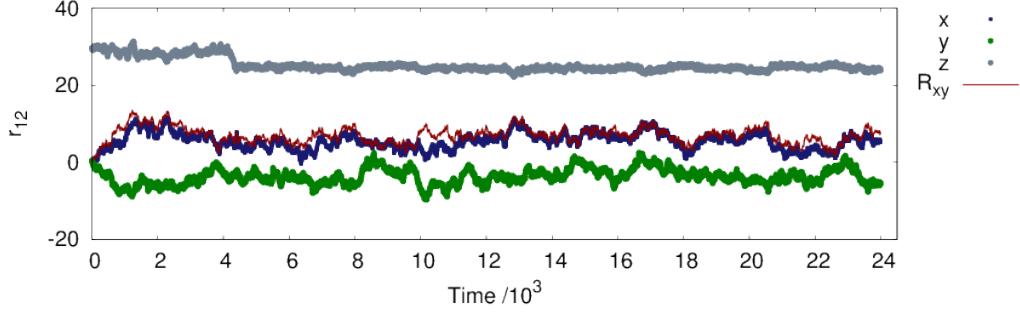


Figure 8.13: The  $x$  (blue),  $y$  (green) and  $z$  (grey) components of the vector  $\mathbf{r}_{12} = \mathbf{r}_2 - \mathbf{r}_1$  connecting the positions of the two nanoparticles over time. The two nanoparticles were initially placed in the centre of simulation box with 125 000 Gay-Berne molecules separated by  $30\sigma_0$  along  $z$ . The red line corresponds to the separation of the particles in the  $x$ - $y$  plane  $R_{xy}$ .

run. Referring back to Fig. 8.12 one can see a possible explanation. The short disclination line segment between the two particle can be straight, only if one particle is slightly shifted sideways. This in turn reduces the total length of the line and the surrounding distortions. In contrast to the larger system, the separation along  $z$  decreases significantly corresponding to the particles attracting each other. After the initial approach the average separation along  $z$  remains constant at  $24.4 \pm 0.5\sigma_0$ .

We turn our focus to the same system but with the two nanoparticles separated along  $x$ . In Fig. 8.14 the disclination lines are visualised for the first and last time step of the production run. Initially the disclination line induced by the external field entangles one of the nanoparticles, while the other particle is surrounded by an off-centre Saturn ring. As before the shift was away from the single defect line. Shortly after the particles were released the entangled particle became disentangled, while the defect structure around the second particle remained unchanged. Similar to the observations for a single nanoparticle, the disclination line ‘touches’ both nanoparticles. In Fig. 8.15 the trajectories of the nanoparticles are plotted. The separation of the nanoparticles along  $z$  suggests that the particles repel each other and reach their equilibrium position after  $6 \times 10^6$  time steps (half the production run length). Afterwards the average  $z$  separation stays constant with  $r_{12}^z = 49.4 \pm 2.7$ . In addition, one can see that the separation along  $z$  across the periodic boundary is comparable with  $L_z - |r_{12}^z| = 44.6 \pm 2.7$ , which suggest that the particles are trying to maximise the distance between each other. For the second half of the run the distance between the two particles in the  $x$ - $y$  plane was  $R_{xy} = 19.9\sigma_0 \pm 6.6\sigma_0$ . Referring back to Fig. 8.14 one can see that the particles both moved into one of the

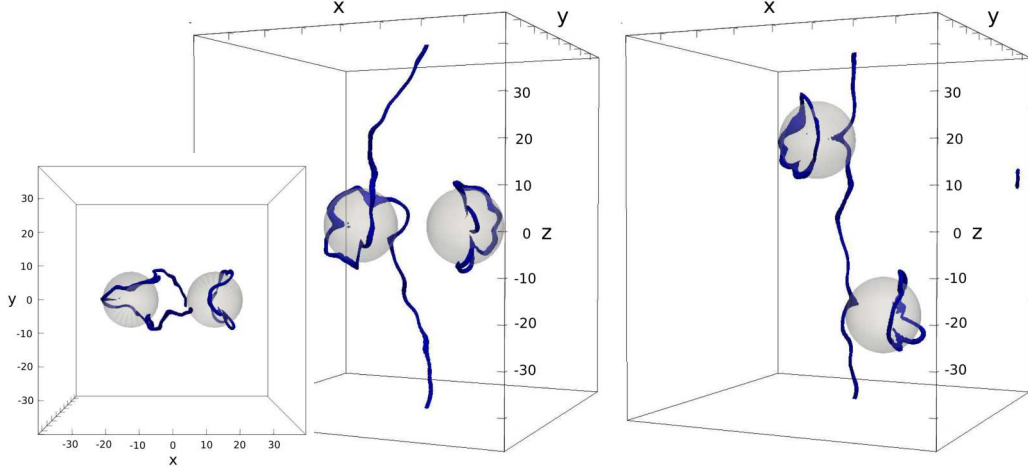


Figure 8.14: Two nanoparticles initially placed at centre of the simulation box separated along  $x$  by  $30\sigma_0$ . Left shows disclination lines (blue) for the first time step of production run and right shows the last time step. Inset shows the first time step viewed from the top.

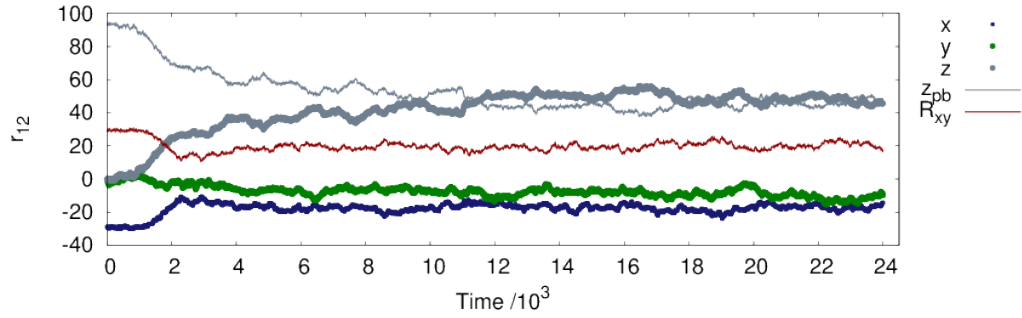


Figure 8.15: The  $x$  (blue),  $y$  (green) and  $z$  (grey) components of the vector  $\mathbf{r}_{12} = \mathbf{r}_2 - \mathbf{r}_1$  connecting the positions of the two nanoparticles are plotted over time. The two nanoparticles were initially placed in the centre of simulation box with 125 000 Gay-Berne molecules separated by  $30\sigma_0$  along  $x$ . The red line corresponds to the separation of the particles in the  $x$ - $y$  plane. The thin grey line indicates the separation along  $z$  across the periodic boundary  $L_z - |r_{12}^z|$ .

three equilibrium positions we identified for a single nanoparticle. Hence we would expect a separation of  $\sim 17.3\sigma_0$  between two equilibrium positions, which is consistent with our measurement. It is interesting that in this simulation the particles' equilibrium positions correspond to different angles  $\phi$ . It seems possible that for different initial conditions the particles could move towards positions corresponding to the same angle; however favouring different positions could be related to smaller distortions of the liquid crystal. This angular dependency would be an interesting topic for further investigations.

When comparing these two simulations with the same setup but different initial conditions, it is surprising that the final defect structures are entirely different. For one system both particles approached each other and remained entangled for the duration of the run. This is somewhat surprising since we observed the particle in setupC to quickly disentangle. It appears that the second particle supports the entanglement. For the second system the particles repel each other maximising the distance between them. Entanglement was only observed at early time steps, while later two separated Saturn rings were the only stable structure. It would be interesting to extend these exploratory simulations to identify all possible stable defect structures and to analyse the impact of the initial conditions.

## 8.4 Conclusions

To conclude, we have observed attractive interactions between a single disclination line and a nanoparticle in close vicinity. When the nanoparticle's position was fixed, the nearby disclination line was bending towards the particle to minimise elastic free energy; the particle itself was surrounded by an off-centre Saturn ring. When the particle was released, it moved towards the centre of the simulation box. This allowed the disclination line to become straight, which minimised its length and hence the energy associated with it. The particles trajectories were non-linear and highly dependent on the structure of the surrounding director field. Three equilibrium positions were identified reflecting the three-fold symmetry of the director field. For a range of simulations with fixed nanoparticle positions the particle became entangled by the disclination line. When the particles were released, they rapidly disentangled suggesting that the entangled state is unstable for nanoparticles of the size studied here. In addition, intermediate defect structures were observed during transitions from the entangled to non-entangled structure and vice versa.

Furthermore we have shown that two nanoparticles can strongly interact in the presence of a nearby disclination line, if their surface-to-surface separation is

comparable to their diameter. For two different initial nanoparticle positions two entirely different structures were observed. For one simulation both particles stayed entangled and attracted each other until they reached an equilibrium separation. It appears that the presence of the second particle supported the entanglement with both particles staying entangled throughout the simulation. For the other structure the particles repelled each other and maximised the separation between them. The entangled particle quickly disentangled and both particles were surrounding by an off-centre Saturn ring.

We have successfully shown that molecular simulations can be exploited to study single disclination lines in liquid crystals and their interaction with nearby particles. The results are in quantitative agreement with experiments and theory. By increasing the size of the simulation box and hence the size of the bulk nematic region in the simulation larger particle inclusions could be studied. This is beyond the scope of this study; however it would be an interesting topic for further investigations.



## Chapter 9

# Conclusions

We have shown that molecular simulations are a useful additional tool to study liquid crystals complementing theoretical predictions and experimental results and aid understanding the underlying dynamics on a molecular level.

**Chapter 3:** A nematic was simulated using the soft Gay-Berne potential. The Frank elastic constants corresponding to splay ( $K_1$ ), twist ( $K_2$ ) and bend ( $K_3$ ) deformations of the liquid crystal can be calculated from the equilibrium director fluctuations. The fluctuations in reciprocal ( $\mathbf{k}$ -)space were calculated and fitted for low  $\mathbf{k}$  to extrapolate the elastic constants. For the two Gay-Berne parameterisations and total of six state points studied, we obtained  $K_3 \gg K_1 \approx K_2$ , i.e. bend fluctuations require most energy. Our results indicate that small system size may be a source of inaccuracy in previous work; large systems are necessary to obtain a sufficient amount of data points in the low  $\mathbf{k}$  regime.

**Chapter 4:** The dynamics of various Gay-Berne nematics were investigated by calculating the time correlation functions of the director and velocity fluctuations. The splay and twist modes showed exponential decay, whereas the bend modes followed an oscillatory decay. All decay rates were accurately proportional to  $k^2$ . The analysis of the separation of timescales between the director fluctuations and the velocity fluctuations showed that the separation is most prominent for the twist mode and reasonably large for the splay mode. For the bend mode no significant separation was observed. We have successfully shown that these observations are consistent with nematodynamics and that indeed one could see bend propagating modes in experiments, if  $\mu = \rho K_3 / \gamma_1 \eta_2 \sim 10^{-2}$ . This result is particularly exciting since this possibil-

ity has so far been overlooked and instead all three modes are traditionally assumed to be overdamped.

**Chapter 5:** Topological defects caused by nanoparticle inclusions were investigated using molecular simulations. For all particles with homeotropic anchoring the Saturn ring defect was found to be stable for radii ranging from  $3\sigma_0$  to  $15\sigma_0$ . For smaller radii a surface-ring defect arises. For larger radii the distance of the defect from the centre of the particle was measured to be  $a = 1.13R_{\text{NP}} + 0.8\sigma_0$ , which is in agreement with theoretical predictions and experimental observations. Attempts were made to stabilise a metastable satellite defect by the use of an external field. However we have found for particles up to  $20\sigma_0$  that the satellite defect was unstable. This is in agreement with theory and experiments that suggest the Saturn ring to be the one stable configuration for particles of nanometre size. However, it disagrees with the previous simulations of Andrienko and Allen, and we have been unable to discover the reason for the discrepancy. In addition, pair interactions of nanoparticles in nematics were investigated. The particles attracted each other until they reached an equilibrium separation corresponding to a few layers of Gay-Berne molecules. As predicted in mean-field calculations the particles preferred to sit at an angle with respect to the director.

**Chapter 6 :** Molecular simulations of two nanoparticles in close vicinity showed a variety of entangled defect structures arise: the figure of eight, the figure of theta and the figure of omega. These are the same structures seen in experiments for micron-sized particles. The simulation results show that for nanoparticles the transitions between different defect types occur frequently and that no entangled structure persists for more than a few hundred time steps. Intermediate linked defect structures form in-between transitions. These are not seen in experiments; possibly due to high energy associated with them. We explained the origin of the three-ring structure observed in previous molecular simulations as a result of time-averaging over times much longer than the transition rates.

**Chapter 7:** Molecular simulations were used to stabilise a  $-1/2$  disclination by applying an external field. When the field is applied, a network of disclinations forms, which shrinks over time and disclination loops vanish entirely until a single disclination forms. The total length of all disclinations in the network followed an exponential decay. The defect core region showed a significant drop in uniaxial order and was found to be biaxial. Furthermore the equilibrium

fluctuations of the disclination were studied in reciprocal space and we found that the inverse decay rates were accurately proportional to  $k^2$ . Although the amplitudes of these modes did not follow the form expected on the basis of the line tension alone, we found the gradient provided a good estimate for the ratio of line tension and viscous drag.

**Chapter 8:** The interactions of disclinations and nanoparticles were investigated. For a fixed nanoparticle in close vicinity of a  $-1/2$  disclination two defect structures were observed: (1) The nanoparticle was surrounded by an off-centre Saturn ring and the disclination line bends ‘touches’ the surface of the nanoparticle. (2) Entangled defect structures formed for certain nanoparticle positions, where the nanoparticle was entangled by the disclination. Once the nanoparticles were released, they became disentangled. Furthermore they experienced highly non-radial forces that attracted them towards the centre of the simulation box allowing the disclination to become straight. For two nanoparticles in close vicinity of a disclination two different scenarios occurred depending on their initial position: (1) Both particles became entangled by the disclination and stayed entangled throughout the simulation. (2) Both particles became disentangled and two off-centre Saturn ring formed.

# Bibliography

- [1] A. Humpert and M.P. Allen. Propagating director bend fluctuations in nematic liquid crystals. *Phys. Rev. Lett.*, 114:028301, 2015.
- [2] A. Humpert and M.P. Allen. Elastic constants and dynamics in nematic liquid crystals. *Molec. Phys.*, 113:2680–2692, 2015.
- [3] M. Heckmeier, U. Heider, and R. Maisch. Materialien für dünne displays. *Physik Journal*, 14(4):33–38, 2015.
- [4] O.D. Lavrentovich. [http://www.nsf.gov/news/mmg/mmg\\_disp.jsp?med\\_id=59511&from=mmg](http://www.nsf.gov/news/mmg/mmg_disp.jsp?med_id=59511&from=mmg), 1993. Accessed: 24th November 2015.
- [5] U. Tkalec and I. Mušević. Topology of nematic liquid crystal colloids confined to two dimensions. *Soft Matter*, 9:8140, 2013.
- [6] P.G. De Gennes and J. Prost. *The physics of liquid crystals*. Oxford University Press, second edition edition, 1993.
- [7] P.J. Collings and M. Hird. *Introduction to liquid crystal*. Taylor & Francis, 1997.
- [8] D. Demus, J. Goodby, G.W. Gray, H.-W. Spiess, and V. Vill. *Handbook of liquid crystals*. Wiley-VCH, 1998.
- [9] S. Chandrasekhar. *Liquid crystals*. Cambridge University Press, 1992.
- [10] R. Eppenga and D. Frenkel. Monte Carlo study of the isotropic and nematic phases of infinitely thin hard platelets. *Molec. Phys.*, 52:1303, 1984.
- [11] E. de Miguel. Reexamining the phase diagram of the Gay-Berne fluid. *Molec. Phys.*, 100:2449–2459, 2009.
- [12] F. C. Frank. On the theory of liquid crystals. *Discuss. Faraday Soc.*, 25:19–28, 1958.
- [13] M. Ravnik and S. Žumer. Landau-de Gennes modelling of nematic liquid crystal colloids. *Liq. Cryst.*, 36:1201–1214, 2009.
- [14] B. Jérôme. Surface effects and anchoring in liquid crystals. *Rep. Prog. Phys.*, 54:391–451, 1991.

- [15] J.L. Ericksen. Anisotropic fluids. *Arch. Rational Mech. Anal.*, 4:231–237, 1960.
- [16] F. Leslie. Some constitutive equations for liquid crystals. *Arch. Rational Mech. Anal.*, 28:265, 1968.
- [17] D. Forster, T.C. Lubensky, P.C. Martin, J. Swift, and P.S. Pershan. Hydrodynamics of liquid crystals. *Phys. Rev. Lett.*, 26:1016, 1971.
- [18] F.M. Leslie. Theory of flow phenomena in liquid crystals. *Adv. Liq. Cryst.*, 4: 1–81, 1979.
- [19] I.W. Stewart. *The static and dynamic continuum theory of liquid crystals: A mathematical introduction*. Taylor & Francis, 2004.
- [20] O. Parodi. Stress tensor for a nematic liquid crystal. *J. de Physique*, 31: 581–584, 1970.
- [21] D. Andrienko and M.P. Allen. Molecular simulation and theory of a liquid crystalline disclination core. *Phys. Rev. E*, 61:504–510, 2000.
- [22] H.-R. Trebin. The topology of non-uniform media in condensed matter physics. *Adv. Phys.*, 31:195–254, 1982.
- [23] H. Stark. Director field configurations around a spherical particle in a nematic liquid crystal. *Euro. J. Phys.*, 10:311–321, 1999.
- [24] S.V. Shiyankovskii and O.V. Kuksenok. Structural transitions in nematic filled with colloid particles. *Mol. Cryst. Liq. Cryst.*, 321:45–56, 1998.
- [25] D. Andrienko, G. Germano, and M.P. Allen. Computer simulation of topological defects around a colloidal particle or droplet dispersed in a nematic host. *Phys. Rev. E*, 63:041701, Mar 2001.
- [26] O.V. Kuksenok, R.W. Ruhwandl, S.V. Shiyankovskii, and E.M. Terentjev. Director structure around a colloid particle suspended in a nematic liquid crystal. *Phys. Rev. E*, 54:5198–5203, 1996.
- [27] R.W. Ruhwandl and E.M. Terentjev. Monte Carlo simulation of topological defects in the nematic liquid crystal matrix around a spherical colloid particle. *Phys. Rev. E*, 56:5561, 1997.
- [28] T.C. Lubensky, D. Pettey, N. Currier, and H. Stark. Topological defects and interactions in nematic emulsions. *Phys. Rev. E*, 57:610–625, 1998.
- [29] H. Stark. Physics of colloidal dispersions in nematic liquid crystals. *Physics Reports*, 351:387–474, 2001.
- [30] M. Škarabot and I. Muševič. Direct observation of interaction of nanoparticles in a nematic liquid crystal. *Soft Matter*, 6:5476–5481, 2010.

- [31] A.V. Ryzhkova and I. Muševič. Particle size effects on nanocolloidal interactions in nematic liquid crystals. *Phys. Rev. E*, 87:032501, 2013.
- [32] M. Tasinkevych, N.M. Silvestre, and M.M. Telo da Gama. Liquid crystal boojum-colloids. *New J. Phys.*, 14:073030, 2012.
- [33] M.S. Al-Barwani, G.S. Sutcliffe, and M.P. Allen. Forces between two colloidal particles in a nematic solvent. *J. Phys. Chem. B*, 108:6663–6666, 2004.
- [34] P. Poulin and D.A. Weitz. Inverted and multiple nematic emulsions. *Phys. Rev. E*, 57:627–637, 1998.
- [35] J. Fukuda. Liquid crystal colloids: A novel composite material based on liquid crystals. *J. Phys. Soc. Japan*, 78:041003, 2009.
- [36] M. Yada, J. Yamamoto, and H. Yokoyama. Direct observation of anisotropic interparticle forces in nematic colloids with optical tweezers. *Phys. Rev. E*, 92:185501, 2004.
- [37] I. Muševič, M. Škarabot, U. Tkalec, M. Ravnik, and S. Žumer. Two-dimensional nematic colloidal crystal self-assembled by topological defects. *Science*, 313:954–958, 2006.
- [38] P. Poulin, H. Stark, T.C. Lubensky, and D.A. Weitz. Novel colloidal interactions in anisotropic fluids. *Science*, 275:1770, 1997.
- [39] E.B. Kim, O. Guzmán, S. Grollau, N.L. Abbott, and J.J. de Pablo. Interactions between spherical colloids mediated by a liquid crystal: A molecular simulation and mesoscale study. *J. Chem. Phys.*, 121:1949–1961, 2004.
- [40] J.K. Whitmer, A.A. Joshi, T.F. Roberts, and J.J. de Pablo. Liquid-crystal mediated nanoparticles interactions and gel formation. *J. Chem. Phys.*, 138:194903, 2013.
- [41] S. Grollau, E.B. Kim, O. Guzmán, N.L. Abbott, and J.J. de Pablo. Monte Carlo simulations and dynamic field theory for suspended particles in liquid crystalline systems. *J. Chem. Phys.*, 119:2444–2455, 2003.
- [42] R.W. Ruhwandl and E.M. Terentjev. Long-range forces and aggregation of colloid particles in a nematic liquid crystal. *Phys. Rev. E*, 55:2958, 1997.
- [43] M. Škarabot, M. Ravnik, U. Tkalec, I. Poberaj, D. Babič, and I. Muševič. Hierarchical self-assembly of nematic colloidal superstructures. *Phys. Rev. E*, 77:061706, 2008.
- [44] U. Tkalec, M. Ravnik, S. Žumer, and I. Muševič. Vortexlike topological defects in nematic colloids: Chiral colloidal dimers and 2D crystals. *Phys. Rev. Lett.*, 103:127801, 2009.

- [45] Z. Eskandari, N.M. Silvestre, M. Tesinkevych, and M.M. Telo da Gama. Interactions of distinct quadrupolar nematic colloids. *Soft Matter*, 8:10100–10106, 2012.
- [46] M. Škarabot, M. Ravnik, S. Žumer, U. Tkalec, I. Poberaj, D. Babič, N. Osterman, and I. Muševič. Interactions of quadrupolar nematic colloids. *Phys. Rev. E*, 77:031705, 2008.
- [47] I. Muševič and M. Škarabot. Self-assembly of nematic colloids. *Soft Matter*, 4:195–199, 2008.
- [48] U.M. Ognysta, A.B. Nych, V.A. Uzunova, V.M. Pergamenschik, V.G. Nazarenko, M. Škarabot, and I. Muševič. Square colloidal lattices and pair interactions in a binary system of quadrupolar nematic colloids. *Phys. Rev. E*, 83:041709, 2011.
- [49] A. Nych, U. Ognysta, M. Škarabot, M. Ravnik, S. Žumer, and I. Muševič. Assembly and control of 3D nematic dipolar colloidal crystals. *Nat. Commun.*, 4:1489, 2013.
- [50] N.M. Silvestre, Q. Liu, B. Senyuk, I.I. Smalyukh, and M. Tasinkevych. Towards template-assisted assembly of nematic colloids. *Phys. Rev. Lett.*, 112:225501, 2014.
- [51] M. Rahimi, T.F. Roberts, J.C. Armas-Pérez, X. Wang, E. Bukusoglu, N.L. Abbott, and J.J. de Pablo. Nanoparticle self-assembly at the interface of liquid crystal droplets. *Proc. Nat. Acad. Sci.*, 112:5297–5302, 2015.
- [52] D. Andrienko, M.P. Allen, G. Skačej, and S. Žumer. Defect structures and torques on an elongated colloidal particle immersed in a liquid crystal host. *Phys. Rev. E*, 65:041702, 2002.
- [53] D.L. Cheung and M.P. Allen. Forces between cylindrical nanoparticles in a liquid crystal. *Langmuir*, 24:1411–1417, 2008.
- [54] F.R. Hung. Quadrupolar particles in a nematic liquid-crystal: Effects of particle size and shape. *Phys. Rev. E*, 79:021705, 2009.
- [55] M. Tasinkevych, F. Mondiot, O. Mondain-Monval, and J.-C. Loudet. Dispersions of ellipsoidal particles in a nematic liquid crystal. *Soft Matter*, 10:2047–2058, 2014.
- [56] U. Tkalec, M. Škarabot, and I. Muševič. Interactions of micro-rods in a thin layer of a nematic liquid crystal. *Soft Matter*, 4:2402–2409, 2008.
- [57] B. Senyuk, Q. Liu, S. He, R.D. Kamien, R.B. Kusner, T.C. Lubensky, and I.I. Smalyukh. Topological colloids. *Nature*, 493:200, 2013.
- [58] C.P. Lapointe, T.G. Mason, and I.I. Smalyukh. Shape-controlled colloidal interactions in nematic liquid crystals. *Science*, 326:1083–1086, 2009.

- [59] F. Mondiot, S.P. Chandran, O. Mondain-Monval, and J.-C. Loudet. Shape-induced dispersion of colloids in anisotropic fluids. *Phys. Rev. Lett.*, 103: 238303, 2009.
- [60] A. Martinez, T. Lee, T. Asavei, H. Rubinsztein-Dunlop, and I.I. Smalyukh. Three-dimensional complex-shaped photopolymerized microparticles at liquid crystal interfaces. *Soft Matter*, 8:2432, 2012.
- [61] Q. Liu, B. Senyuk, M. Tasinkevych, and I.I. Smalyukh. Nematic liquid crystal boojums with handles on colloidal handlebodies. *Proc. Nat. Acad. Sci.*, 110: 9231–9236, 2013.
- [62] A. Martinez, L. Hermosillo, M. Tasinkevych, and I.I. Smalyukh. Linked topological colloids in a nematic host. *Proc. Nat. Acad. Sci.*, 112:4546–4551, 2015.
- [63] P.A. Lebwohl and G. Lasher. Nematic-liquid-crystal order - A Monte Carlo calculations. *Phys. Rev. A*, 6:426–429, 1972.
- [64] U. Fabbri and C. Zannoni. A Monte Carlo investigation of the Lebwohl-Lasher lattice model in the vicinity of its orientational phase transition. *Molec. Phys.*, 58:763–788, 1986.
- [65] F. Biscarini, C. Chiccoli, P. Pasini, F. Semeria, and C. Zannoni. Phase diagram and orientational order in a biaxial lattice model: A Monte Carlo study. *Phys. Rev. Lett.*, 75:1803–1806, 1995.
- [66] H. Jang and M.J. Grimson. Surface-induced ordering in thin uniaxial liquid crystal films. *Phys. Rev. E*, 61:511–518, 2000.
- [67] R. Jose, G. Skačej, V.S.S. Sastry, and S. Žumer. Colloidal nanoparticles trapped by liquid-crystal defect lines: A lattice Monte Carlo simulations. *Phys. Rev. E*, 90:032503, 2014.
- [68] L. Onsager. The effects of shape on the interaction of colloidal particles. *Ann. N. Y. Acad. Sci.*, 51:627–659, 1949.
- [69] D. Frenkel, B.M. Mulder, and J.P. McTague. Phase diagram of a system of hard ellipsoids. *Phys. Rev. Lett.*, 52:287–290, 1984.
- [70] P.J. Camp and M.P. Allen. Phase diagram of the hard biaxial ellipsoid fluid. *J. Chem. Phys.*, 106:6681, 1997.
- [71] D. Frenkel. Onsager’s spherocylinders revisited. *J. Phys. Chem.*, 91:4912–4916, 1987.
- [72] J.G. Gay and B.J. Berne. Modification of the overlap potential to mimic a linear-site potential. *J. Chem. Phys.*, 74:3316, 1981.
- [73] M.R. Wilson. Atomistic simulations of liquid crystals. In *Liquid Crystals I*. Springer Berlin Heidelberg, 1999.



- [74] Y. Olivier, L. Muccioli, and C. Zannoni. Quinquephenyl: The simplest rigid-rod-like nematic liquid crystal, or is it? An atomistic simulation. *ChemPhysChem*, 15:1345–1355, 2014.
- [75] A. Pizzirusso, M.E. di Petro, G. de Luca, G. Celebre, M. Longeri, L. Muccioli, and C. Zannoni. Order and conformation of biphenyl in cyanobiphenyl liquid crystals: A combined atomistic molecular dynamics and  $^1\text{H}$  NMR study. *ChemPhysChem*, 15:1356–1367, 2014.
- [76] A. Akinshina, M. Walker, M.R. Wilson, G.J.T. Tiddy, A.J. Masters, and P. Carbone. Thermodynamics of the self-assembly of non-ionic chromonic molecules using atomistic simulations. The case of TP6EO2M in aqueous solution. *Soft Matter*, 11:680, 2015.
- [77] J. Peláez and M.R. Wilson. Atomistic simulations of a thermotropic biaxial liquid crystal. *Phys. Rev. Lett.*, 97:267801, 2006.
- [78] N.H. Phuong, G. Germano, and F. Schmid. Elastic constants from direct correlation functions in nematic liquid crystals: A computer simulation study. *J. Chem. Phys.*, 115:7227–7234, 2001.
- [79] J. Stelzer, L. Lech, and H. Trebin. Molecular dynamics simulations of a Gay-Berne nematic liquid crystal: Elastic properties from direct correlation functions. *J. Chem. Phys.*, 103:3098, 1995.
- [80] M.P. Allen, M.A. Warren, M.R. Wilson, A. Sauron, and W. Smith. Molecular dynamics calculation of elastic constants in Gay-Berne nematic liquid crystal. *J. Chem. Phys.*, 105:2850–2858, 1996.
- [81] S. Sarman. Flow properties of liquid crystal phases of the Gay-Berne fluids. *J. Chem. Phys.*, 108:7909–7916, 1998.
- [82] C. Wu, T. Qian, and P. Zhang. Non-equilibrium molecular-dynamics measurements of the Leslie coefficients of a Gay-Berne nematic liquid crystal. *Liq. Cryst.*, 34:1175–1184, 2007.
- [83] A. Cuetos, J.M. Ilnytskyi, and M.R. Wilson. Rotational viscosities of Gay-Berne mesogens. *Molec. Phys.*, 100:3845, 2002.
- [84] M.P. Allen, J.T. Brown, and M.A. Warren. Computer simulation of liquid crystals. *J. Phys. Cond. Mat.*, 3:335–353, 1996.
- [85] M.P. Allen and M.A. Warren. Simulation of structure and dynamics near the isotropic-nematic transition. *Phys. Rev. Lett.*, 78:1291, 1997.
- [86] D. Andrienko, G. Germano, and M.P. Allen. Liquid crystal director fluctuations and surface anchoring by molecular simulation. *Phys. Rev. E*, 62: 6688–6693, 2000.

- [87] M.P. Allen. Molecular simulation and theory of liquid crystal surface anchoring. *Molec. Phys.*, 96:1391–1397, 1999.
- [88] D. Andrienko and M.P. Allen. Theory and simulation of the nematic zenithal anchoring coefficient. *Phys. Rev. E*, 65:021704, 2002.
- [89] D.L. Cheung and F. Schmid. Monte Carlo simulations of liquid crystals near rough walls. *J. Chem. Phys.*, 122:074902, 2005.
- [90] M. Greschek and M. Schoen. Orientational prewetting of planar solid substrates by a model liquid crystal. *J. Chem. Phys.*, 135:204702, 2011.
- [91] W.M. Brown, M.K. Petersen, S.J. Plimpton, and G.S. Grest. Liquid crystal nanodroplets in solution. *J. Chem. Phys.*, 130:044901, 2009.
- [92] S. I. Hernández, J. A. Moreno-Razo, A. Ramírez-Hernandez, E. Díaz-Herrera, J. P. Hernández-Ortiz, and J. J. de Pablo. Liquid crystal nanodroplets, and the balance between bulk and interfacial interactions. *Soft Matter*, 8:1443–1450, 2012.
- [93] A. Costantini R. Berardi, L. Muccioli, S. Orlandi, and C. Zannoni. A computer simulation study of the formation of liquid crystal nanodroplets from a homogeneous solution. *J. Chem. Phys.*, 126:044905, 2007.
- [94] A.P.J. Emerson and C. Zannoni. Monte Carlo study of Gay-Berne. *J. Chem. Soc. Faraday Trans.*, 91:3441–3447, 1995.
- [95] C. Chiccoli, P. Pasini, G. Skačej, C. Zannoni, and S. Žumer. Chirality transfer from helical nanostructures to nematics: A Monte Carlo study. *Mol. Cryst. Liq. Cryst.*, 576:151–156, 2013.
- [96] M. Ricci, M. Mazzeo, R. Berardi, P. Pasini, and C. Zannoni. A molecular level simulation of a twisted nematic cell. *Faraday Disc. Chem. Soc.*, 144:171–185, 2009.
- [97] S.D. Hudson and R.G. Larson. Monte Carlo simulation of a disclination core in nematic solutions of rodlike molecules. *Phys. Rev. Lett.*, 70:19, 1993.
- [98] J.L. Billeter and R.A. Pelcovits. Defect configurations and dynamical behavior in a Gay-Berne nematic emulsion. *Phys. Rev. E*, 62:711, 2000.
- [99] M. Melle, S. Schlotthauer, M.G. Mazza, H.L. Klapp, and M. Schoen. Defect topologies in a nematic liquid crystal near a patchy colloid. *J. Chem. Phys.*, 136:194703, 2012.
- [100] D. Antypov and D.J. Cleaver. The effect of spherical additives on a liquid crystal colloid. *J. Phys. Cond. Mat.*, 16:S1887–S1900, 2004.
- [101] M. Melle, S. Schlotthauer, C.K. Hall, E. Diaz-Herrera, and M. Schoen. Disclination lines at homogeneous and heterogeneous colloids immersed in a chiral liquid crystal. *Soft Matter*, 10:5489, 2014.

- [102] B.T. Gettelfinger, J.A. Moreno-Razo, G.M. Koenig Jr, J.P. Hernández-Ortiz, N.L. Abbott, and J.J. de Pablo. Flow induced deformation of defects around nanoparticles and nanodroplets suspended in liquid crystals. *Soft Matter*, 6: 896–901, 2010.
- [103] T. Stieger, M. Schoen, and M.G. Mazza. Effects of flow on topological defects in a nematic liquid crystal near a colloid. *J. Chem. Phys.*, 140:054905, 2014.
- [104] S. Grollau, N.L. Abbott, and J.J. de Pablo. Dynamic interaction between suspended particles and defects in a nematic liquid crystal. *Phys. Rev. E*, 67: 051703, 2003.
- [105] O. Guzmán, E. B. Kim, S. Grollau, N. L. Abbott, and J. J. de Pablo. Defect structure around two colloids in a liquid crystal. *Phys. Rev. Lett.*, 91:235507, 2003.
- [106] V. Tomar, T.F. Roberts, N.L. Abbott, J.P. Hernández-Ortiz, and J.J. de Pablo. Liquid crystal mediated interactions between nanoparticles in a nematic phase. *Langmuir*, 28:6124–6131, 2012.
- [107] J.M. Ilnytskyi, A. Trokhymchuk, and M. Schoen. Topological defects around a spherical nanoparticle in nematic liquid crystal: Coarse-grained molecular dynamics simulations. *J. Chem. Phys.*, 141:114903, 2014.
- [108] D. Frenkel and B. Smit. *Understanding molecular simulation*. Academic Press, 2002.
- [109] M.P. Allen and G. Germano. Expressions for forces and torques in molecular simulations using rigid bodies. *Molec. Phys.*, 104:3225–3235, 2006.
- [110] J.M. Ilnytskyi and M.R. Wilson. A domain decomposition molecular dynamics program for the simulation of flexible molecules of spherically-symmetrical and non-spherical sites. II. Extension to NVT and NPT ensembles. *Comput. Phys. Commun.*, 148:43–58, 2002.
- [111] A. Dullweber, B. Leimkuhler, and R. McLachlan. Symplectic splitting methods for rigid body molecular dynamics. *J. Chem. Phys.*, 107:5840, 1997.
- [112] T.F. Miller, M. Eleftheriou, P. Pattnaik, A. Ndirango, D. Newns, and G.J. Martyna. Symplectic quaternion scheme for biophysical molecular dynamics. *J. Chem. Phys.*, 116:8649, 2002.
- [113] M.P. Allen and D.J. Tildesley. *Computer simulation of liquids*. Oxford University Press, 2009.
- [114] H.C. Andersen. Molecular dynamics simulations at constant pressure and/or temperature. *J. Chem. Phys.*, 72:2384, 1980.
- [115] S. Nosé. A molecular dynamics method for simulations in the canonical ensemble. *J. Chem. Phys.*, 52:255–268, 1984.

- [116] W.G. Hoover. Canonical ensemble: Equilibrium phase-space distributions. *Phys. Rev. A*, 31:1695, 1985.
- [117] R. Berardi, A.P.J. Emerson, and C. Zannoni. Monte Carlo investigations of a Gay-Berne liquid crystal. *J. Chem. Soc. Faraday Trans.*, 89:4069–4078, 1993.
- [118] D.J. Cleaver, C.M. Care, M.P. Allen, and M.P. Neal. Extension and generalization of the Gay-Berne potential. *Phys. Rev. E*, 54:559–567, 1996.
- [119] M.A. Bates and G.R. Luckhurst. Computer simulation studies of anisotropic systems. XXX. The phase behavior and structure of a Gay-Berne mesogens. *J. Chem. Phys.*, 110:7087, 1999.
- [120] E. de Miguel, L.R. Rull, M.K. Chalam, and K.E. Gubbins. Liquid crystal phase diagram of the Gay-Berne fluid. *Molec. Phys.*, 74:405–424, 1991.
- [121] L.F. Rull. Phase diagram of a liquid crystal model: A computer simulation study. *Physica A*, 220:113–138, 1995.
- [122] A.P.J. Emerson, G.R. Luckhurst, and S.G. Whatling. Computer simulation studies of anisotropic systems. *Molec. Phys.*, 82:113–124, 1994.
- [123] S. Plimpton. Fast parallel algorithms for short-range molecular dynamics. *J. Chem. Phys.*, 117:1–19, 1995.
- [124] J. Ihnyskyi and M.R. Wilson. A domain decomposition molecular dynamics program for the simulation of flexible molecules with an arbitrary topology of Lennard-Jones and/or Gay-Berne sites. *Comput. Phys. Commun.*, 134:23–32, 2001.
- [125] R. Berardi, C. Fava, and C. Zannoni. A generalized Gay-Berne intermolecular potential for biaxial particles. *Chem. Phys. Lett.*, 236:462–468, 1995.
- [126] R. Everaers and M.R. Ejtehadi. Interaction potentials for soft and hard ellipsoids. *Phys. Rev. E*, 67:041710, 2003.
- [127] S. Kralj and E.G. Virga. Universal fine structure of nematic hedgehogs. *J. Phys. A Math. Gen.*, 34:829–838, 2001.
- [128] T. Araki and H. Tanaka. Colloidal aggregation in a nematic liquid crystal: Topological arrest of particles by a single-stroke disclination line. *Phys. Rev. Lett.*, 97:127801, 2006.
- [129] A. Sparavigna, A. Sanna, M. Montrucchio, and A. Strigazzi. Streamline image analysis: A new tool for investigating defects in nematic liquid crystals. *Liq. Cryst.*, 26:1467–1478, 1999.
- [130] B.G. Chen, P.J. Ackerman, G.P. Alexander, R.D. Kamien, and I.I. Smalyukh. Generating the Hopf fibration experimentally in nematic liquid crystals. *Phys. Rev. Lett.*, 110:237801, 2013.

- [131] S. Čopar, T. Porenta, and S. Žumer. Visualisation methods for complex nematic fields. *Liq. Cryst.*, 40:1759–1768, 2013.
- [132] A.T. Gabriel, T. Meyer, and G. Germano. Molecular graphics of convex body fluids. *J. Chem. Theor. Comput.*, 4:468–476, 2008.
- [133] M. Zapotocky, P.M. Goldbart, and N. Goldenfeld. Kinetics of phase ordering in uniaxial and biaxial nematic films. *Phys. Rev. E*, 51:1216, 1995.
- [134] J.L. Billeter, A.M. Smondyrev, G.B. Loriot, and R.A. Pelcovits. Phase-ordering of the Gay-Berne nematic liquid crystal. *Phys. Rev. E*, 60:6831, 1999.
- [135] A.C. Callan-Jones, R.A. Pelcovits, V.A. Slavin, S. Zhang, D.H. Laidlaw, and G.B. Loriot. Simulation and visualization of topological defects in nematic liquid crystals. *Phys. Rev. E*, 74:061701, 2006.
- [136] M.P. Allen. Molecular graphics and the computer simulation of liquid crystals. *Molec. Simul.*, 2:301–306, 1989.
- [137] R. H. Bartels, J.C. Beatty, and B. A. Barsky. *An introduction to splines for use in computer graphics and geometric modeling*. Morgan Kaufmann, 1987.
- [138] T.J. Jankun-Kelly, S. Zhang, A.C. Callan-Jones, R.A. Pelcovits, V.A. Slavin, and D. H. Laidlaw. *Visualization and Processing of Tensor Fields*. Springer, 2009.
- [139] U. Ayachit. *The ParaView Guide: A parallel visualization application*. Kitware, 2015.
- [140] C. Oseen. The theory of liquid crystals. *Trans. Faraday Soc.*, 29:883, 1933.
- [141] H. Zocher. The effect of a magnetic field on the nematic state. *Discuss. Faraday Soc.*, 29:945, 1933.
- [142] S. Singh. Curvature elasticity in liquid crystals. *Physics Reports*, 277:284–384, 1996.
- [143] M. Schadt and W. Helfrich. Voltage-dependent activity of a twisted nematic liquid crystal. *Appl. Phys. Lett.*, 18:127, 1971.
- [144] M. Ravnik and S. Žumer. Nematic colloids entangled by topological defects. *Soft Matter*, 5:269–274, 2009.
- [145] A.A. Verhoeff, R.H.J Otten, P. van der Schoot, and H.N.W. Lekkerkerker. Shape and director field deformation of tactoids of plate-like colloids in a magnetic field. *J. Phys. Chem. B*, 113:3704–3708, 2009.
- [146] P.C. Martin, O. Parodi, and P.S. Pershan. Unified hydrodynamic theory for crystals, liquid crystals, and normal fluids. *Phys. Rev. A*, 6:2401, 1972.

- [147] M.P. Allen and D. Frenkel. Calculation of liquid-crystal Frank constants by computer simulation. *Phys. Rev. A*, 37:1813, 1988.
- [148] M.P. Allen and D. Frenkel. Calculation of liquid-crystal Frank constants by computer simulation. *Phys. Rev. A*, 42:3641, 1990. Erratum.
- [149] E. Fischermeier, D. Bartuschat, T. Preclik, and M. Marechal. Simulation of a hard-spherocylinder liquid crystal with the *pe*. *Comput. Phys. Commun.*, 185:3156–3161, 2014.
- [150] D.J. Cleaver and M.P. Allen. Computer simulations of the elastic properties of liquid crystals. *Phys. Rev. A*, 43:1918–1931, 1991.
- [151] T. Gruhn and S. Hess. Monte Carlo simulation of the director field of a nematic liquid crystal with three elastic coefficients. *Z. Naturf. A*, 51a:1–9, 1996.
- [152] A.A. Joshi, J.K. Whitmer, O. Guzmán, N.L. Abbott, and J.J. de Pablo. Measuring liquid crystal elastic constants with free energy perturbations. *Soft Matter*, 10:882–893, 2014.
- [153] A. Poniewierski and J. Stecki. Statistical theory of the elastic constants of nematic liquid crystals. *Molec. Phys.*, 38:1931–1940, 1979.
- [154] M.D. Lipkin, S.A. Rice, and U. Mohanty. The elastic constants of condensed matter: A direct-correlation function approach. *J. Chem. Phys.*, 82:472, 1985.
- [155] H. Yokoyama. Density-functional theory of surfacelike elasticity of nematic liquid crystals. *Phys. Rev. E*, 55:2938, 1997.
- [156] J. Stelzer, L. Longa, and H. Trebin. Elastic constants of nematic liquid crystals from molecular dynamics simulations. *Mol. Cryst. Liq. Cryst.*, 262:455–461, 1995.
- [157] M.R. Wilson, M.P. Allen, A. Sauron, and W. Smith. Replicated data and domain decomposition molecular dynamics techniques for simulation of anisotropic potentials. *J. Comput. Chem.*, 18:478, 1997.
- [158] E. de Miguel, E.M. del Rio, J.T. Brown, and M.P. Allen. Effect of the attractive interactions on the phase behavior of the Gay-Berne liquid crystal model. *J. Chem. Phys.*, 105:4234, 1996.
- [159] J.T. Brown, M.P. Allen, E. Martín del Río, and E. de Miguel. Effects of elongation on the phase behavior of the Gay-Berne fluid. *Phys. Rev. E*, 57: 6685, 1998.
- [160] Groupe d’Etude des Cristaux Liquides (Orsay). Dynamics of fluctuations in nematic liquid crystals. *J. Chem. Phys.*, 51:816, 1969.
- [161] M.J. Stephen and J.P. Straley. Physics of liquid crystals. *Rev. Mod. Phys.*, 46: 617–704, 1974.

- [162] G. Durand, L. Leger, F. Rondelez, and M. Veyssie (Orsay Liquid Crystal Group). Quasielastic rayleigh scattering in nematic liquid crystals. *Phys. Rev. Lett.*, 22:1361, 1969.
- [163] D.C. Van Eck and M. Perdeck. Experimental data on the elasticities and viscosities of some nematics. *Mol. Cryst. Liq. Cryst.*, 49:39–45, 1978.
- [164] R. Borsali, D.Y. Yoon, and R. Pecora. Determination of splay and twist relaxation modes in nematic liquid crystals from dynamic light scattering experiments. *J. Phys. Chem. B*, 102:6337–6341, 1998.
- [165] F. Giavazzi, S. Crotti, A. Speciale, F. Serra, G. Zanchetta, V. Trappe, M. Buscaglia, T. Bellini, and R. Cerbino. Viscoelasticity of nematic liquid crystals at a glance. *Soft Matter*, 10:3938, 2014.
- [166] D. Forster. Hydrodynamics and correlation functions in ordered systems: Nematic liquid crystals. *Ann. Phys.*, 85:505–534, 1974.
- [167] D. Forster. *Hydrodynamic fluctuations, broken symmetry and correlation functions*, volume 47 of *Frontiers in Physics*. W. A. Benjamin, Advanced Book Program, Reading, 1975.
- [168] J.L. Barrat and J.P. Hansen. *Basic concepts for simple and complex liquids*. Cambridge University Press, 2003.
- [169] J.P. Hansen and I.R. McDonald. *Theory of simple liquids with applications to soft matter*. Academic Press, 2013.
- [170] H. Wang, T.X. Wu, S. Gauza, J.R. Wu, and S.-T. Wu. A method to estimate the Leslie coefficients of liquid crystal based on MBBA data. *Liq. Cryst.*, 33: 91–98, 2006.
- [171] A.M. Smondyrev, G.B. Loriot, and R.A. Pelcovits. Viscosities of the Gay-Berne nematic liquid crystal. *Phys. Rev. Lett.*, 75:2340, 1995.
- [172] S. Cozzini, L.F. Rull, G. Ciocotti, and G.V. Paolini. Intrinsic frame transport for a model of nematic liquid crystal. *Physica A*, 240:173–187, 1997.
- [173] L. Bennett and S. Hess. Nonequilibrium-molecular-dynamics investigation of the presmectic behavior of the viscosities of a Gay-Berne nematic liquid crystal. *Phys. Rev. E*, 60:5561, 1999.
- [174] S. Sarman and A. Laaksonen. Evaluation of the viscosities of a liquid crystal model system by shear flow simulation. *ChemPhysChem*, 479:47–51, 2009.
- [175] G.R. Luckhurst and R.A. Stephens and R.W. Phippen. Computer simulation studies of anisotropic systems. XIX. Mesophases formed by the Gay-Berne model mesogen. *Liq. Cryst.*, 8:451, 1990.

- [176] N. Kuzuu and M. Doi. Constitutive equation for nematic liquid crystals under weak velocity gradient derived from a molecular kinetic equation. II. Leslie coefficients for rodlike polymers. *J. Phys. Soc. Japan*, 53:1031–1040, 1984.
- [177] H. Ehrentraut and S. Hess. Viscosity coefficients of partially aligned nematic and nematic discotic liquid crystals. *Phys. Rev. E*, 51:2203, 1995.
- [178] M. Kröger and S. Sellers. Viscosities of nematic and discotic nematic liquid crystals according to the affine transformation model. *Mol. Cryst. Liq. Cryst.*, 300:245–262, 1997.
- [179] N. Schopohl and T.J. Sluckin. Defect core in nematic liquid crystals. *Phys. Rev. Lett.*, 59:2582, 1987.
- [180] Y. Gu and N.L. Abbott. Observation of Saturn-ring defects around solid microspheres in nematic liquid crystals. *Phys. Rev. Lett.*, 85:4719, 2000.
- [181] O. Mondain-Monval, J.C. Dedieu, T. Gulik-Krzywicki, and P. Poulin. Weak surface energy in nematic dispersions: Saturn ring defects and quadrupolar interactions. *Euro. Phys. J. B*, 12:167–170, 1999.
- [182] J.-C. Loudet, P. Barois, and P. Poulin. Colloidal ordering from phase separation to continuous phase. *Nature*, 407:611, 2000.
- [183] I. Muševič, M. Škarabot, D. Babič, N. Osterman, I. Poberaj, V. Nazarenko, and A. Nych. Laser trapping of small colloidal particles in a nematic liquid crystal: Clouds and ghosts. *Phys. Rev. Lett.*, 93:187801, 2004.
- [184] P. Poulin, V. Raghunathan, P. Richetti, and D. Roux. On the dispersion of latex particles in a nematic solution. *J. de Physique II*, 4:1557–1569, 1994.
- [185] V.A. Raghunathan, P. Richetti, and D. Roux. Dispersion of latex particles in a nematic solution. Phase diagram and elastic properties. *Langmuir*, 12: 3789–3792, 1996.
- [186] G.M. Koenig, J.J. de Pablo, and N.L. Abbott. Characterization of the reversible interaction of pairs of nanoparticles dispersed in nematic liquid crystals. *Langmuir*, 25:13318–13321, 2009.
- [187] H. Stark. Saturn-ring defects around microspheres suspended in nematic liquid crystals: An analogy between confined geometries and magnetic fields. *Nature*, 493:200–205, 2002.
- [188] M. Ravnik, M. Škarabot, S. Zumer, U. Tkalec, I. Poberaj, D. Babic, N. Osterman, and I. Musevic. Entangled nematic colloidal dimers and wires. *Phys. Rev. Lett.*, 99:247801, 2007.
- [189] S. Čopar and S. Žumer. Nematic braids: Topological invariants and rewiring of disclinations. *Phys. Rev. Lett.*, 106:177801, 2011.



- [190] M. Ravnik and S. Žumer. Nematic braids: 2D entangled nematic liquid crystal colloids. *Soft Matter*, 5:4520–4525, 2009.
- [191] T. Araki, F. Serra, and H. Tanaka. Defect science and engineering of liquid crystals under geometrical frustration. *Soft Matter*, 9:8107, 2013.
- [192] U. Tkalec, M. Ravnik, S. Čopar, S. Žumer, and I. Mušević. Reconfigurable knots and links in chiral nematic colloids. *Science*, 333:62, 2011.
- [193] M. Nikkhou, M. Škarabot, and I. Mušević. Topological binding and elastic interactions of microspheres and fibres in a nematic liquid crystal. *Euro. Phys. J. E*, 38:115, 2015.
- [194] M. Nikkhou, M. Škarabot, S. Čopar, M. Ravnik, S. Žumer, and I. Mušević. Light-controlled topological charge in a nematic liquid crystal. *Nature*, 11: 183–187, 2015.
- [195] V.S.R. Jampani, M. Škarabot, M. Ravnik, S. Čopar, S. Žumer, and I. Mušević. Colloidal entanglement in highly twisted chiral nematic colloids: Twisted loops, Hopf links and trefoil knots. *Phys. Rev. E*, 84:031703, 2011.
- [196] S. Čopar, U. Tkalec, I. Mušević, and S. Žumer. Knot theory realizations in nematic colloids. *Proc. Nat. Acad. Sci.*, 112:1675–1680, 2015.
- [197] T.A. Wood, J.S. Lintuvuori, A.B. Schofield, D. Marenduzzo, and W.C.K. Poon. A self-quenched defect glass in a colloid-nematic liquid crystal composite. *Science*, 334:79–83, 2011.
- [198] A. Agarwal, E. Huang, S. Palecek, and N.L. Abbott. Optically responsive and mechanically tunable colloid-in-liquid crystal gels that support growth of fibroblasts. *Adv. Mater.*, 20:4804–4809, 2008.
- [199] M. Ravnik, B. Črnko, and S. Žumer. Nematic braids: Modeling of colloidal structures. *Mol. Cryst. Liq. Cryst.*, 508:150–162, 2009.
- [200] A. Bogi, P. Martinot-Lagarde, I. Dozov, and M. Nobili. Anchoring screening of defects interaction in a nematic liquid crystal. *Phys. Rev. Lett.*, 89:225501, 2002.
- [201] D. Svenšek and S. Žumer. Fluctuations of topological disclination lines in nematic liquid crystals: Renormalization of the string model. *Phys. Rev. E*, 70:040701, 2004.
- [202] G. Tóth, C. Denniston, and J.M. Yeomans. Hydrodynamics of topological defects in nematic liquid crystals. *Phys. Rev. Lett.*, 88:105504, 2002.
- [203] I. Chuang, N. Turok, and B. Yurke. Late-time coarsening dynamics in a nematic liquid crystal. *Phys. Rev. Lett.*, 66:2472, 1991.
- [204] S. Thiberge, C. Chevillard, J.M. Gilli, and A. Buka. Critical radius of loop defects in homeotropic liquid crystal. *Liq. Cryst.*, 26:1225–1234, 1999.

- [205] H. Imura and K. Okano. Friction coefficient for a moving disclination in a nematic liquid crystal. *Phys. Lett. A*, 42A:403–404, 1973.
- [206] P.E. Cladis, W. van Saarloos, P.L. Finn, and A.R. Kortan. Dynamics of line defects in nematic liquid crystals. *Phys. Rev. Lett.*, 58:222–225, 1987.
- [207] A. Mertelj and M. Čopič. Observation of thermal fluctuations of disclination lines in a nematic liquid crystal. *Phys. Rev. E*, 69:021711, 2004.
- [208] N. Osterman, J. Kotar, E.M. Terentjev, and P. Cicuta. Relaxation kinetics of stretched disclination lines in a nematic liquid crystal. *Phys. Rev. E*, 81:061701, 2010.
- [209] I.I. Smalyukh, A.N. Kuzmin, A.V. Kachynski, P.N. Prasad, and O. Lavrentovich. Optical trapping of colloidal particles and measurement of the defect line tension and colloidal forces in a thermotropic nematic liquid crystal. *Appl. Phys. Lett.*, 86:021913, 2005.
- [210] P. Chaikin and T.C. Lubensky. *Principles of condensed matter physics*. Cambridge University Press, 1995.
- [211] D. Pires, J.-B. Fleury, and Y. Galerne. Colloid particles in the interaction field of a disclination line in a nematic phase. *Phys. Rev. Lett.*, 98:247801, 2007.
- [212] J.-B. Fleury, D. Pires, and Y. Galerne. Self-connected 3D architecture of microwires. *Phys. Rev. Lett.*, 103:267801, 2009.
- [213] P. Kosyrev, M. Ravnik, and S. Žumer. Branching of colloidal chains in capillary-confined nematics. *Phys. Rev. Lett.*, 96:048301, 2006.
- [214] S. Žumer, J. Fukuda, and M. Ravnik. Confined colloidal blue phases with potential for photonics. *Mol. Cryst. Liq. Cryst.*, 561:107–114, 2012.
- [215] M.A. Gharbi, M. Nobili, and C. Blanc. Use of topological defects as templates to direct assembly of colloidal particles at nematic interfaces. *J. Coll. Int. Sci.*, 417:250–255, 2014.
- [216] D. Coursault, J. Grand, B. Zappone, H. Ayeb, G. Lévi, N. Féridj, and E. Lacaze. Linear self-assembly of nanoparticles within liquid crystal defect arrays. *Adv. Mater.*, 24:1461–1465, 2012.
- [217] I. Mušević. Optical manipulation and self-assembly of nematic colloids: colloidal crystals and superstructures. *Liq. Cryst. Today*, 19:2–12, 2010.
- [218] D. Engström, R.P. Trivedi, M. Persson, M. Goksör, K.A. Bartness, and I.I. Smalyukh. Three-dimensional imaging of liquid crystal structures and defects by means of holographic manipulation of colloidal nanowires with faceted side-walls. *Soft Matter*, 7:6304, 2011.
- [219] A. Sengupta, C. Bahr, and S. Herminghaus. Topological microfluidics for flexible micro-cargo concepts. *Soft Matter*, 9:7251, 2013.

- [220] M. Ravnik, G.P. Alexander, J.M. Yeomans, and S. Zumer. Mesoscopic modelling of colloids in chiral nematics. *Faraday Disc. Chem. Soc.*, 144:159–169, 2009.
- [221] C. Blanc. Ordering nano- and microparticles assemblies with liquid crystals. *Liq. Cryst. Rev.*, 1:83–109, 2013.
- [222] J. Milette, V. Toader, E.R. Soulé, R.B. Lennox, A.D. Rey, and L. Reven. A molecular and thermodynamic view of the assembly of gold nanoparticles in nematic liquid crystal. *Langmuir*, 29:1258–1263, 2013.